

5-1-2014

The effect of single crystal elastic and plastic anisotropy on stress and strain heterogeneity: comparison of olivine to other common minerals

Christopher Joseph Cline li
University of Nevada, Las Vegas, clinec4@unlv.nevada.edu

Follow this and additional works at: <https://digitalscholarship.unlv.edu/thesesdissertations>



Part of the [Geochemistry Commons](#), [Geology Commons](#), and the [Mineral Physics Commons](#)

Repository Citation

Cline li, Christopher Joseph, "The effect of single crystal elastic and plastic anisotropy on stress and strain heterogeneity: comparison of olivine to other common minerals" (2014). *UNLV Theses, Dissertations, Professional Papers, and Capstones*. 2065.
<https://digitalscholarship.unlv.edu/thesesdissertations/2065>

This Thesis is protected by copyright and/or related rights. It has been brought to you by Digital Scholarship@UNLV with permission from the rights-holder(s). You are free to use this Thesis in any way that is permitted by the copyright and related rights legislation that applies to your use. For other uses you need to obtain permission from the rights-holder(s) directly, unless additional rights are indicated by a Creative Commons license in the record and/or on the work itself.

This Thesis has been accepted for inclusion in UNLV Theses, Dissertations, Professional Papers, and Capstones by an authorized administrator of Digital Scholarship@UNLV. For more information, please contact digitalscholarship@unlv.edu.

THE EFFECT OF SINGLE CRYSTAL ELASTIC AND PLASTIC ANISOTROPY
ON STRESS AND STRAIN HETEROGENEITY: COMPARISON OF OLIVINE TO
OTHER COMMON MINERALS

By

Christopher Joseph Cline II

Bachelor of Science in Geology
University of Nevada Las Vegas
2012

A thesis submitted in partial fulfillment
of the requirements for the

Master of Science - Geoscience

Department of Geoscience
College of Sciences
The Graduate College

University of Nevada, Las Vegas
May 2014

Copyright by Christopher J. Cline II, 2014
All Rights Reserved



THE GRADUATE COLLEGE

We recommend the thesis prepared under our supervision by

Christopher Joseph Cline II

entitled

The Effect of Single Crystal Elastic and Plastic Anisotropy on Stress and Strain Heterogeneity: Comparison of Olivine to Other Common Minerals

is approved in partial fulfillment of the requirements for the degree of

Master of Science - Geoscience

Department of Geoscience

Pamela Burnley, Ph.D., Committee Chair

Rodney Metcalf, Ph.D., Committee Member

Michael Wells, Ph.D., Committee Member

Andrew Cornelius, Ph.D., Graduate College Representative

Kathryn Hausbeck Korgan, Ph.D., Interim Dean of the Graduate College

May 2014

ABSTRACT

The effect of single crystal elastic and plastic anisotropy on stress and strain heterogeneity: comparison of olivine to other common minerals

By

Christopher J. Cline II

Dr. Pamela C. Burnley Examination committee chair
Associate Research Professor
University of Nevada Las Vegas

In order to investigate the influence of single crystal elastic anisotropy on the heterogeneity of stress distributions during polycrystalline deformation multiple deformed crystalline materials were analyzed using electron backscatter diffraction (EBSD). Deformation experiments were conducted on samples of Solnhofen limestone using a modified Griggs piston cylinder apparatus at UNLV, and also on San Carlos olivine using the D-DIA multi-anvil press at the National Synchrotron Light Source beamline X17B2. Analysis of the mechanical twins in deformed calcite and kink bands in olivine help elucidate deviations in local stress directions away from that of the applied macroscopic stress. Combined calculated compression directions in each microstructured grain shows that in both olivine and calcite the mean deviation of local stresses is approximately 25° , with maximum being 35° and 40° respectively. Experimental observations were compared with finite element models (FEMs) of olivine, quartz and calcite. The models were constructed using the full elastic tensor of each material, as well as an estimated single crystal yield stress. The FEMs show that with increasing single crystal elastic anisotropy there is an increase in deviation of the local

compression direction away from the macroscopic compression direction, up to 12, 13 and 19° respectively, but lack the magnitude that is observed in the experimental deformation. I hypothesize that this discrepancy originates from the lack of a grain boundary structural component in the FEMs, thus providing evidence of the importance of grain boundary sliding during polycrystalline deformation. In addition, the experimental deformation results do not show a strong correlation between the elastic anisotropy of the single crystal and the spread in local compression directions. This behavior is attributed to the differing plastic anisotropy of both materials, indicating the importance of plastic anisotropy in the prediction of stress and strain heterogeneity in polycrystalline deformation based off of single crystal properties.

ACKNOWLEDGMENTS

I would like to thank the UNLV Geoscience department for all of the support you afforded me during the duration of undergraduate and graduate degrees. To my advisor Dr. Burnley, you have shared your knowledge and opened many doors for me in the research field during our three years working together; I am truly grateful to have had you as a mentor. Also, I would like to thank my advisory committee, Dr. Rodney Metcalf, Dr. Michael Wells and Dr. Andrew Cornlelius for their time and guidance through this process.

This project would have not been completed without the logistical assistance of: Dr. Eric Ryabcki of Deutsches GeoForschungsZentrum Postdam for providing me with a block of Solnhofen limestone starting material. Dr. Gareth Seward from the University of California Santa Barbara for running EBSD maps on olivine samples when our detector was down. Jacob Tielke from University of Minnesota for providing his excel program used to calculate compression and tension directions from twinned calcite grains and Dr. Minghua Ren for allowing me to completely takeover the EBSD when I needed to acquire data. In addition, the contribution of computer programming and sample preparation made by undergraduate research assistants Rick Rowland and Evan Mohr is greatly appreciated.

In conclusion, enough cannot be said about how supportive my friends and family have been; thank you so much Amanda, Mom, Dad, Eric and Chase for understanding the long hours and time away from home. You all have kept me going with your words of encouragement.

DEDICATION

To Ralph Cline and George Pard,
thank you for imparting curiosity in me.

TABLE OF CONTENTS

ABSTRACT	iii
ACKNOWLEDGMENTS	v
DEDICATION	vi
LIST OF TABLES	ix
LIST OF FIGURES	x
CHAPTER 1 INTRODUCTION	1
High pressure and temperature experiments	1
Temporal and volumetric extrapolations	3
Modeling polycrystalline plasticity	5
Sachs model – constant stress	6
Taylor model – constant strain	8
Self-consistent models - mean field	9
Full field models	11
Objectives	12
CHAPTER 2 BACKGROUND	15
Crystallography of materials selected for deformation	17
Olivine	17
Calcite	22
CHAPTER 3 Methodology	28
Griggs apparatus	28
Calcite deformation (Griggs)	30
Starting material and sample assembly	30
Experimental procedure	31
D-DIA experiments	32
Pressure and differential stress	34
Strain and strain rate	35
Olivine deformation	36
Starting material and sample assembly	36
Experimental procedure	37
Electron backscatter diffraction	38
Finite element models	43
Construction and physical properties	43
CHAPTER 4 RESULTS	46
Olivine EBSD analysis	46
Olivine Schmid factor and misorientation analysis	48
Olivine local stress direction deviations	55

Calcite EBSD analysis	59
Calcite local stress direction deviations.....	61
Finite element model local stress deviations.....	66
CHAPTER 5 DISCUSSION	70
Misorientation distribution	70
Experimental local stress modulations.....	71
Constraints on calculated compression directions	71
Calculated local stress variations	73
Comparison to previous studies	75
Modeled results compared to experimental	77
CHAPTER 6 CONCLUSIONS	81
APPENDIX A Calcite host/twin c-axis analysis.....	83
APPENDIX B Calcite twin numerical data	103
APPENDIX C Olivine kink analysis from EBSD orientation maps	105
APPENDIX D Olivine kink numerical data	109
APPENDIX E Rotation of elastic tensors for finite element models	110
REFERENCES.....	119
VITA	127

LIST OF TABLES

Table 1	List of selected materials and their respective elastic anisotropies....	16
Table 2	Summary of conditions for calcite deformation experiments.....	32
Table 3	Summary of conditions for olivine deformation experiments	38
Table 4	Summary of EBSD map acquisition settings	39
Table 5	Run conditions for each finite element model	67

LIST OF FIGURES

Figure 1a	Depiction of D-DIA anvil and sample	2
Figure 1b	Pressure and temperature limitations for different apparatuses	2
Figure 2a	Deformation mechanism map for olivine at grain size of 1mm	5
Figure 2b	Deformation mechanism map for olivine at 7 GPa and 1700K	5
Figure 3	Components of the Schmid factor calculation	7
Figure 4	Stress state calculation using the IHM in self-consistent models ...	10
Figure 5	Example of FEMs with varying elastic properties	12
Figure 6a	Unit cell of forsterite.....	18
Figure 6b	Schematic of all slip systems in olivine	18
Figure 7	Active slip systems as a function of strain rate and temperature....	20
Figure 8	Elements of a kink band in olivine	21
Figure 9	Kinked magnesium germanate grain imaged using EBSD	22
Figure 10	Slip systems in calcite as a function of temperature and CRSS	24
Figure 11a	Stereonet showing main components of e-twins in calcite	25
Figure 11b	Schematic cross section of a calcite twin	25
Figure 12	Calcite paleostress calculation using eigenvector analysis	27
Figure 13	Diagram of the Griggs modified piston cylinder sample assembly .	31
Figure 14a	D-DIA module	34
Figure 14b	Cross section view of the D-DIA	34
Figure 15	Radiograph taken through the anvil gap in the D-DIA	36
Figure 16	Diagram depicting the D-DIA sample assembly	37
Figure 17	Geometry of EBSD acquisition	41
Figure 18	Noise reduction process in EBSD maps.....	42
Figure 19	Finite element mesh with grain populations.....	44
Figure 20	Example of Euler rotations made to elastic tensors.....	45
Figure 21a	Photomicrograph of deformed San_197.....	46
Figure 21b	Photomicrograph of deformed Ol_412.....	46
Figure 22	Euler angle coloration on EBSD map of San_197	47
Figure 23	Euler angle EBSD map for Ol_412	48
Figure 24	Mean Misorientation EBSD map of San_197	50
Figure 25	Schmid factor EBSD map of San_197.....	51
Figure 26	Schmid factor vs. mean misorientation.....	52
Figure 27	Histogram of mean misorientation in San_197.....	54
Figure 28	Histogram of mean misorientation in Ol_412.....	54
Figure 29	EBSD map of Ol_412 showing kinked grains	55
Figure 30a	Expanded view of kinked grain.....	56
Figure 30b	Misorientation profile of kinked grain	56
Figure 30c	3-D crystallographic orientaiton of domains in kinked grain.....	56
Figure 31	Kinked grain confirmation	57
Figure 32	All kinked grains on a pole figure.....	58
Figure 33	Rotation of calculated compression directions in kinked grains.....	59
Figure 34a	Photomicrograph of sample Sfn_002	60
Figure 34b	Photomicrograph of sample Sfn_004	60
Figure 35	EBSD OIM of Sfn_002 after noise reduction	60

Figure 36	EBSD OIM of Sfn_004 after noise reduction	61
Figure 37	EBSD OIM of Sfn_002 showing twinned grains	62
Figure 38a	Expanded view of twinned grain in Sfn_002	63
Figure 38b	Pole figure showing c-axis of host and twinned grain	63
Figure 38c	Misorientation profile from twinned grain	63
Figure 39	EBSD OIM of Sfn_001 with no twins	63
Figure 40	Calculation of preferred compression direction	65
Figure 41	Compression directions from both calcite experiments	66
Figure 42	Example subsets of FEMs	68
Figure 43	Pictorial description of stress variation calculation in FEMs	68
Figure 44	Summary graph of all FEM angular variations	69
Figure 45	Resolved shear stress for calcite twins	72
Figure 46	Stereonet comparing olivine and calcite data	74
Figure 47	Pole figure of compression data from deformed limestone	76
Figure 48	Pole figure of 20 kinked Mg ₂ GeO ₄ grains	77
Figure 49	Comparison of FEMs to those of Burnley, (2013)	78
Figure 50	Comparison of all modeled and experimental results	80

CHAPTER 1

INTRODUCTION

The rheology of the upper mantle regulates multiple tectonic processes on earth, thus it becomes paramount to obtain a complete understanding of the flow laws and distribution of stress within this portion of the earth. Since olivine ($(\text{Mg,Fe})_2\text{SiO}_4$) is both the least viscous and most voluminous mineral in the upper mantle, deformation experiments using olivine have been the center of mantle studies for over four decades (e.g. Goetze, 1978; Demouchy et al., 2009; Faul et al., 2011). Studies include work on both single crystal (Durham et al., 1977; Bai and Kohlstedt, 1992; Raterron et al., 2007; Raterron et al., 2011) and polycrystalline deformation (Carter and Ave'lallemant, 1970; Stoker and Ashby, 1973; Goetze, 1978; Karato and Yu, 1993; Karato and Jung, 2003; Hansen et al., 2011) to establish flow laws, which are empirical fits to experimental data, and to also understand microstructural evolution (Green and Radcliffe, 1972). These deformation experiments are intended to elucidate mantle processes by being conducted at realistic pressure and temperature conditions found along the geotherm; but other parameters of volumetric and temporal scale require large extrapolations before data can be accurately interpreted (Bai et al., 1991; Karato et al., 1998; Karato, 2010).

High pressure and temperature experiments

Most high pressure apparatuses employ the simple relationship *pressure* = *force/area* to produce a high pressure environment (Fig. 1a). This relation provides two methods for creating a high pressure environment 1) increase the

applied force or 2) decrease the area over which the force is applied. Many types of high pressure apparatuses have been developed that utilize this relationship between achievable pressure and sample volume (Fig. 1b). Limitations on the applied stress are ultimately determined by the strength of all the materials used in the specific apparatus. Currently, for large volume deformation the strongest material available for use as force-generating anvils or pistons, such as tungsten carbide and cubic boron nitride, have compressive strengths that range from 4 to 8 GPa. Thus, to reach higher pressures the sample volume must decrease (Getting et al., 1993).

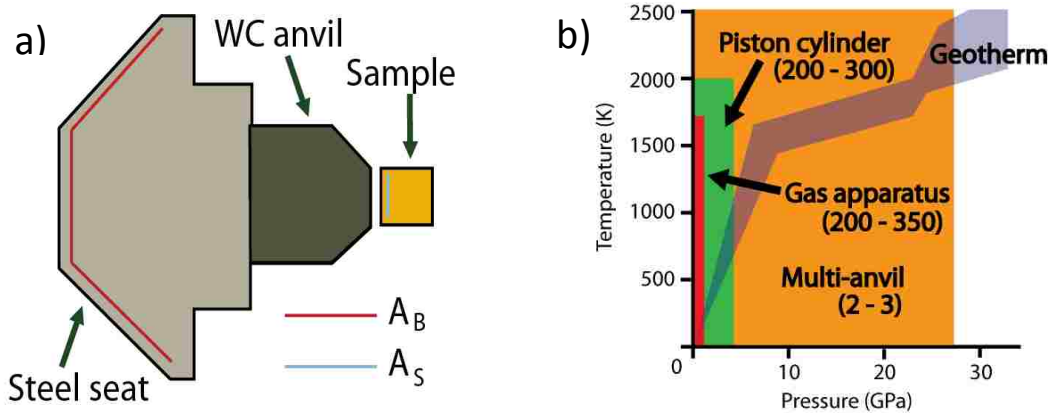


Figure 1a. Depiction of D-DIA anvil and sample. A_b represents the surface area of the back of the anvil which is in contact with the pressure source, A_s represents the surface area of the sample. Figure 1b. Pressure and temperature limitations for different apparatuses. Pressure/temperature limitations in common large volume high pressure deformation apparatuses plotted in relation to the geotherm, volumes in parentheses are listed in mm^3 . Notice that to achieve any pressure above approximately 25 GPa, large volume deformation is no longer viable and extremely small samples volumes are required, such as found in diamond anvil cell, redrawn inspired by Karato (2010).

For polycrystalline deformation studies, decreases in sample volume are usually accompanied by a decrease in the grain size in order to maintain satisfactory grain statistics. With sample volumes in the multi-anvil deformation apparatus generally constrained to 2 mm^3 (refer to Fig. 1b), experimental grain sizes are usually on the order of 10's of μm 's, differing from presumed mantle grain sizes (10's of μm 's up to 10's of mm 's) by multiple orders of magnitude (Nicolas, 1978; Ave'lallemant et al., 1980). This discrepancy in grain size adds complexity to data interpretation as many aggregate properties and deformation mechanisms in olivine have been shown to be sensitive to mean grain size, such as: seismic wave attenuation (Faul and Jackson, 2005; Jackson et al., 2002), grain boundary sliding (Lee et al., 2002; Hirth and Kohlstedt, 2003; Hansen et al., 2011) and activation of diffusional processes (Karato et al., 1986; Karato and Yu, 1993; Hirth and Kohlstedt, 2003). For a microstructural study, such as this one, this grain size sensitivity needs to be taken into account to ensure the experiment is conducted at the correct conditions to activate the desired deformation mechanisms (i.e. dislocation glide vs. diffusion creep).

Temporal and volumetric extrapolations

The issues of temporal scale in deformation experiments are far more difficult to overcome than those of a volumetric origin. Inevitably, the duration of experiments are limited by the human timescale. These time constraints mean that experimental strain rates are generally between $10^{-3} - 10^{-6} \text{ s}^{-1}$, in contrast to the estimated mantle strain rate of $10^{-12} - 10^{-16} \text{ s}^{-1}$ (Karato, 2010). Thus, large

extrapolations of flow data are needed in order to be applied to mantle processes (Karato et al., 1986; Karato, 1988).

Mainly the extrapolation is not a correction of strain rate, but the differential stress which is applied to the sample. The relationship between stress and strain rate is illustrated by a flow law which is used to empirically fit experimental mechanical data (Equation 1). Equation 1 is a flow law Where $\dot{\epsilon}$ is strain rate, A is a parameter based on the material, σ is the differential stress, n is a deformation mechanism-specific stress exponent, Q is activation energy, P is pressure, V is volume, R is the ideal gas constant and T is temperature in Kelvin. In (equation 1), the value of strain rate is a function of the differential stress, so as our experiments are forced to higher strain rates than naturally occur in the mantle, by consequence the applied stress must also increase to unrealistically large values.

$$\dot{\epsilon} = A\sigma^n \exp\left(\frac{-(Q+PV)}{RT}\right) \quad \text{eq.1}$$

As with the sensitivity that deformation mechanisms have to grain size, similar effects are observed at particular differential stresses. (Figs. 2a and 2b) are two different deformation mechanism maps for olivine which show how stress, grain size and temperature relate to different deformation mechanisms and strain rates (Kirby, 1983). It is clear from (Fig. 2b) that the extrapolations needed to justify deformation experiments are quite large, and can benefit from substantiation by additional means.

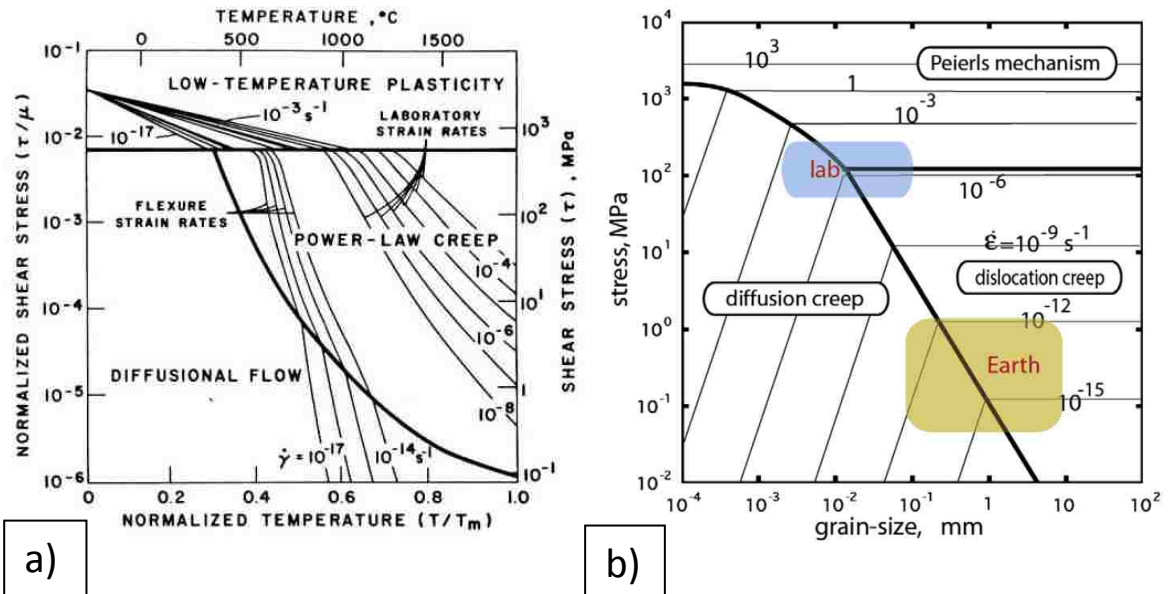


Figure 2a. Deformation mechanism map for olivine at a grain size of 1mm. Temperature has been normalized to melting temperature, From Kirby (1983). Figure 2b. Deformation mechanism map for olivine at 7 GPa and 1700 K. From Karato (2010).

Modeling polycrystalline plasticity

In order to better extrapolate the rheological behavior of polycrystalline earth materials to stress conditions and timescales that are unachievable in a laboratory setting, some sort of model is required (Karato, 2010; Karato 1998; Karato and Yu, 1993; Hirth and Kohlstaedt, 2003). Numerical models are particularly appealing for this task, but for these models to provide a sound platform for extrapolation they must be based on a sound understanding of all deformation mechanics that are operating in the real material. In a simplified description the mechanics of polycrystals can be thought of as having three components 1) the mechanical properties of the individual grains, 2) the mechanical properties of the grain boundaries and 3) the macroscopic aggregate response, which consists of the interaction of the other two components within

the polycrystal. The individual reaction of a constituent grain within a polycrystal, also known as a crystallite, to an applied stress is fairly well understood from the studies on single crystal deformation listed above and others; also, the macroscopic response of an aggregate is easily measured using laboratory techniques. The complexity arises when attempting to model how the microscopic stress and strain of the constituent grains relate to the macroscopic stress and strain of the aggregate (Castenlau et al., 2008). The early models of polycrystalline plasticity that were developed to describe the relationship between aggregate response and crystallite behaviors are end member descriptions, either focusing on homogeneous stress or strain throughout the whole polycrystal.

Sachs model – constant stress

One of these end-member models is known as the Sachs model, which assumes that each grain within a deforming aggregate is subjected to the same stress state and that this stress is equivalent to the macroscopic stress (Sachs, 1928). This type of constant stress state in a polycrystal is also known as the Ruesch state. In addition, Sachs also proposed that each crystallite deforms utilizing only the slip systems with the highest value of resolved shear stress, thus satisfying Schmid's law, see (Fig. 3).

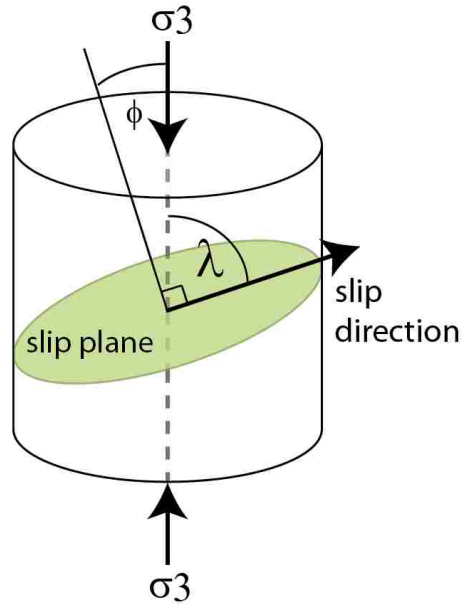


Figure 3. Components of the Schmid factor calculation. α is the angle between the applied differential stress and the normal of the slip plane, and β is the angle between the slip direction and the applied stress. Schmid factor is a value between 0 and 0.5 which is a geometric description of the amount of shear stress resolved on a specific slip plane and direction, calculated using the equation $S.F. = (\cos \alpha \cdot \cos \beta)$ (Hull and Bacon, 1984). In the case of the Sachs model, only the slip system with the highest Schmid factor will be activated (Clausen, 1997). In the situation of a crystal being orientated along a symmetry axis and two slip systems have identical Schmid factors, both systems will be activated.

When both of these aspects of the model are combined, the product is a model that considers each crystallite as an unconfined deforming single crystal, which is where the model begins to break down (Zhao et al., 2007). During deformation grains will change shape to relieve internal stresses by dislocation motion, but within a polycrystal the shape change cannot be arbitrary, since it is also controlled by the surrounding grains. If the position and shape change of the neighboring crystallites is not taken into account compatibility among grains is lost due to the creation of voids and overlap at grain boundaries, (Zhao et al., 2007; Delannay, 2001).

Taylor model – constant strain

The other end-member is the Taylor model, in which each grain in an aggregate is envisioned to accommodate the same amount of strain as the aggregate in total (Taylor, 1938). The constant strain state of each grain in a polycrystal is also known as the Voigt state. This model employs five active slip systems per grain in order to accommodate the appropriate amount of strain, in contrast to the Sachs model which only activates one slip system (Taylor, 1938; Kozaczek et al., 1992). Also, the stress state of each grain is dependent purely on its orientation, thus grain populations of different orientations will exhibit different stress states and grains cannot transfer stress to neighboring grains (Delannay, 2001). Since there is no means of maintaining stress equilibrium within the polycrystal, the model cannot be valid (Zhao et al., 2007; Delannay, 2001).

The Sachs and Taylor models both make similar assumptions which lead to the ultimate invalidity of both models; they both define deformation as being described exclusively within populations of grains defined purely by their orientation. This assumption overlooks two important phenomena which are consistently observed in experimental polycrystalline deformation: 1) Variability does exist within grain populations that share orientations during deformation and 2) stress and strain heterogeneity exist at both the inter- and intragranular scale (Clausen et al., 1998). Simplistically, these models do not account for the elastic anisotropy of the material, or the contribution of multiple grains on both the strain rate and stress state of each constituent grain within the polycrystal (Molinari et

al., 1997; Clausen, 1997). This issue was resolved with the next generation of models that began incorporating the changing stress state of constituent grains within the aggregate into the determination of each individual grains behavior. These models are described as self-consistent, since they utilize internally calculated values of stress at a given increment of deformation in the determination of the stress state for a grain at the next increment (Turner and Tome, 1994). Currently there exist two main schemes utilized to determine self-consistent values of effective stress within these models: 1) use the average stress state of all grains (mean field), or 2) use the full description of each individual stress state present in each grain (full field).

Self-consistent model – mean field

Self-consistent theory was first used in a description of polycrystalline deformation by Kroner (1961) and utilized the theory of inclusions presented by Eshelby (Eshelby, 1957; Kroner, 1961; Clausen, 1997). The theory relies on the finding that if elliptical inclusions are deformed in a homogeneous matrix, and both have linear properties, there can be uniform stress and strain rates at the intragranular scale (Eshelby, 1957; Delannay, 2001; Clausen, 1997). By providing intragranular stress and strain equilibrium throughout a deforming aggregate, there were no longer any violations of stress equilibrium or grain continuity, as in the Taylor and Sachs model respectively. This theory provided a sound basis to then build a numerical model (Delannay, 2001). The elastic-plastic self-consistent model (EPSC) of Turner and Tome (1994) is just one of these models, in which grains are represented by elliptical inclusion deforming

within an infinite homogeneous matrix (IHM), representative of an aggregate matrix (Turner and Tome, 1994). Initial input data includes orientation data through the use of Euler angles, all possible slip systems in the single crystal and their associated CRSS. As strain is imposed through the IHM each grain responds according to the single crystal rheology (Turner and Tome, 1994). The properties of the IHM are calculated by averaging the reaction of all grains to the stress field, and is recalculated after each grain in the simulated aggregate has been subjected to the previous calculated stress, thus the given name of mean-field model, see (Fig. 4) for a visual of this process (Molinaro et al., 1997; Castenlauro et al., 2008). This type of model can be used to determine macroscopic stresses on a polycrystal, but it still lacks the ability to model plastic interactions between neighboring grains, including stress and strain localization which is commonly observed in deforming aggregates (Delannay, 2001; Hansen et al., 2012).

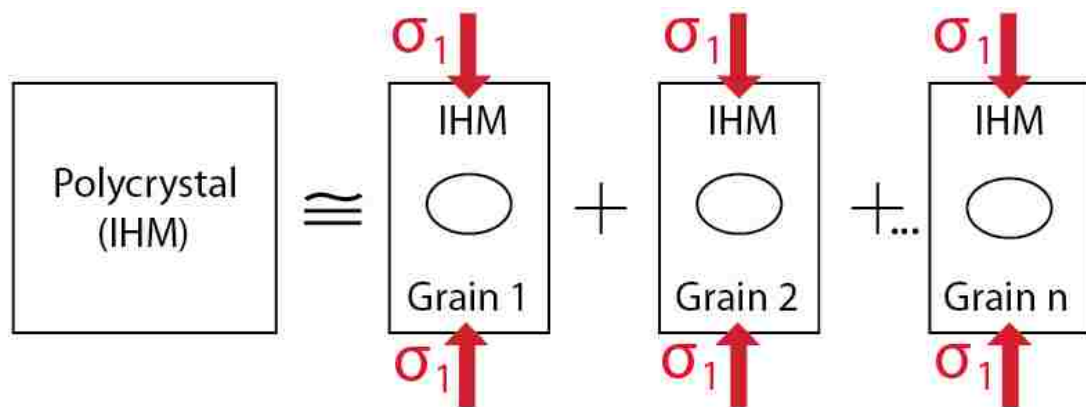


Figure 4. Stress state calculation using the IHM in self-consistent models. Modified from Molianri et al. (1997).

Full field models

In contrast to the mean field approach, there exist other models known as full field models that incorporate fluctuations in intragranular stress and strain rate as well as the plastic interaction of these grains to describe the overall aggregate behavior (Castenlau, 2008; Burnley, 2013). There exist numerous variations to the full field technique including simple 2D plane-strain finite element models (FEM) used by Burnley (2013), and the more complicated 3D Fast Fourier Transform (FFT) models used in Castenlau et al. (2008) and (2010); but due to the large computing power needed for 3D models and the small grain statistics of FFT models, we will focus on the FEM technique. Recent work within our lab using 2D plane-strain FEMs has elucidated some shortcomings of the mean field approach to modeling. In our models, the plastic interactions between grains have been observed to effect variations of the local stress tensors within the aggregate in both magnitude and direction away from the macroscopic stress tensor. These variations in the stress tensor produce patterns similar to force chains that are observed in deformation experiments on granular materials and appear to be a direct consequence of stress percolation (Fig. 5). The density of stress localization was directly affected by the anisotropy of the elastic and plastic properties of the single crystals used to construct the model, but were exaggerated from anisotropy values observed in earth materials. These results do not directly correlate to the models on geologic materials since the values of anisotropy were exaggerated, but did provide a framework to further explore the relationship between stress patterning and single crystal properties.

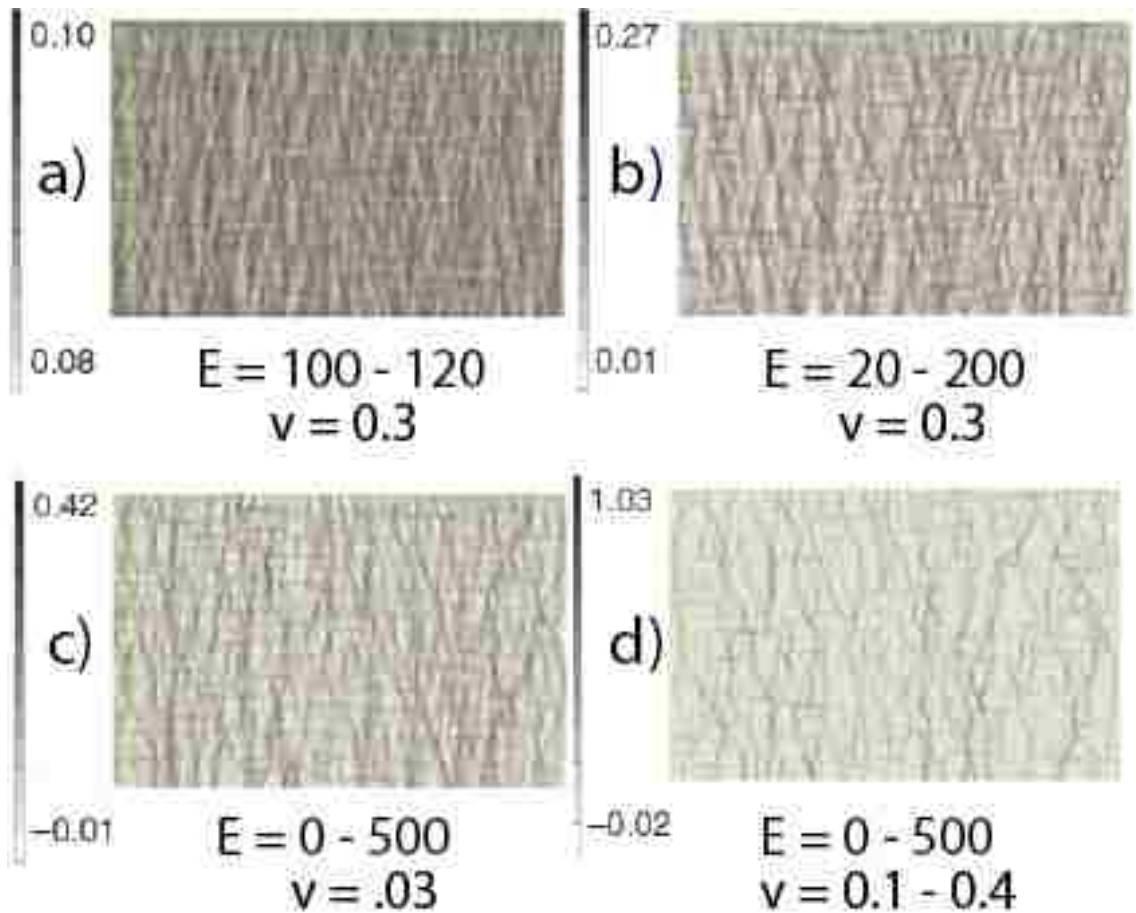


Figure 5. Example of FEMs with varying elastic properties. 4 FEMs are shown with increasing constituent grain anisotropy from a to d. E represents the range of Young's modulus and ν represents the range of Poisson ratio assigned to each grain population. The scale indicates the value of equivalent Von Mises stress (in GPa) for each model after a vertical load of 0.1 GPa is applied. Notice the difference in stress magnitudes present in the isotropic model (a) from 0.08 – 0.1 GPa compared to the anisotropic model (d) of -0.02 – 1.03 GPa, modified from Burnley (2013).

Objectives

The aim of this study is to provide new insight into single crystal controlled stress percolation in deforming polycrystals, similar to the study using finite element models. In contrast, I use an experimental technique and geologically relevant materials in order to further define the relationship between stress direction modulations in a deforming aggregate, and the anisotropy of the elastic

and plastic strengths of the single crystal. By conducting a suite of deformation experiments utilizing multiple monomineralic polycrystals that have a range of single crystal anisotropies we can infer the total stress direction modulation within each material. This was done by analyzing microstructures in each material that form with a preferred orientation to an applied stress direction, such as deformation twins and kink bands. It must be emphasized that I am not reconstructing the complete local stress tensor modulations within the aggregates; I am only determining the modulation of stress directions within each material, not the magnitudes. Studies have been conducted using deformation twins in calcite to estimate both the direction and magnitude of a stress tensor acting on an aggregate, but this type of analysis averages numerous local stress tensors calculated by twin sets and disregards the variations between individual grains and is thus not applicable to this study (Burkhard, 1993; Becker et al., 2006; Lacombe, 2007; Jang et al., 2012). Establishing the relationship between strain heterogeneity and single crystal properties will provide the ability to predict local stress direction inhomogeneities and stress patterning in a deforming polycrystal based largely on the properties of the single crystal. The ability of this relationship to be predictive has direct implications on advancing the current state of geologically relevant numerical models.

The Reuss stress state (all crystallites having equal stress) has long been shown to be a simplified interpretation of the stress field within a polycrystal, but is still commonly used in linear combination with the other isostate bound, Voigt state (all crystallites having equal strain), to determine the effective macroscopic

moduli in aggregates for studies on seismic anisotropy (Dolle, 1979; Mainprice et al., 2000; Chen, 2006; Murray, 2013). By establishing a more realistic construct of stress patterning through percolation theory into popular computer models, I can then begin to abandon the use of an assumed Reuss state of stress and start to converge on a more realistic description of stress distribution in a deforming aggregate (Burnley, 2013). To the author's knowledge there are currently no numeric models that account for modulations in the local stress direction during polycrystalline deformation, which is the main inspiration for conducting this study. In addition to contributions within the mineral physics community, the implications could be farther reaching into the geologic community providing new insight on how we interpret paleostress from deformation microstructures in the field, and could also be of interest to the material science community as a whole.

CHAPTER 2

BACKGROUND

In making the selection of materials for the deformation experiments two criteria needed to be met 1) there was a range of anisotropy values between the materials, and 2) each of the chosen materials form deformation microstructures from which local stress direction can be inferred. By meeting both of these criteria we maintain the ability to determine modulations in local stress directions as a function of constituent single crystal properties. Defining the elastic anisotropy of a single crystal is straight forward and several methods have already been devised. Plastic anisotropy is more difficult to quantify, different materials possess different symmetries, varying number and arrangement of slip systems and can have either open or closed yield surfaces. For these reasons we will be quantifiably comparing anisotropy values of the materials in this study using measures of elastic anisotropy.

There are two schemes for calculating elastic anisotropy values. The first method was developed by Ledbetter and Migliori (2006), which uses the maximum and minimum single crystal shear wave velocities to define an anisotropy value A^* . (Equation 2) shows the calculation of A^* where V_1 and V_2 are the minimum and maximum shear sound wave velocities within a single crystal (Ledbetter and Migliori, 2006).

$$A^* = v_2^2/v_1^2 \quad \text{eq.2}$$

The second method simply involves using the ratio of the maximum and minimum Young's modulus for each material, which will be referred to as Y^* . The Young's modulus is used since it is the measure of stiffness in a material and a direct result from the elastic tensor. Both of these methods allow anisotropy values to be determined in a way that is comparable between all crystal symmetries, unlike other methods such as the one developed by Zener (1948) which utilizes the elastic constants C_{11} , C_{12} and C_{14} , thus is only applicable for materials with cubic symmetry (Zener, 1948; Ledbetter and Migliori, 2006). (Table 1) shows values of A^* and Y^* for a selection of geologic materials.

Table 1
List of selected materials and their respective elastic anisotropies

Material	symmetry	A*	Y*	Reference
halite	cubic	1.42	1.34	Srivastava, 2007
MgO	cubic	1.55	1.41	Anderson, 1966
^{†‡} olivine	orthorhombic	1.55	1.75	Abramson et al., 1997
galena	cubic	1.94	1.74	Padaki et al., 1981
hornblende	monoclinic	1.91	1.90	Ahrens and Bass, 1995
[†] quartz	trigonal	2.38	1.86	Kimizuka et al., 2007
^{†‡} calcite	trigonal	2.95	2.58	Lin, 2013

[†] indicates material was used in finite element models. [‡] indicates material was used in deformation experiments. A^* refers to the method of determining anisotropy published in Ledbetter and Migliori, 2006. Y^* represents the ratio of the maximum and minimum Young's modulus. All elastic constants are from measurements made at ambient conditions.

Numerous materials accommodate strain by either deformation twinning or kinking. We chose materials within this population that have different values of A^* and Y^* which can be made into mono-phase polycrystals with a relatively small and homogeneous grain size. In addition, the synthesis of the starting aggregates cannot induce any microstructures or crystallographic preferred

orientation (CPO). Microstructures formed during the production of the aggregate will bias the determination of local stress directions; any CPO in the starting material is not ideal as it will decrease the anisotropy of the aggregate and the mechanical properties will begin to become more analogous to single crystal behavior. Olivine was the first choice of material for deformation experiments, followed by calcite because of the large difference of 1.4 in values of A^* . Quartz was used in this study, but does not form any stress dependent microstructures, therefore it was only used in finite element models and not for deformation experiments.

Crystallography of materials selected for deformation

Olivine

Olivine is a group of minerals in which a solid solution between two end-member minerals exists; one is Fe bearing, fayalite (Fe_2SiO_4 : Fa_{100}) and the other Mg bearing forsterite (Mg_2SiO_4 : Fo_{100}). Peridotite samples from the upper mantle show limited chemical variability and usually have compositions within the range of Fo_{89} to Fo_{94} . Due to this Mg rich composition the forsterite unit cell is used for descriptions of crystallography in the remainder of this study (Dehoog et al., 2010). Forsterite is a nesosilicate within the space group Pbnm, with cell parameters of $a = 4.752$ $b = 10.193$ $c = 5.977$ (Fig. 6a; Hazen 1976). The unit cell contains two octahedral sites across which Mg^{+2} and Fe^{+2} are randomly scattered, M_1 and M_2 . M_1 shares two edges with a silica tetrahedron and four edges with neighboring M_1 octahedrons, and M_2 shares only two edges with neighboring octahedral and one edge with a silica tetrahedron (Smyth and

Hazen, 1973). The bonds in the silicon tetrahedron mostly have covalent character in comparison to the Mg-O bonds which are mostly ionic. Since ionic bonds are weaker than covalent, the slip systems within the single crystal operate so glide occurs along planes which break Mg-O bonds (Poirier, 1975). Through single crystal deformation experiments and electron microscopy, eight slip systems have been found to operate within the single crystal, (Fig. 6b; Carter and Ave'Lallemant, 1970; Durham et al., 1977; Raterron et al., 2008; Raterron et al., 2012).

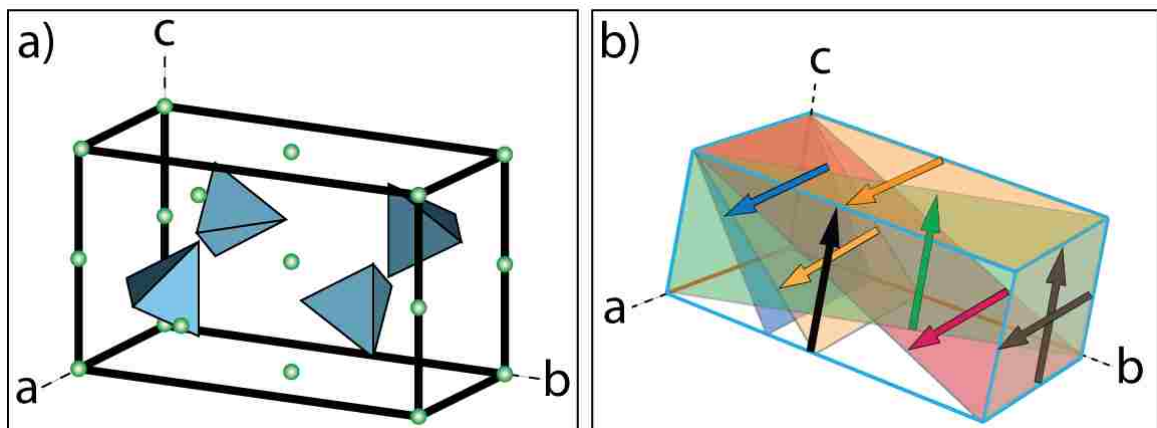


Figure 6. (a) Unit cell of forsterite. Blue represents silicon tetrahedrons and green spheres representing Mg atoms, redrawn from Couvy (2005). (b) Schematic of all slip systems in olivine. Colored planes represent slip planes while similar colored arrows indicate the burgers vector on that specific crystallographic plane, modified from Castnelau et al. (2008).

As is depicted in (Fig. 6b) $[100]$ slip occurs on multiple planes: (010) and (001) , then three planes $\{011\}$, $\{021\}$ and $\{031\}$ which are referred to as pencil glide slip systems; $[001]$ slip only occurs on the (100) , (010) and $\{110\}$ planes. Multiple slip systems (Fig. 6b) are active during polycrystalline deformation, but the last 40 years of experimentation has shown that the $[100]$ burgers vector

dominates at high temperature and low strain rate conditions, and the [001] burgers vector dominates slip during low temperature and high strain rates (Fig. 7; Carter and Ave'lallemant, 1970; Durham and Goetze, 1977; Karato et al., 1986; Raterron et al., 2007; Raterron et al., 2012). Because there are only two permissible burgers vectors, olivine only possesses three linearly independent slip systems. Thus, olivine fails to meet the Von Mises criterion for arbitrary plastic strain, which requires five independent slip systems to ensure strain compatibility during deformation (Von Mises, 1928; Castenlau, 2008). In addition to this deficiency, the geometry of the eight slip systems do not allow for dislocation creep to accommodate strain when stress is applied in the axial directions. These properties of the single crystal necessitate additional deformation mechanisms to allow polycrystalline deformation, which is partially achieved through the formation of kink bands (Burnley et al., 2013). Kink bands have been observed in both natural Iherzolites and experimentally deformed polycrystalline samples of olivine since the work of Raleigh (1968) (Nicolas et al., 1971; Green and Radcliffe, 1972; Durham and Goetz, 1977; Ave' Lallemand, 1985). As explained by Christie et al. (1964) and Raleigh (1968), the morphology of kink bands can be used to determine which slip system is active in kinked grains (Christie et al., 1964; Raleigh 1968). The morphology can also be used to infer the compression direction acting upon each kinked grain, which is how they will be used in this study.

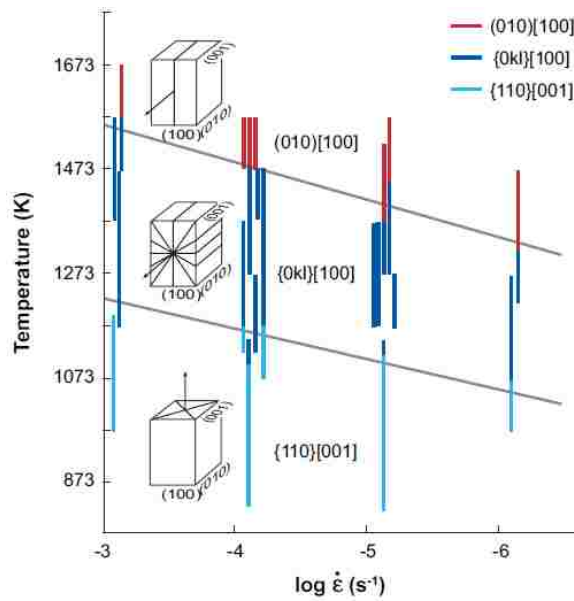


Figure 7. Active slip systems as a function of strain rate and temperature. Pressure is constant at 1.5 GPa, modified by Karato et al. (2008) from Carter and Ave'Lallemant (1970).

Kink bands form due to a buckling instability which is a consequence of the single crystal inability to accommodate strain via dislocation glide in the axial directions (Burnley et al., 2013). During the formation of a kink band, dislocation glide occurs on a plane orientated at a very low angle or parallel to the applied stress, thus providing motion on a prominent slip system which has little to no resolved shear stress at the initiation of slip (Lenze et al., 2005). There are three important components of a kinked grain, the kink band boundary, glide plane and rotation axis, which are traditionally used in the determination of active slip system, see (Fig. 8; Christie et al., 1964). During slip along the slip plane, the glide direction will form normal to the kink band boundary, and portions of the crystal inhomogeneously slip which causes rotation about an axis defined by the intersection of the slip plane and kink band boundary (Raleigh, 1968). By

determining the orientation of the rotation axes in a kinked grain, the compression direction can then be inferred (Lenze et al., 2005). A study conducted by Burnley et al. (2013) analyzed kinked grains in deformed Mg_2GeO_4 olivine using EBSD, (Fig. 9). In this figure the kinked grain can be visually identified in photomicrograph and EBSD orientation map by the distinctive crystallographic domains separated by sub-parallel fractures. The pole figures from the kinked grain can be used to determine the rotation axis; data points on the [010] plot show a superposition of poles, while the [100] and [001] poles are distributed along great circles. This trend is indicative of rotation about [010], and since the [001] poles are at low angle to compression, the [001] is identified as the compression direction (Burnley et al., 2013). In this study, the same technique will be used to determine the local compression direction for each kinked grain identified in the deformed olivine samples.

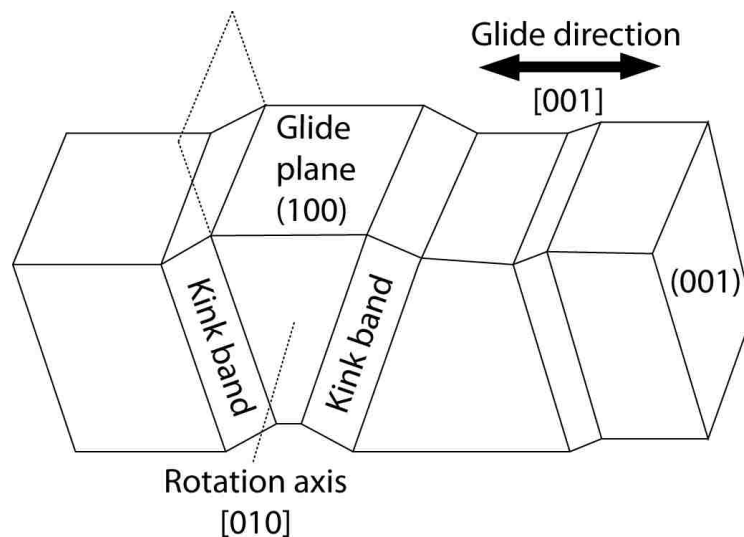


Figure 8. Elements of a kink band in olivine. Notice the rotation axis is normal to the glide direction and parallel to the intersection of the kink band boundary and glide plane from Lenze et al. (2005).

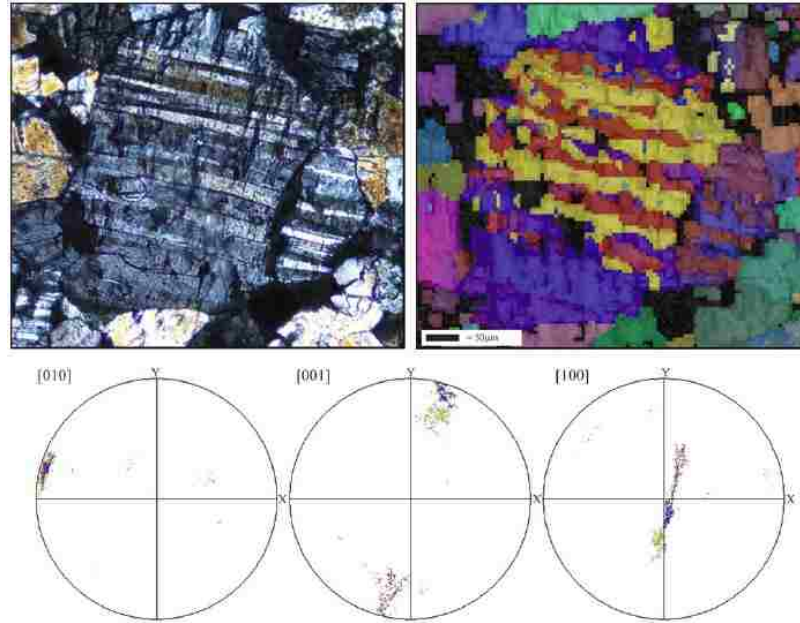


Figure 9. Kinked magnesium germanate grain imaged using EBSD. Mg_2GeO_4 grain photomicrograph (upper left), and a EBSD map (upper right). Notice the different orientation domains separated by sharp sub-parallel fractures. (lower half) The [010] axis show a superposition while the [100] and [001] poles are distributed along great circles. Experimental compression is in the vertical, figure from Burnley et al. (2013).

Calcite

Calcite twins have been utilized to provide information on both the stress direction and incremental strain in deformed rocks since the early descriptions of their morphology in works by Turner, (1953); Groshong, (1972) and Spang (1972) (Burkhard, 1992). Since these early works many alterations have been made to the classic method of stress analysis via calcite twin morphology which include: weighting the amount of twinned grains to calculate relative stress magnitudes (Spang, 1972), determining intragranular twin density as a proxy for shear strain (Groshong, 1984) and the evaluation of negative expected values (NEV) which measure the homogeneity of strain in a twin data set in relation to a

theoretically predicted strain tensor calculated only using the twin set with the highest Schmid factor (Pfiffner and Burkhard, 1987) (Burkhard, 1992). For the purpose of this study only the modulation of local stress directions is of importance, and since the values of temperature, pressure and macroscopic stress are measured during the experiment, the classic technique of determining compression direction by use of the c-axes and twin composition plane of each grain will be adequate.

Deformation twinning in calcite aggregates is the most dominant deformation mechanism during low temperature/low stress deformation due to the extremely low critical resolved shear stress of ~ 30 bars at less than 350°C (Wenk et al., 1973). Above this temperature the role of deformation twinning is minimized and strain is either accommodated by recrystallization or dislocation glide on r-planes $\{10\text{-}11\}$ and f-planes $\{02\text{-}21\}$ (Fig. 10; Rybacki et al., 2013; Wenk et al., 1973). The twinning system is defined by the composition plane, or e-plane $\{01\text{-}12\}$, and the twin direction which is defined by the intersection of the e-plane and the cleavage plane $r\{10\text{-}11\}$, see (Fig. 11a). The c-axis, pole to the e-plane and glide direction in a twinned grain are coplanar with respect to the preferred compression and tension axes, and the twin geometry can be seen in (Fig. 11a) (Laurent et al., 2000; Tielke, 2010; Jang et al., 2012). In a host grain the angle between the c-axis and e-plane pole is 26° , after the grain twins the c-axis is rotated to the opposite side of the e-plane pole by 26° in the twinned domain, creating an angular misorientation between the host and twin c-axes of 52° (Fig. 11b; Spang, 1972; Groshong, 1972; Burkhard, 1993). It is important to

note that due to the trigonal symmetry of calcite, twinning may occur on any of the three $\{10\bar{1}1\}$ planes, and with large amounts of strain multiple twinning planes can be activated simultaneously (Burkhard, 1993). Multiple twin sets in a single grain complicates the determination of a single compression direction based of the twin morphology, and thus high strains were avoided during deformation experiments.

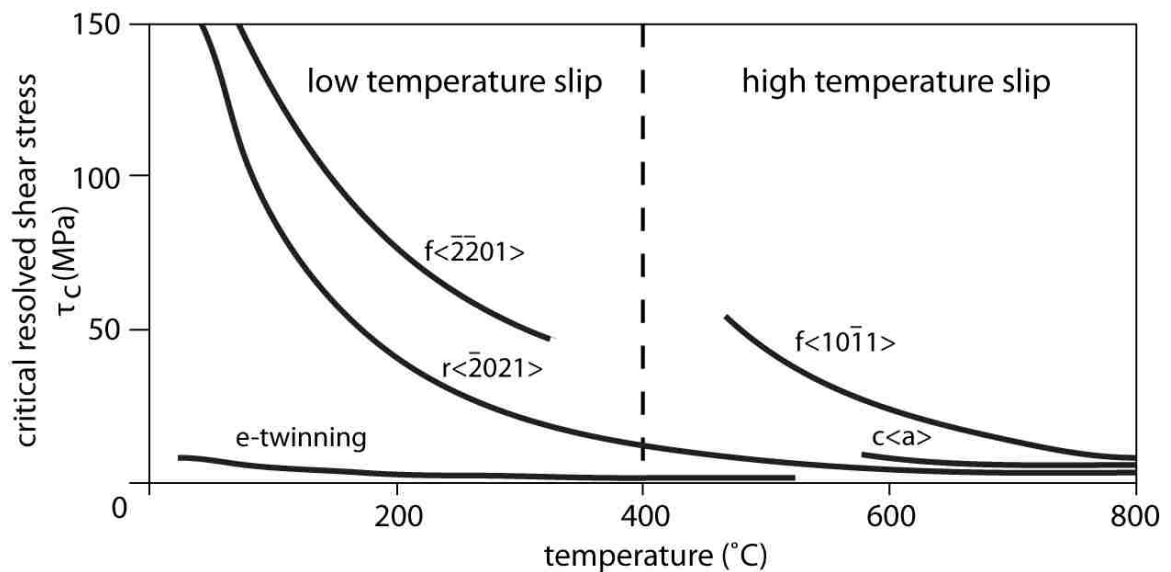


Figure 10. Slip systems in calcite as a function of temperature and CRSS. Notice the very low stress required to activate e-twinning compared to dislocation glide in the low temperature slip regime modified from Rez and Melichar (2010).

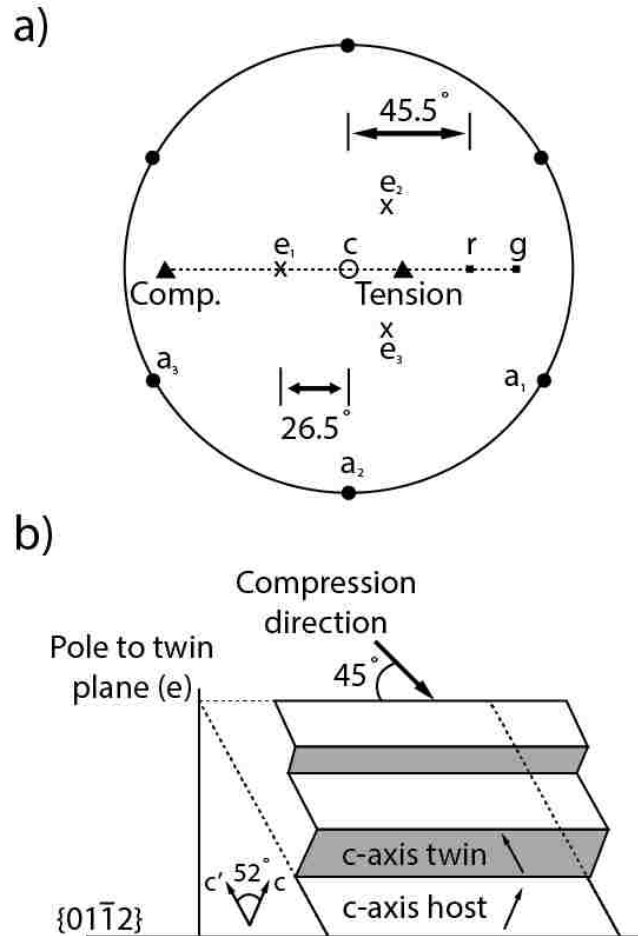


Figure 11. (a) Stereonet showing main components of e-twins in calcite. C-axis is in center with the three e-plane poles distributed around by 120° due to the trigonal symmetry of the single crystal. The angle between the e-plane pole and c-axis is 26° , with compression being 45° from the e-pole. The pole to the cleavage plane is indicated by r, and g is the glide direction for the e_1 twin system, modified from Burkhard (1993). (b) Schematic cross section of calcite twin. The stippled box represents the host grain with the grey regions as twinned orientations, modified from Spang (1972).

Stress and strain analysis utilizing calcite twins in natural samples use a large number of twins to calculate an average stress or strain tensor acting on a regional scale. (Fig. 12) from Spang (1972) spread shows just one of these classic studies in which 50 twinned calcite grains have been analyzed by taking advantage of the coplanar relationship between compression, tension, e-plane

pole and c-axes of the twin and host (Spang, 1972). Using a u-stage, compression direction is calculated from each twinned grain and plotted on a stereonet. By averaging the calculated compression direction vectors, a single stress vector is determined which is produced from the entire population of twinned grains (Burkhard, 1993). In (Fig. 12) it can be observed that the calculated compression directions show a spatial distribution away from the determined macroscopic stress direction. Understanding this spread in compression data is the main objective of this study, and has not been addressed by any of the previously mentioned authors. By modifying the classical technique of calcite twin analysis by using EBSD and a known applied macroscopic stress direction the deviation in local stress directions can be accurately determined and compared with other minerals.

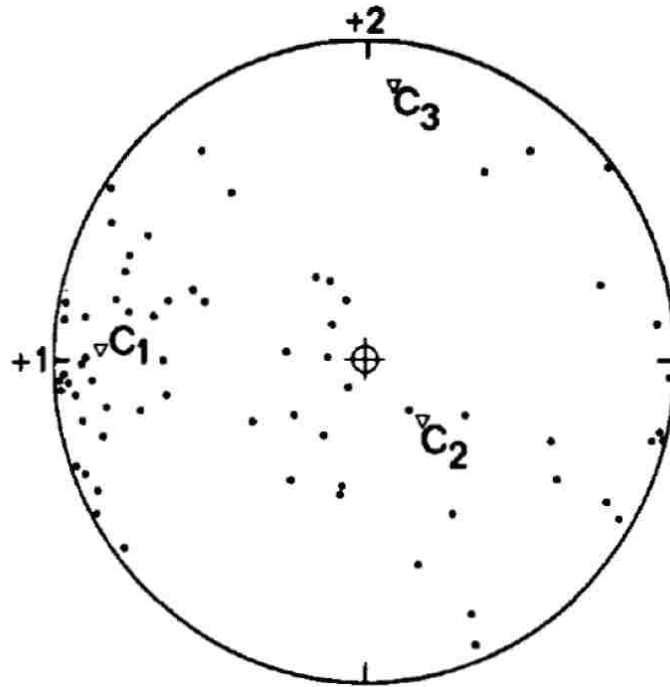


Figure 12. Calcite paleostress calculation using eigenvector analysis. Equal area stereographic projection with the calculated compression direction from 50 twinned calcite grains. C_1 , C_2 and C_3 are representative of the calculated eigenvectors for the data set which correspond to the principal directions of the macroscopic stress tensor, with $C_1 = \sigma_1$, $C_2 = \sigma_2$ and $C_3 = \sigma_3$, from Spang (1972).

CHAPTER 3

METHODOLOGY

This study utilized a number of different experimental and observational techniques. Two types of deformation apparatuses were used in the experimental portion of this study: a modified Griggs type piston cylinder apparatus and the deformation-dia multi-anvil press. After deformation, scanning electron microscopy (SEM) along with electron backscatter diffraction (EBSD) was performed at either Electron Microanalysis and imaging Laboratory (EMiL) located at the University of Nevada Las Vegas, or the microscopy lab located at University of California Santa Barbara. In addition to the deformation experiments, finite element models were also used to better constrain local stress direction modulations during polycrystalline deformation.

Griggs apparatus

The Griggs machine is a modified piston cylinder apparatus. This apparatus allows for the independent pressurization and deformation of a sample by using both a hydraulic ram (for pressure) and deformation piston in line with a loading column (for deformation) (Griggs, et al., 1960). Temperature is monitored by a single side entry type S thermocouple (100% Pt/ 90%Pt 10% Rh). Signal from the thermocouple is routed directly into the data acquisition system where it is treated with a built in cold-junction compensator. A pressure correction has not been applied to the recorded temperature because the findings of Lazarus et al. (1971) indicate that at the largest correction that would be appropriate for a type S thermocouple is approximately $0.6^{\circ}\text{C}/\text{kb}$ at 800°C , a negligible deviation for the

purpose of this study. Differential stress is recorded from a load cell that is attached directly to the loading column and upstream of the deformation piston. Attached to this load cell are two horizontal supports that secure the linear variable differential transformer's (LVDT) that record the vertical position of the deformation piston, and are used in the determination of strain in-situ.

Confining pressure data is acquired from an Omegadyne pressure transducer, which records the pressure within the lines that supply oil to the top of the hydraulic ram. In order to determine the confining pressure on the sample we use the factory calibration to convert the mV output from the transducer to psi. Oil pressure is applied to the top of the hydraulic ram, so a conversion is made between this surface area and the surface area of the confining pressure piston directly below to provide the actual sample pressure.

There is a source of error within this pressure reading that is caused by the internal friction within the hydraulic ram. Inside of the ram there is a large O-ring that seals oil in either the upper or lower portion of the ram. As the ram is pressurized and oil is transferred from the lower reservoir to the upper, the friction of this O-ring will produce a slight increase in recorded pressure. This contribution can be described by the following relationship: *recorded pressure = confining pressure + internal friction within the ram*. Currently the total contribution of this friction to the value of recorded pressure is not known for this specific Griggs machine, but Burnley and Getting, (2012) have shown that deviations between actual and recorded pressure can be up to 10%. All data from the Griggs machine instruments are recorded using an Omega engineering

data acquisition system (OMB-DAQ-2416-4AO). This suite of data includes: temperature, pressure, differential stress and LVDT position. Data is recorded at a frequency of approximately 2 Hz and to an accuracy of 10^{-7} volts; combining this with the uncertainty of each instrument we can achieve accuracy within 1°C, <0.1mPa for pressure, <0.01mPa for differential stress and .01mm in deformation piston position.

Calcite deformation (Griggs)

Starting material and sample assembly

For calcite deformation experiments Solnhofen limestone (Upper Jurassic, Bavaria) was chosen as the starting material because of its very homogeneous grain size (~10 μ m) and microstructure free grains (Barber and Wenk, 1973). This specific limestone has been used for calcite deformation experiments for these same reasons since the mid 1970's (Barber and Wenk, 1973; Wenk et al., 1973; Rybacki et al., 2013). The homogenous small grain size ensures the stress field in the sample is not complicated by the presence of anomalously large grains, and also maintains adequate grain statistics in the deformed aggregate.

Calcite samples were cored from a block of Solnhofen limestone, provided by Dr. Eric Rybacki from the Helmholtz Centre Potsdam, using a 1/4 inch diamond core drill. Cores were then cut into 15 mm long cylinders using a slow speed diamond saw and inserted into a Cu jacket before being placed into the Griggs sample assembly (Fig. 13). The jacketed calcite was then placed into a NaCl sleeve along with two alumina pistons used for creating the differential stress on top and bottom of the cylinder. The jacketed sample and pistons were

then placed inside of a graphite sleeve used for resistive heating. The furnace assembly and sample are placed into a pressure media of larger NaCl rings and placed on top of the bottom tungsten carbide piston. A Pb plug is used on the top to transfer load from the ram to the NaCl and a Cu ring is inserted in between the Pb and NaCl for a furnace contact. A Pb plug is used on the top to transfer load from the ram to the NaCl and a Cu ring is inserted in between the Pb and NaCl for a furnace contact.

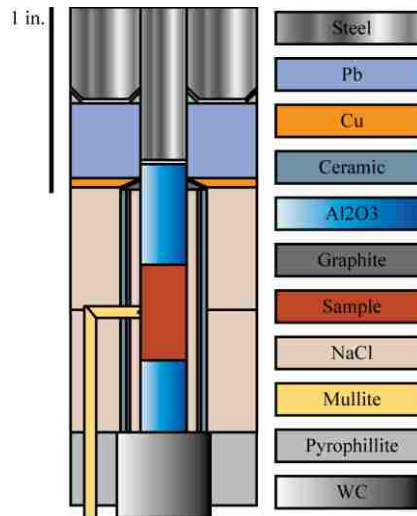


Figure 13. Diagram of the Griggs modified piston cylinder sample assembly. Sample is calcite core with a Cu jacket. NaCl is used as the pressure media and heated through the use of a vertical graphite furnace. Temperature is monitored through a single side-entry Pt/Rh (type-S) thermocouple which is inside the mullite insulation.

Experimental procedure

Samples were brought up to pressure over a 24 hour period. This allowed plenty of time for the NaCl to creep, and prevented any stress concentrations within the assembly that could prematurely produce deformation twins and biased microstructures. After the desired pressure was reached the temperature was increased at a rate of approximately $1/4 \text{ } ^\circ\text{C sec}^{-1}$ until reaching the run temperature, see run conditions in (Table 2). When the sample reached pressure and temperature the deformation piston was engaged at a constant rate which

produces a sample strain rate of $1.0 \times 10^{-3} \text{sec}^{-1}$ until the deformation piston made initial contact with the sample. Once contact is made the deformation piston is immediately stopped and the motor reversed for approximately one minute so the piston is no longer touching the sample. This provides an opportunity to slow the motor down to the experimental strain rate of 1.0×10^{-4} before the motor is engaged again for the deformation. During deformation sample strain is monitored in-situ by the two external LVDT's and a feeler gauge which are attached to the piston. Upon reaching the target strain the motor is stopped and the sample is quenched to preserve deformation microstructures; then the motor is reversed at 1.0×10^{-3} and pressure is bled off at roughly 2 kb/hour.

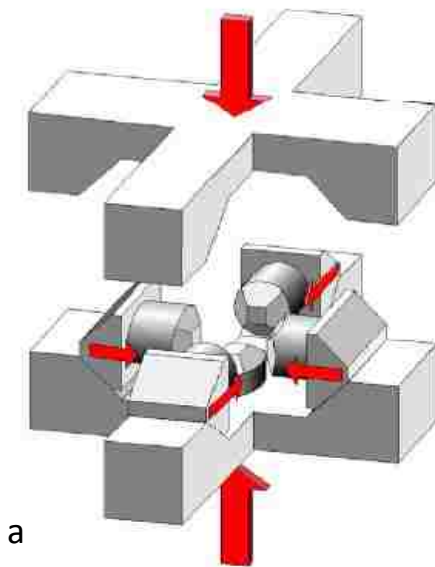
Table 2
Summary of conditions for calcite deformation experiments

Sample	Temperature (°C)	Pressure(kb)	$\dot{\epsilon}$ (sec ⁻¹)	Total ϵ (%)
Sfn_002	300	2.5	1.0×10^{-4}	14
Sfn_004	200	2.5	1.0×10^{-4}	16

D-DIA experiments

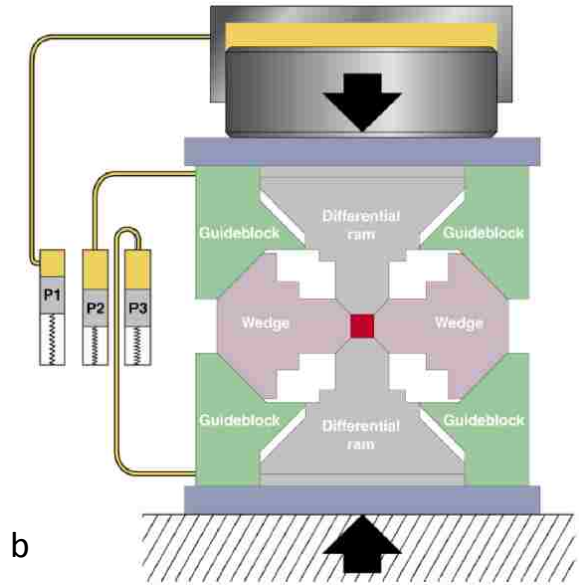
D-DIA experiments were conducted utilizing beam line X-17B2 at the National Synchrotron Light Source. Using a synchrotron beam line allows in-situ x-ray diffraction data during deformation experiments which is used for stress and strain measurements. The D-DIA is a type of multi-anvil deformation apparatus that uses 6 cubically arranged anvils to provide independent pressurization and deformation of the sample. (Figs. 14a and 14b) Shows the geometry of the six anvils in relation to the two guide blocks that are used to

pressurize the sample, one anvil in each guide block in the vertical, and four arranged opposing at 90° in the horizontal, making a cubic arrangement. As noted in Durham et al. (2003), the back side of each horizontal anvil comprises two faces of a virtual octahedron (Durham et al., 2003). By the symmetry imposed from the advancing guide blocks and anvils, all axes of the virtual octahedron are then strained equally and thus provide hydrostatic pressure to the sample. In order to create a deviatoric stress, oil is pumped using two differential rams behind the top and bottom anvils located within the guide blocks allowing them to advance independent of the other four, see (Fig. 14ba; Wang et al., 2003). By advancing just one anvil pair, a deviatoric stress is created thus altering the previously cubic stress field to one that is tetragonal. The induced flow is approximately axially-symmetric with respect to the cylindrical sample (Durham et al., 2003, Wang et al). By advancing an anvil pair pressure would begin to increase on the sample as deformation progresses, but the D-DIA has the capability of bleeding off oil from the main ram (p1 in Fig. 14b) while advancing the differential pumps (p2 and p3 in Fig. 14b) in order to maintain a constant sample pressure during deformation (Wang et al., 2003).



a

Figure 14a. D-DIA module, shows how the vertical pressure applied by a hydraulic ram is converted into a six-sided cubic stress field Modified from Wang et al. (2003).



b

Figure 14b. Cross section view of the D-DIA. P1 is the main ram used for pressurization, while p2 and p3 are the differential rams used for deformation, Long et al. (2011).

Pressure and differential stress

The values of pressure and differential stress are obtained from in-situ x-ray diffraction collected during the experiment. Polychromatic x-rays enter the sample through a small gap between the front anvils, then exit through an X-Ray transparent anvil made of either sintered diamond or cubic boron nitride. The diffracted X-rays then passes through a double slit system and is collected by a 10 element energy dispersive detector at a 2θ angle of approximately 6.5° . Spectra are collected in 60 second intervals for 5 cycles on the sample, then repeated on the crushable alumina piston. Before analysis each block of 5 spectra are added together to provide a greater intensity. This type of processing allows a more detailed analysis of the rapidly changing stress state in the

beginning of the experiment if needed. Once the spectra are compiled, peaks are identified and fit using a program provided by the beam line called Plot 85 to determine d-spacing values for each (hkl). D-spacing values are then used to determine the evolution of lattice strain throughout the experiment. Values of strain can be obtained by comparing the values of d-spacing from each diffraction pattern to a hydrostatic diffraction pattern collected before the deformation began. This is shown in (Equation 3), where d_{hkl} is the hydrostatic value of d-spacing and $d_f hkl$ is the values of d-spacing calculated from each diffraction pattern.

$$\epsilon_{\text{lattice}} = \frac{d_{hkl} - d_f hkl}{d_f hkl} \quad \text{eq. 3}$$

The pressure on the sample was also calculated from diffraction data by using the measured temperature and calculated cell volume in conjunction with a third-order Birch–Murnaghan equation of state program from Ross Angel of the University of Padova called EosFit 6.0.

Strain and strain rate

Sample strain and strain rate are calculated from X-Ray radiographs collected after each block of 5 spectra. Radiographs are produced by imaging fluorescence of the transmitted beam by a YAG crystal with a CCD camera (Fig. 15). In the radiograph the sample is visible along with two Pt foils placed on either end. In-situ strain is measured in the axial direction by monitoring the distance between the Pt foils during deformation. Strain rate is then calculated by plotting the values of strain as a function of time.

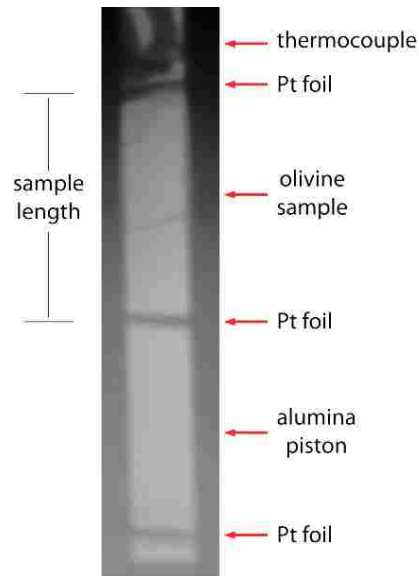


Figure 15. Radiograph taken through the anvil gap in the D-DIA. This image shows the long axis of the deforming sample, which is parallel to compression, and the Pt foil strain markers. Using the foils, strain is calculated in-situ.

Olivine deformation

Starting material and sample assembly

Phenocrysts of San Carlos olivine (Fo_{90}) were used as a starting material for olivine deformation experiments. The phenocrysts were approximately 1cm in diameter and optically free of oxidation. The grains were crushed and ground using a corundum mortar and pestle. The powder was packed into a Ni jacket along with an alumina piston and Pt foil markers on either end of the olivine powder (Fig. 16). The Ni jacket not only contains the powder, but also helps control the oxygen fugacity of the sample. The Ni jacket is then placed into a hexagonal boron nitride sleeve that acts as a pressure media. This sleeve is then placed into a graphite sleeve which is used as a resistive heater. Temperature is monitored by a single top entry Pt/Rh thermocouple which is threaded through alumina insulation and placed directly above the Ni jacket. The thermocouple

insulation is cemented with zirconia glue into an alumina ring which allows it to be used as a piston.

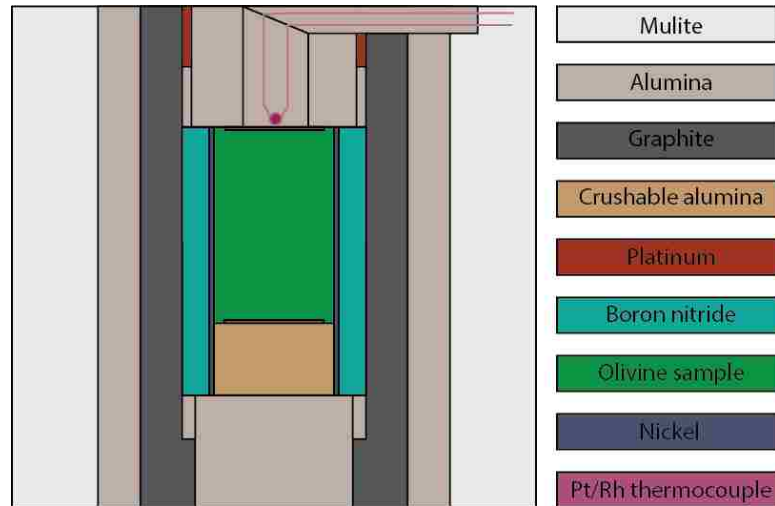


Figure 16. Diagram depicting the D-DIA sample assembly. Outer mullite is a sphere which fits into 2 pyrophyllite seats forming a cube that fits inside the D-DIA assembly shown in Figure 14a

Experimental procedure

Olivine samples were brought up to the desired run pressure at a rate of approximately 5kb/hour at room temperature. Once pressure was reached the samples were heated to an annealing temperature of $\sim 1100^{\circ}\text{C}$ for approximately 2 hours. During the annealing the differential motors were engaged at 0.5mm/sec until the oil pressure from the differential lines indicated that a load was being applied to the sample. This step ensures that deformation can begin immediately once the final experimental conditions are reached. Temperature was then dropped to run conditions and diffraction patterns were taken to ensure the sample was at hydrostatic conditions before starting the deformation. Then the motor was slowed down to advance at only $2\mu\text{m}/\text{sec}$ and deformation began.

Once the deformation was complete the sample was quenched to preserve any microstructure and the sample was unloaded by retracting the main and differential rams. A summary of experimental conditions for olivine deformation can be seen in (Table 3).

Table 3
Summary of conditions for olivine deformation experiments

Sample	Temperature (°C)	Pressure(GPa)	$\dot{\epsilon}$ (sec ⁻¹)	Total ϵ (%)
San_197	700	5.0	1.45×10^{-5}	15.5
OI_412	900	4.5	2.0×10^{-4}	35 [†]

[†]Indicates approximate value due to lack of in-situ x-ray diffraction

Electron backscatter diffraction

After deformation each cylindrical sample was mounted in epoxy and cut parallel to the direction of applied stress. The cut surfaces were then manually polished using diamond grit in the following steps: 9 μ m, 6 μ m, 3 μ m, 1 μ m, 0.5 μ m and 0.25 μ m. This was then followed by a final polish on a Buehler Vibromet2 vibratory polisher using a 0.05 μ m, basic colloidal silica solution for approximately 12 hours. The vibratory polish is a critical step for preparation of samples that are to be analyzed using EBSD, as it removes any surface damage and dislocations that have been introduced in the sample by the manual polishing procedure. Without removing these surface dislocations, Kikuchi patterns appear less sharp and indexing rates drop (Maitland and Sitzman, 2007). In order to prevent charging, all samples were dried in a vacuum oven before a 0.5 nm carbon coat was applied using an evaporative coater. Samples that were carbon coated were

then dried again in the vacuum oven before being placed in the SEM for EBSD analysis.

EBSD orientation maps were produced on one of two scanning electron microscopes (SEM). This first instrument is a JEOL JSM 6700F field emission scanning electron microscope (FESEM) equipped with an Oxford Nordlys II EBSD detector located at the University of Nevada Las Vegas EMiL lab. The second is a FEI Quanta 400f field-emission, environmental scanning electron microscope located at the University of California Santa Barbara. Post processing of OIMs was completed using the HKL technologies software suite, Channel 5. A summary of run conditions for all EBSD maps is seen in (Table 4).

Table 4
Summary of EBSD map acquisition settings

sample	stepsize	bands	hough resolution	reflectors	MAD limit	lab
San_197	0.5	5-6	80	65	1.3	UCSB
OI_412	0.5	5-6	80	56	1.3	UCSB
Sfn_002	0.5	6-7	60	60	1.3	UNLV
Sfn_004	0.5	6-7	60	60	1.3	UNLV

*lab refers to which institution was used to produce the EBSD orientation maps.

EBSD orientation data are produced by analyzing a specific type of diffraction pattern known as an electron backscatter diffraction pattern (EBSP), which is composed of intersecting lines known as Kikuchi bands. Kikuchi bands are produced by inelastic scattering of electrons along crystallographic planes within the crystal that have met the Bragg condition ($n\lambda = 2d_{hkl} \sin\theta$), and the

intersections of these bands are representative of the zone axes (Maitland and Sitzman, 2007). EBSD orientation maps are created by rastering the electron beam in the SEM across a sample that was been mounted at a high tilt (70° from the beam normal) and at each point in the raster, or step, a diffraction pattern is produced see (Fig. 17). The diffraction patterns from each step are collected using a phosphorus screen in conjunction with a charge-coupled device (CCD) camera within the EBSD detector. After the collection of each EBSP pattern, the software automatically indexes each pattern by first converting the linear data within the EBSP to point data by using a Hough transformation. Once this transformation is complete the diffraction data is compared to the known standard for the material (referred to as a match unit) that is being analyzed. From this data a 3-D orientation is assigned along with a value of mean angular deviation (MAD) for each step (Maitland and Sitzman, 2007). MAD values indicate the angular deviation of the diffraction pattern in reference to the known standard and are a measure of the goodness of fit. See (Table 4) for MAD value thresholds and match units used in each map. These discrete steps that contain 3D orientation data become the individual pixels that comprise the EBSD orientation image map (OIM). All crystal orientation data is recorded using Euler angles according to the Bunge convention (φ_1 , Φ , φ_2) with respect to the sample coordinate system.

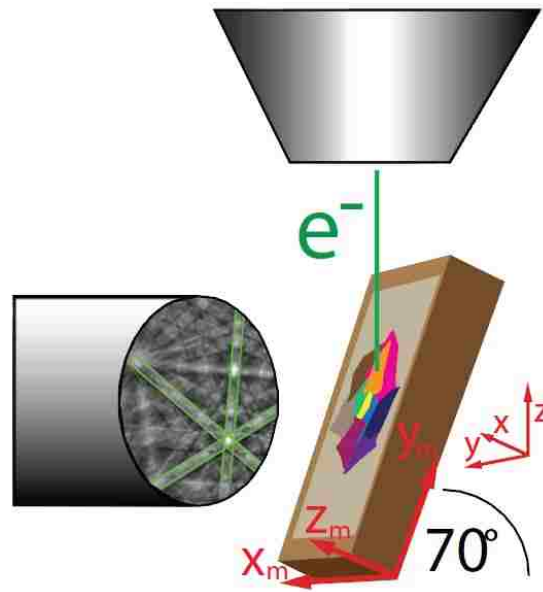


Figure 17. Geometry of EBSD acquisition. Electron beam interacts with sample orientated at a 70° tilt from the beam normal with the EBSD detector directly adjacent to the sample. X,Y and Z indicate the FESEM coordinate system while X_m, Y_m and Z_m indicate the sample coordinate system.

Post-Processing began with the reduction of noise within the raw orientation maps. This procedure started with the alteration of erroneous data points referred to as "wild-spikes". These pixels are defined as a single pixel surrounded on all sides by pixels sharing an orientation different from that of the center pixel. Wild-spikes are eliminated by averaging the orientations of all 9 neighboring pixels and assigning that orientation to the original wild-spike (Maitland and Sitzman, 2007). After the removal of wild-spikes, additional data refinement was completed to eliminate further noise. This process involved altering the definition of what a wild-spike is to include pixels where only 8 of their 9 neighbors deviate and then repeating the process (Fig. 18). These steps have

been shown in the literature to smooth the data without the addition of erroneous data. A detailed description of this process can be found in Hansen et al. (2012).

Olivine samples require further noise reduction due to a systematic misindexing of the EBSP's by the EBSD software. The misindexing is a product of the pseudo-three fold rotational symmetry about the [100] in the olivine Kikuchi pattern produced by the fcc arrangement of the oxygen sub-lattice within the olivine structure (Bystricky et al., 2006; Hansen et al., 2012). Systematically misindexed points are easily identified visually, refer to (Fig. 18). They are removed as normal practice in the grain detection procedure by ignoring high-angle grain boundaries with rotations of 60° increments along the [100] (Bystricky et al., 2006; Hansen et al., 2012).

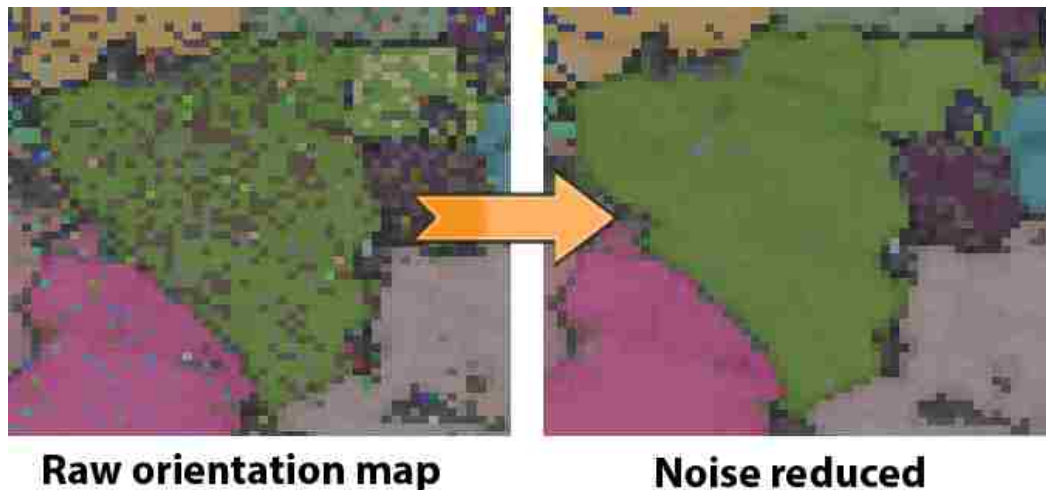


Figure 18. Noise reduction process in EBSD maps. The left side of the figure shows a portion of a raw EBSD map of olivine. Bright colored single pixels within the green grain are noise, while dark brown pixels are systematically misindexed points. The right side shows the same portion of the map that has been properly noise reduced by means of the next neighbor technique, as well as the elimination of systematically misindexed rotations about the [100]

Finite element models

Construction and physical properties

Finite element models were constructed using MSC.MARC Mentat, a commercial engineering finite element program. Each material was modeled as a rectangular array of 2,574 hexagons, see (Fig. 19). Each hexagon was divided into 48, 6-noded elements. Nodes along the boundaries of each hexagon are shared with the neighboring hexagon, thus displacement along the hexagon boundaries is not permitted. This model geometry is the same as used in the Burnley (2013) study, and a detailed description can be found within. The hexagons were divided into 14 populations down from the original 25 of the original Burnley models, then assigned different mechanical properties in order to simulate randomly orientated single crystals distributed throughout a monophasic polycrystal. The elastic tensors were produced by rotating the full elastic tensor of each material by specific Euler angles and since the orientation of each grain is known the critical resolved shear stress of each slip system can be calculated using the Schmid equation and a yield stress accurately assigned to each population, see (Fig. 19) for an example. (Table 2) shows what Euler rotations were applied to each materials stiffness matrix to produce the 14 different subpopulations in each FEM.

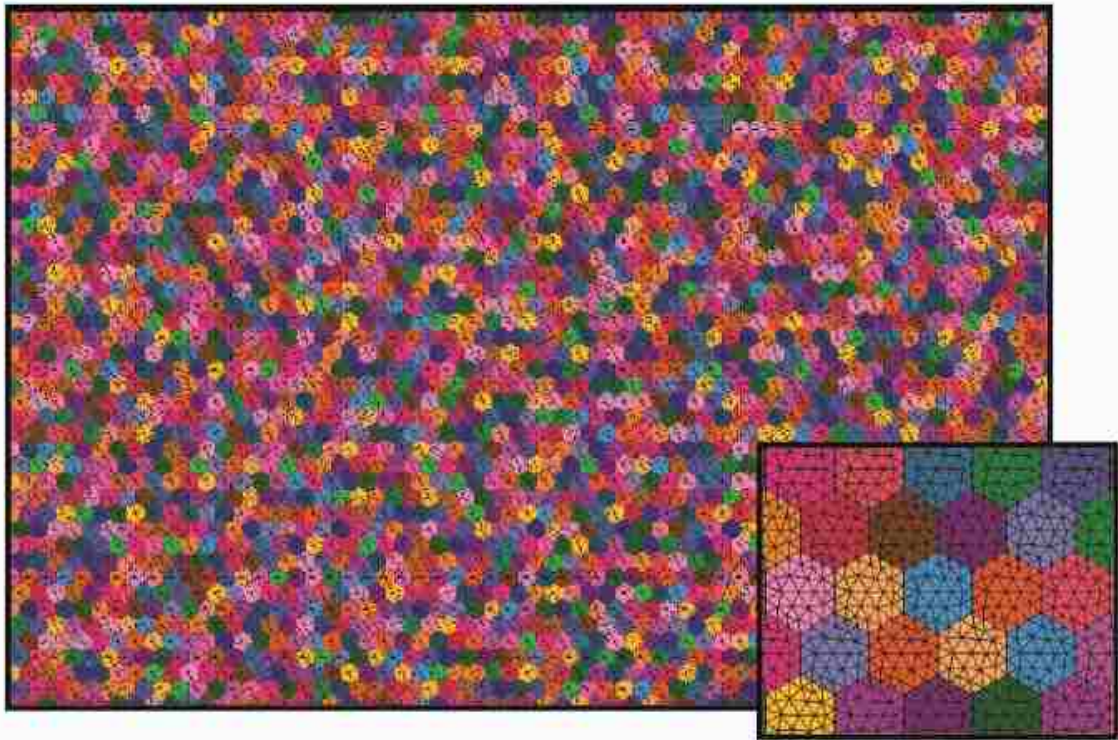


Figure 19. Finite element mesh with grain populations. The finite element model geometry of each material before deformation. Each color represents 1 of the original 25 populations from the Burnley FEMs to which physical properties were assigned. The inset is a magnified view which shows the triangular meshing of individual hexagons, from Burnley (2013).

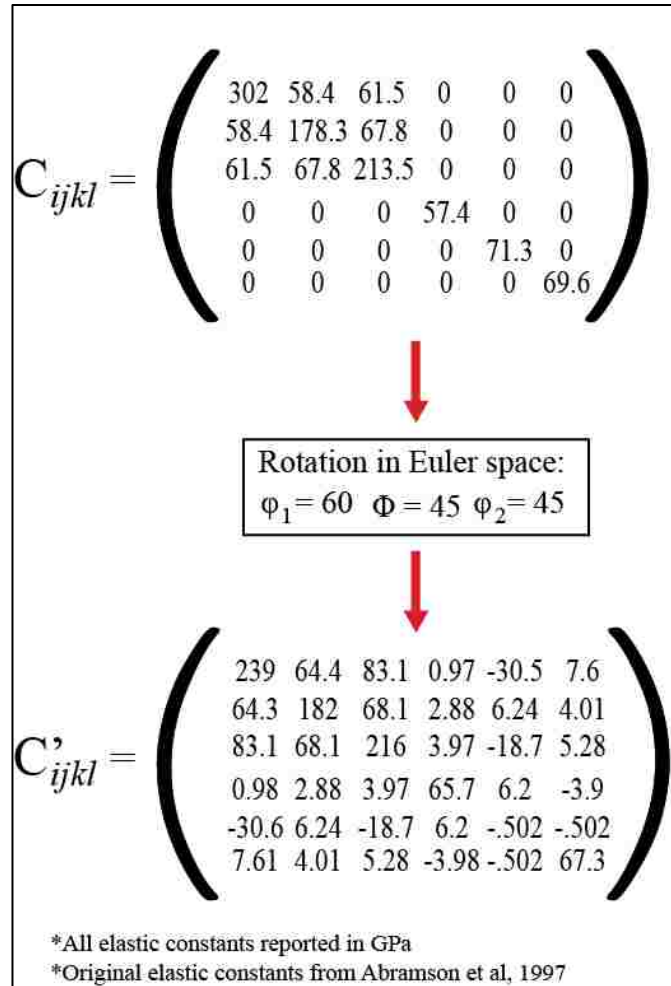


Figure 20. Example of Euler rotations made to elastic tensors. This figure shows one of the 14 different rotations applied to the elastic tensor of olivine. C_{ijkl} is the original tensor from Abramson et al. (1997) and after the Euler rotation C'_{ijkl} is produced which is then used as the elastic properties of one of the fourteen populations of structural elements within the finite element model.

CHAPTER 4

RESULTS

Olivine EBSD analysis

One EBSD orientation image map (OIM) which covered most the sectioned and polished surface was produced from each deformed olivine sample. (Fig. 21) shows photomicrographs of each sample after deformation, sectioning and polish. The locations of the EBSD maps are outlined with a red box. Small representative subsets of each noise reduced OIM can be seen in (Figs. 22 and 23).

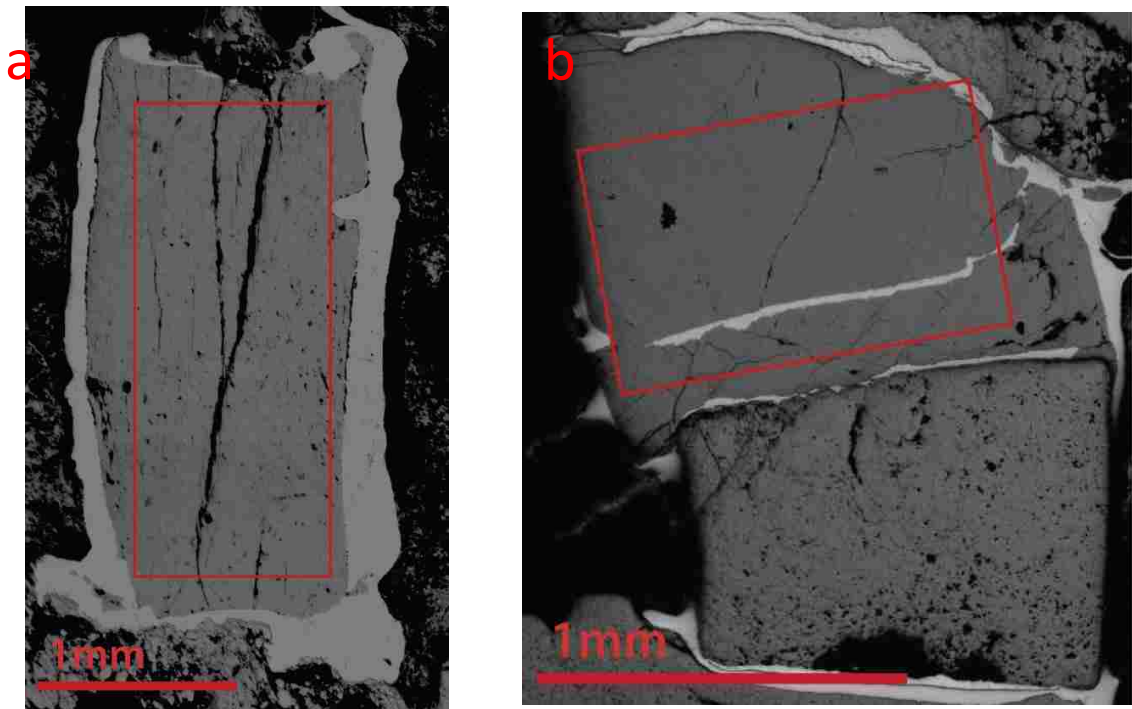


Figure 21. Photomicrographs of deformed and sectioned olivine samples. Red box indicates area where EBSD map was aquired. (a) Photomicrograph of deformed San_197. Deformed to low strain of (15.5%) (b) Photomicrograph of deformed Ol_412. Deformed to high strain of (35%), rectangular shape under the sample is the bottom alumina piston. Compression is in the vertical for both samples

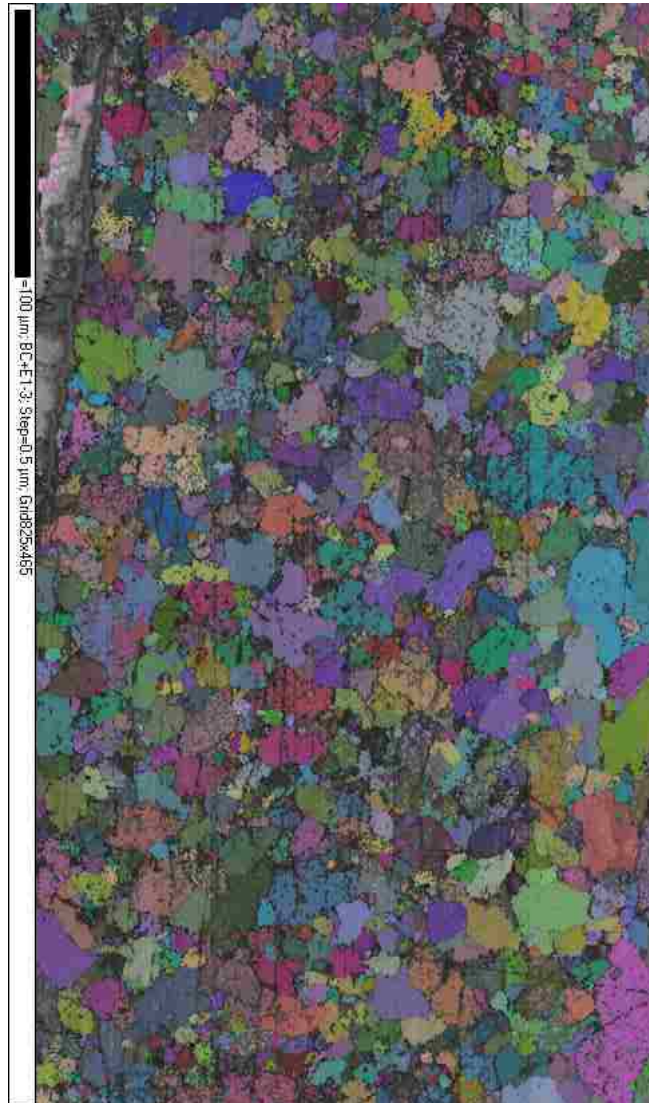


Figure 22. Euler angle coloration on EBSD map of San_197. Euler orientation is shown after noise reduction procedure. Compression is in the vertical direction

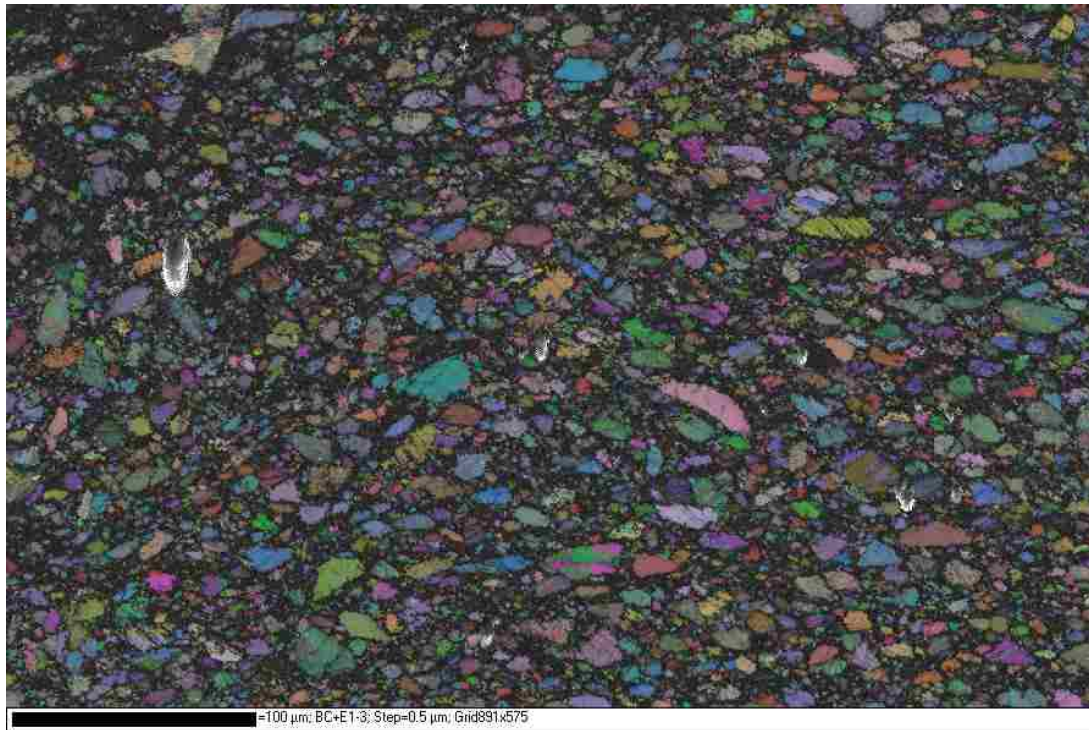


Figure 23 Euler angle EBSD map of Ol_412. Euler orientation is shown after noise reduction procedure. Black areas which surround grains are non-indexed points. Compression is in the vertical direction.

The high strain and low strain olivine OIMs are visually different in terms of grain shape, grain size and indexing rate, especially in regions near grain boundaries in sample Ol_412. Upon seeing how different the physical samples were, the first objective was to understand if the distribution of strain shows any relation to Schmid factors of individual grains.

Olivine Schmid factor and misorientation analysis

Previous authors such as Gennerat et al. (2012) and Farla et al. (2011) have shown that Schmid factor does not provide an accurate prediction of intragranular deformation within deformed aggregates of ice and olivine respectively. To verify these findings in the olivine samples, mean misorientation maps were produced and visually compared to Schmid factor maps. Mean

misorientation maps are a measure of intragranular misorientation angle; values of misorientation are given to each pixel by averaging the orientation of each pixel and the 8 neighboring pixels then determining the deviation away from this average for the central pixel. Since misorientation is caused by the presence of dislocations this type of map is used as a proxy for dislocation density and therefore a measure of intragranular deformation. An example of a mean misorientation map from sample San_197 can be seen in (Fig. 24). Once misorientation maps were made, eight Schmid factor maps were produced from each complete EBSD map from both olivine samples for comparison. Schmid factor maps color each pixel according to its Schmid factor for a given slip system and provides information on which grains are favorably orientated for slip on a given slip system. Each map represents one of the eight slip systems which are observed in deformed olivine; $[100](010)$, $[001](100)$, $[100](001)$, $[100](011)$, $[100](021)$, $[100](031)$, $[001](110)$ and $[001](010)$. Only seven slip systems were analyzed because the slip systems $[100](001)$ and $[001](100)$ produce identical Schmid factors for each grain due to the symmetry of the single crystal (Castenlau et al., 2010). An example of a Schmid factor map for the $[100](010)$ slip system in sample San_197 can be seen in (Fig. 25). Using the deformation mechanism map for olivine from (Fig. 2) it is possible to predict which slip system should be the most dominant during deformation at the experimental conditions, but to ensure all deformation involving all slip systems is accounted for, Schmid factor maps were produced for all slip systems.

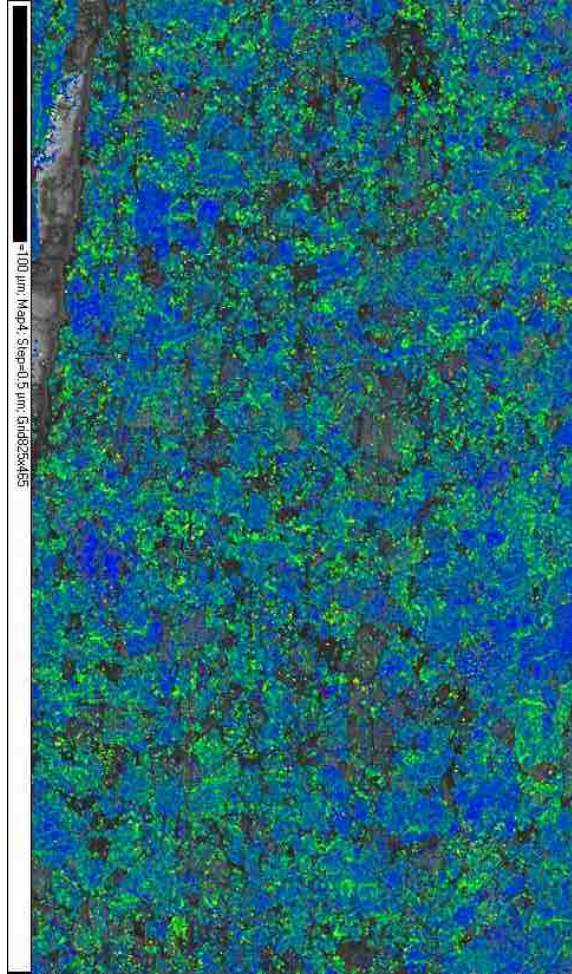


Figure 24. Mean misorientation EBSD map of San_197. Same map subset shown in Figure 22 colored showing the mean misorientation around groups of 3x3 pixels. All nine pixel orientations are averaged then the center pixel orientation is given a misorientation value in relation to the average. No grain boundaries are drawn on the map, but can be inferred by abrupt truncations of areas of differing misorientation.

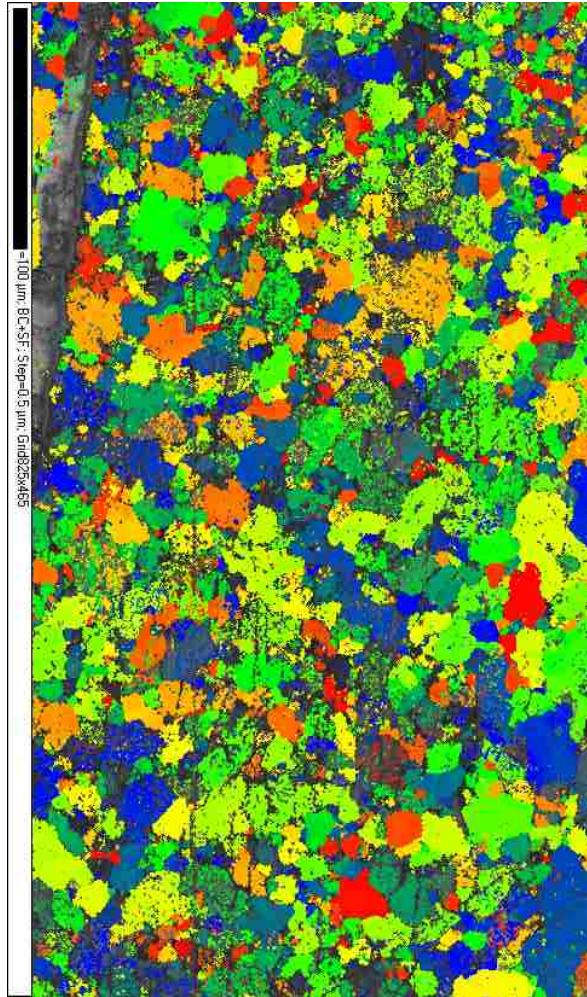


Figure 25. Schmid factor EBSD map of San_197. Same map subset shown in Figure 22 colored by Schmid factor. Rainbow scale is used with blue to red indicating Schmid factor from 0.0 to 0.5 respectively of the [100](010) slip system..

When comparing (Figs. 24 and 25) it can be observed that there is a lack of correlation between Schmid factor and the amount of intragranular deformation. To quantify the relationship between Schmid factor and mean misorientation, graphs were produced that plot the Schmid factor for all 8 slip systems in each grain against the mean misorientation of that specific grain, see (Fig. 26) for this graph from sample San_197. In addition a graph was produced

from this same data set which plots only the highest value of the 8 Schmid factors in each grain against mean misorientation, also in (Fig. 26).

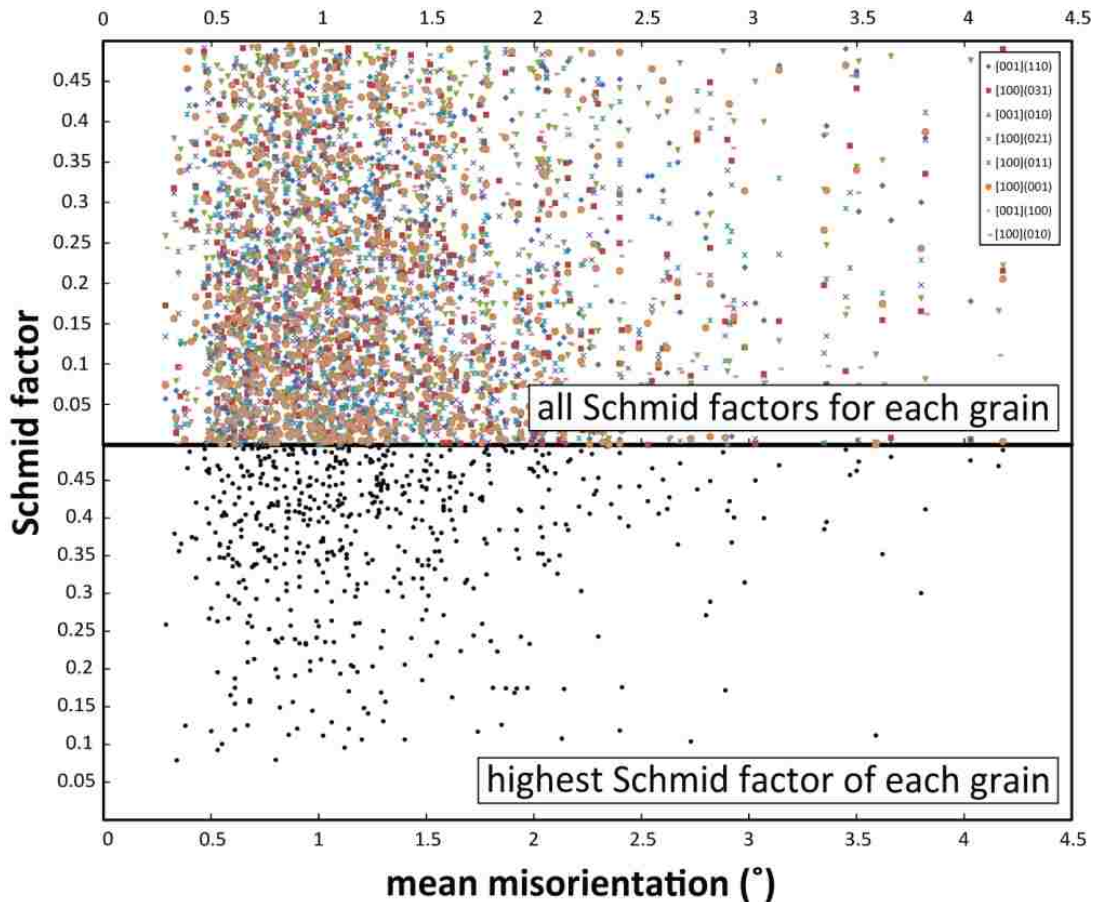


Figure 26. Schmid factor vs. mean orientation. Upper) A plot of Schmid factor against the value of intragranular misorientation for each olivine slip system from sample San_197. Lower) the same grain set from the upper graph but only the slip system with the highest Schmid factor is plotted. Notice the y-axis scale starts at zero when moving to the upper graph. Also, the Schmid factors for the [100](001) and [001](100) slip systems are equivalent due to the symmetry of olivine. Only grains with a diameter > 5 μ m are used.

The upper graph in (Fig. 26) shows no apparent correlation between Schmid factor and mean misorientation. If a correlation was present one could expect to see an increasing value of intragranular misorientation with increasing

values of Schmid factor; instead, it appears that mean intragranular misorientation is independent of changing values of Schmid factor. To further determine the distribution of intragranular misorientation as a function of Schmid factor histograms were then produced by binning Schmid factors by 0.05 and examining the frequency of grains within each Schmid factor population, (Figs. 27 and 28) show these graphs for the [100](010) slip system. This was done to observe in subtle shifts in the mean value of misorientation as a function of Schmid factor, which could not be resolved from (Fig. 26). From (Figs. 27 and 28) it is observed that mean values of misorientation are consistent with changing values of Schmid factor, approximately 1° for San_197 and 1.25° for Ol_412. In addition, it appears that values of misorientation become more diffuse in the higher strain experiment (Ol_412).

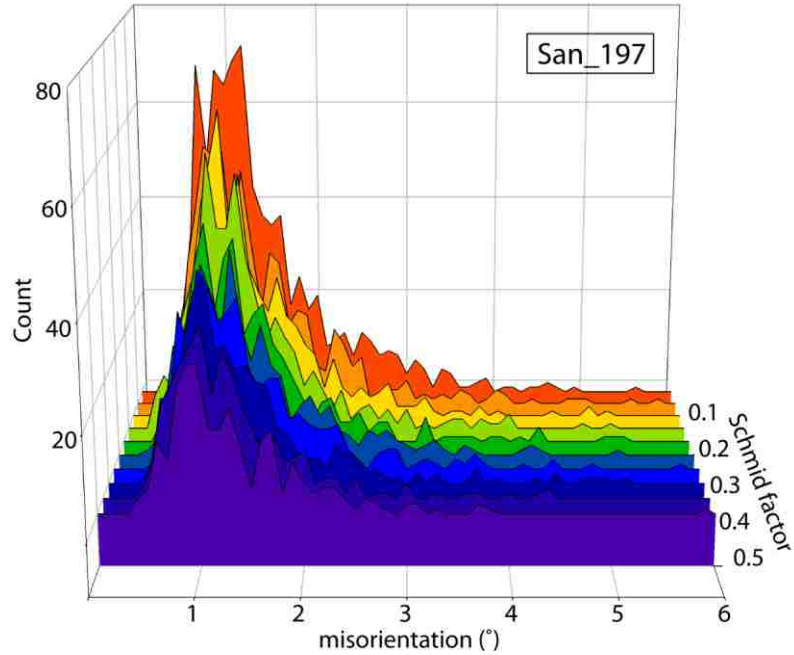


Figure 27. Histogram of mean misorientation in San_197. A graph showing the frequency of a given intragranular misorientation angle throughout sample San_197 plotted as a function of Schmid factor for the [100](010) slip system.

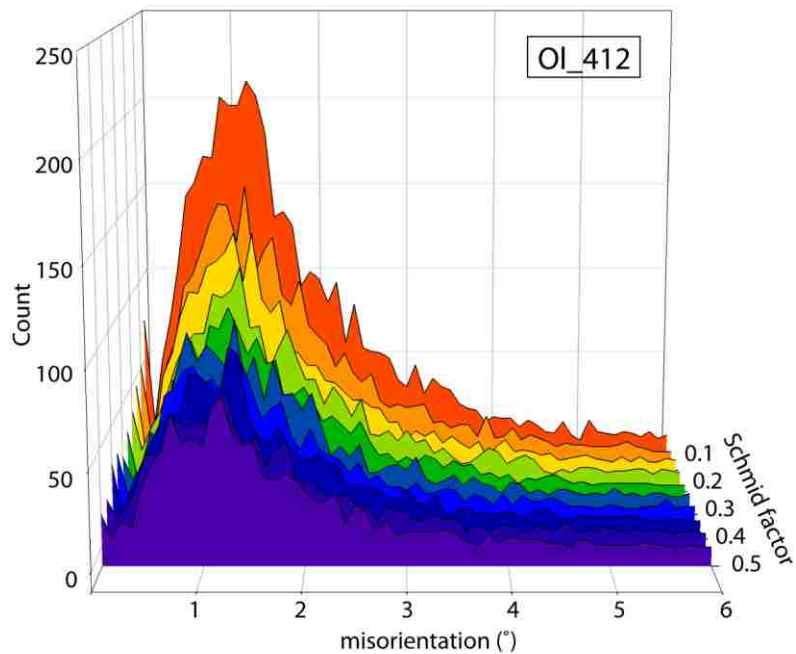


Figure 28. Histogram of mean misorientation in OI_412. A graph showing the frequency of a given intragranular misorientation angle throughout sample OI_412 plotted as a function of Schmid factor for the [100](010) slip system.

Olivine local stress direction deviations

In order to evaluate the degree of variation in the orientation of maximum compressive stress in olivine, kinked grains were identified and analyzed. Kink bands are easily identified in EBSD OIM's because the crystallographic domains within a kinked grain have discrete orientations that are separated by high angle grain boundaries. An example Euler angle EBSD map showing three grains containing kink bands can be seen in (Fig. 29). To confirm each kink band, misorientation angle transects were used in combination a 3-D crystal viewer in the Tango software (part of the HKL EBSD software suite) to verify that each domain is separated by a sharp high angle boundary, and the grain is rotating back and forth about a common rotation axis, seen in (Fig. 30). Kink bands were only observed in the high strain sample OI_412.

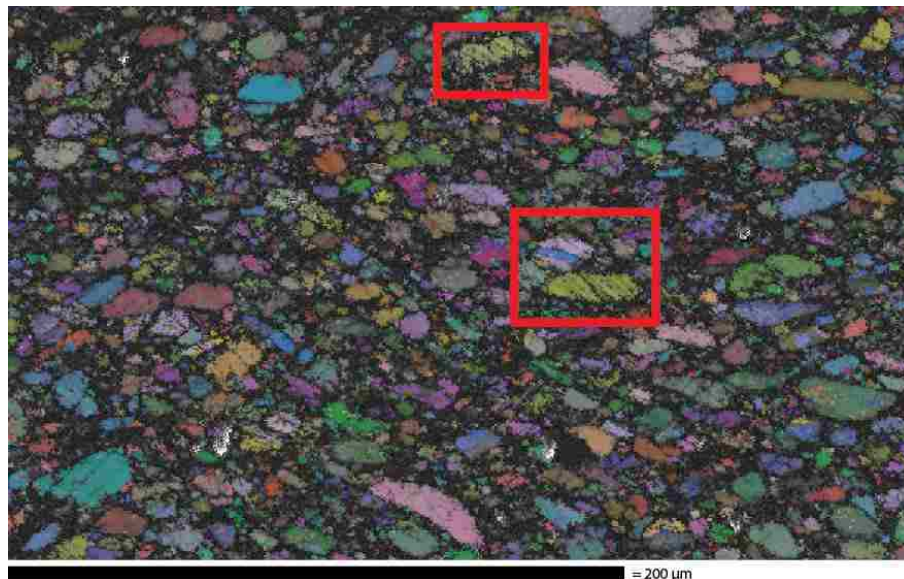


Figure 29. EBSD map of OI_412 showing kinked grains. Three examples of grains with kink bands are outlined with red boxes. Notice the sub-parallel black lines within the kinked grains; these are areas of non-indexing due to fractures. Compression is in the vertical direction.

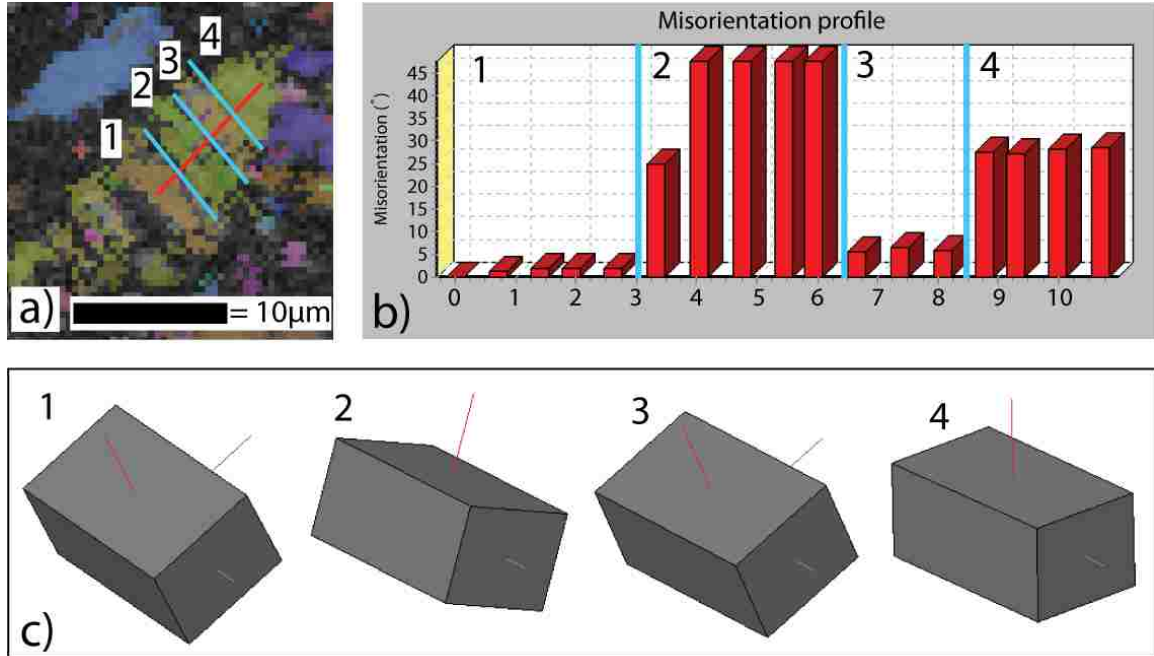


Figure 30. Process used to confirm kink bands in olivine. (a) Expanded view of kinked grain. The red line represents the misorientation transect and the blue lines separate 4 different domains within the kinked grain. (b) Misorientation profile of kinked grain. Notice the sharp boundaries between each crystallographic domain. (c) 3-D crystallographic orientation of domains in kinked grain. Axes are represented by red=100, green=010 and blue=001. Note the crystal is rotating about the 010 axis.

Once each kinked grain was verified the compression direction for each grain was determined. From earlier studies on kink bands in olivine it is known that the shortening direction in a kinked grain will be oriented normal to the rotation axis of the kink band (Lenze et al., 2006). By making pole figures of the kinked grains which display the main crystallographic axes the kink morphology can be determined. Since the [100] and [001] axes are the only Burgers vectors that accommodate dislocation glide in the single crystal, in a kinked grain one of these axes must be the compression direction, (Fig 31). The rotation axes being

uniaxial symmetry of the deformation stress field. It can also be observed that the girdles are not orientated normal to North/South direction of the stereonet. This rotation could be attributed to one or both of the following: 1) the sectioning cut after deformation not being perfectly aligned parallel to applied compressive stress, or 2) the sample geometry after deformation was less than optimal, as seen in (Fig. 21). To correct for this rotation in the data a single point for each kinked grains cluster of [001] poles was chosen, then the mean vector was calculated from this population using the eigenvector function in the program Sterowin, (Fig. 33). The data set of [001] poles was then rotated such that the mean vector plotted at 000° , 00° on the stereonet, allowing for comparison of angular variations in preferred compression to the calcite data set.

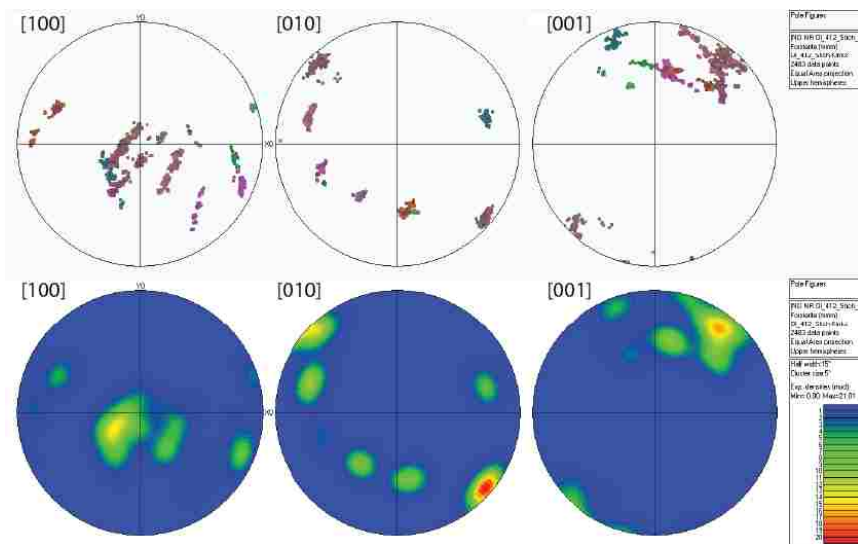


Figure 32. All kinked grains on a pole figure. Upper pole figure shows the raw orientation data of 8 kinked grains from sample OI_412. Lower pole figure is contoured using a halfwidth of 15° and pixel averaging of 5° . Compression for both pole figures is vertical. The [001] axis is at low angle to compression while the [100] and [010] for girdles normal to compression.

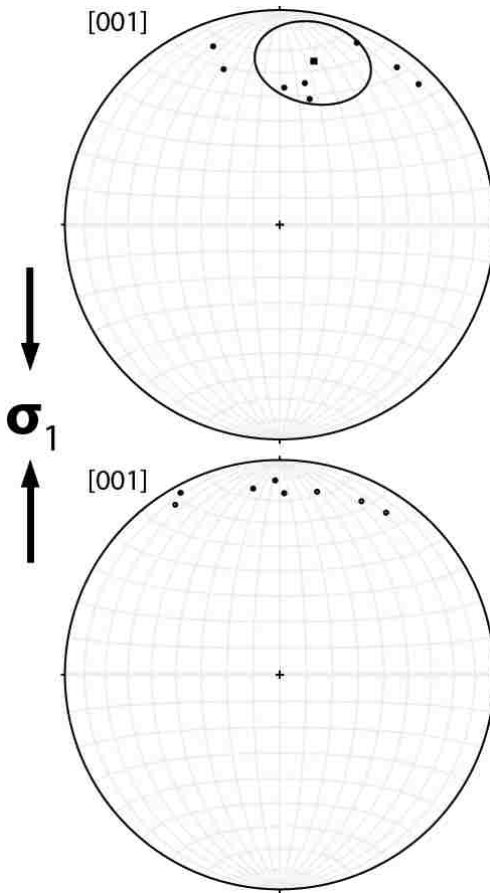


Figure 33. Rotation of calculated compression directions in kinked grains. Upper pole figure shows the [001] axes of the 8 kinked grains identified in OI_412. Square inside upper pole figure represents the mean vector determined by eigenvector analysis. Lower pole figure shows the data set rotated such that the mean vector is orientated at the 0, 0 point on the stereonet.

Calcite EBSD analysis

Two EBSD OIMs were produced from each deformed calcite sample, covering a total area of approximately 7mm^2 for each sample. Photomicrographs of the sectioned and polished samples can be seen in (Fig. 34). One EBSD Euler orientation map for each sample is shown in (Figs 35 and 36).

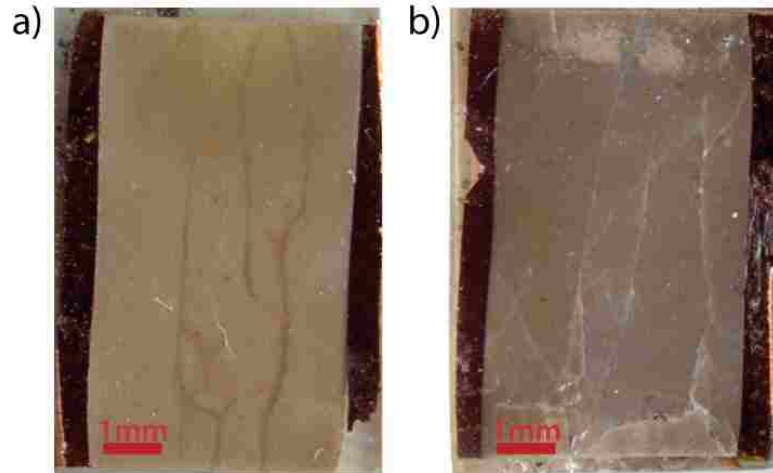


Figure 34. (a) Photomicrograph of sample Sfn_002. Left and right extremities of the photo shows the polished Cu jacket used to confine the sample. Compression is vertical. (b) Photomicrograph of sample Sfn_004. Left and right extremities of the photo shows the polished Cu jacket used to confine the sample. Compression is vertical.

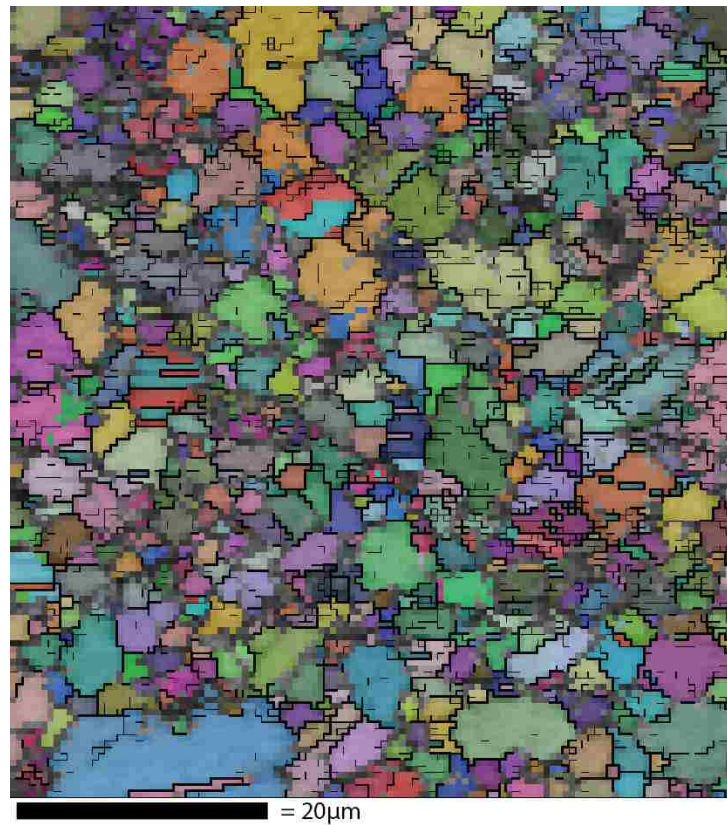


Figure 35. EBSD OIM of Sfn_002 after noise reduction. Compression is vertical

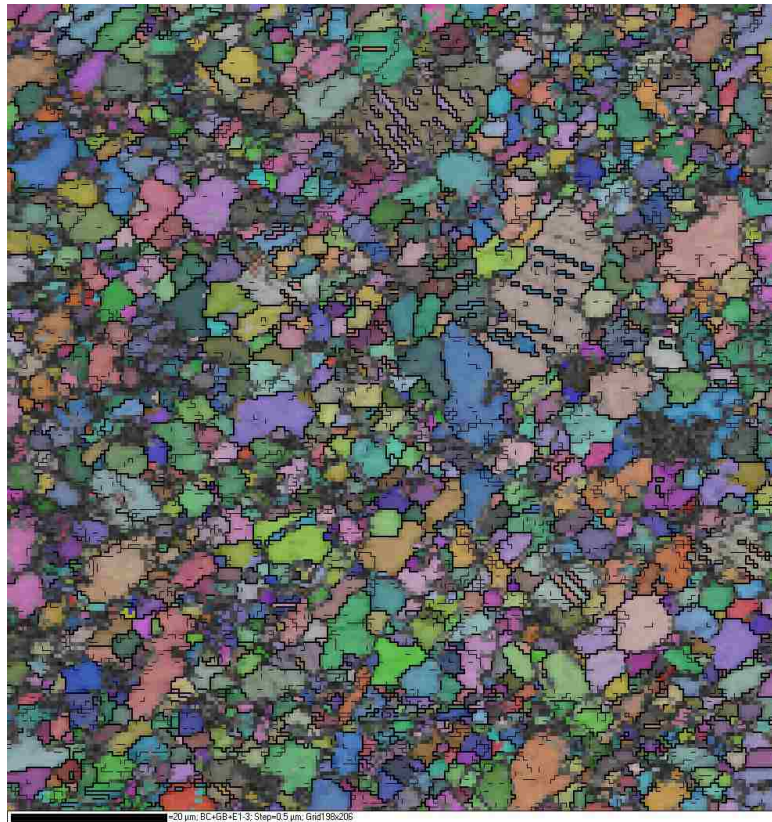


Figure 36. EBSD OIM of Sfn_004 after noise reduction. Compression is vertical.

Calcite local stress direction deviations

Mechanical twins in the calcite samples were used to determine modulations in the direction of maximum compression. Mechanical twins in calcite are visually similar to kink bands in olivine when viewing an OIM. Twins form discrete domains separated by high-angle boundaries. Examples of twins in the Sfn_002 Euler map can be seen in (Fig. 37). E-twins form with a misorientation of the c-axis between the host and the twin of 52° about $\langle 20\text{-}21 \rangle$, therefore after visually identifying twins they are easily verified using misorientation transects and pole figures, see (Fig. 38). Valcke et al. (2006) and Tielke (2010) has shown that when using misorientation transects, e-twins show

diagnostic misorientation values of $\sim 78^\circ$ (Valcke et al., 2006; Tielke, 2010).

Using misorientation transects on OIMs and pole figures to confirm the 52° c-axis separation, a total of 60 twinned grains were identified, 30 from each deformed sample of Solnhofen (Fig. 38). To ensure deformation twins were not formed during the pressurization and heating stages of each experiment, a third sample of Solnhofen was placed in the Griggs apparatus and brought up to 2.5 kb and 300°C and then quenched without deformation. This sample was prepared using the same method as the deformed samples and analyzed using EBSD. The OIM shows no visible twins which is also confirmed using misorientation transects, (Fig. 39).



Figure 37. EBSD OIM of Sfn_002 showing twinned grains. Euler orientation map from sample sfn_002 (same as Figure 35) with a few representative twinned grains outlined in red boxes. Compression is vertical.

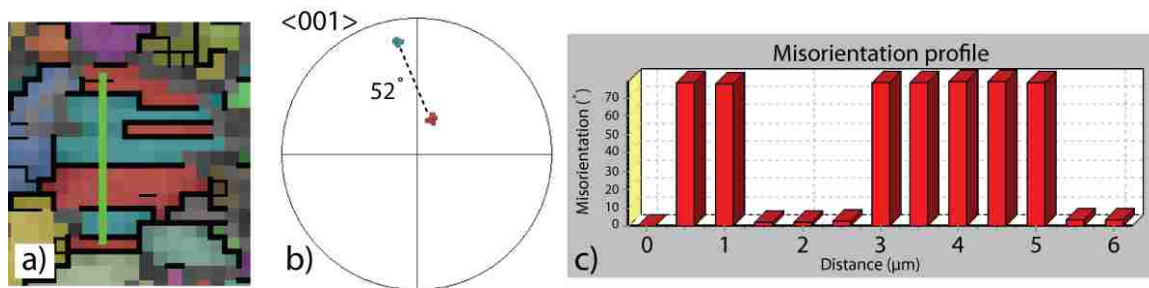


Figure 38. Confirmation of twinned grains. (a) Expanded view of twinned grain in Sfn_002. The green line represents the location of the misorientation transect. (b) Pole figure showing c-axis of host and twinned grain. Note the c-axes of the twin and host are 52° apart. (c) Misorientation profile from twinned grain. Each domain is separated by a sharp boundary of $\approx 78^\circ$, which is diagnostic of calcite twins in EBSD OIMs (Valcke et al., 2006).

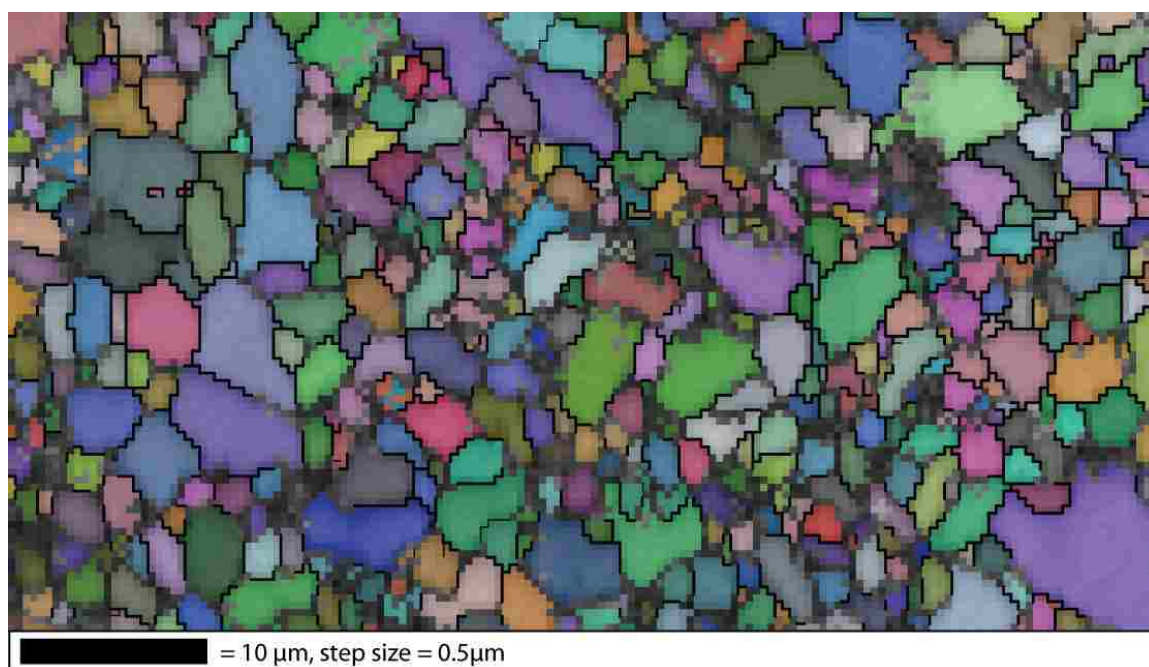


Figure 39. EBSD OIM of Sfn_001 with no twins. This sample was brought up to 2.5kb and 300°C to ensure that the heating and pressurization procedure does not produce any mechanical twins. No twins are visible within the OIM.

Once the calcite twins were verified, the compression direction for each grain was determined. First the c-axes of the twin and host domains were plotted on a stereonet, then using the method of Tielke (2010) the Euler angles for each

domain were converted to trend and plunge of the c-axes and plotted using the program Sterowin, (Fig. 40). Using the eigenvector analysis built into Sterowin, the mean vector of the two c-axes vectors is calculated and plotted on a best-fit great circle from the two c-axes. From studies on deformation twins in calcite (e.g. Burkhard, 1992 and Jamison and Spang, 1976) it is known that two c-axes are coplanar and are each orientated 26° away from the bisecting e-plane pole; thus the mean vector which was calculated in the eigenvector analysis is representative of the e-plane pole of the twinned grain, (Fig. 40). The preferred compression and tension directions are located 45° away from the e-plane pole along the calculated best-fit great circle, (Fig. 40). A program provided by Jacob Tielke was used to determine the associated compression and tension vectors, from measurements of the two c-axes, and the calculations of the e-plane pole and orientation of the best-fit great circle (Tielke, 2010). After the compression directions were determined for all 60 individual twins, they were combined on a single stereonet to examine their spatial distribution in comparison to the applied macroscopic compression direction, (Fig. 41).

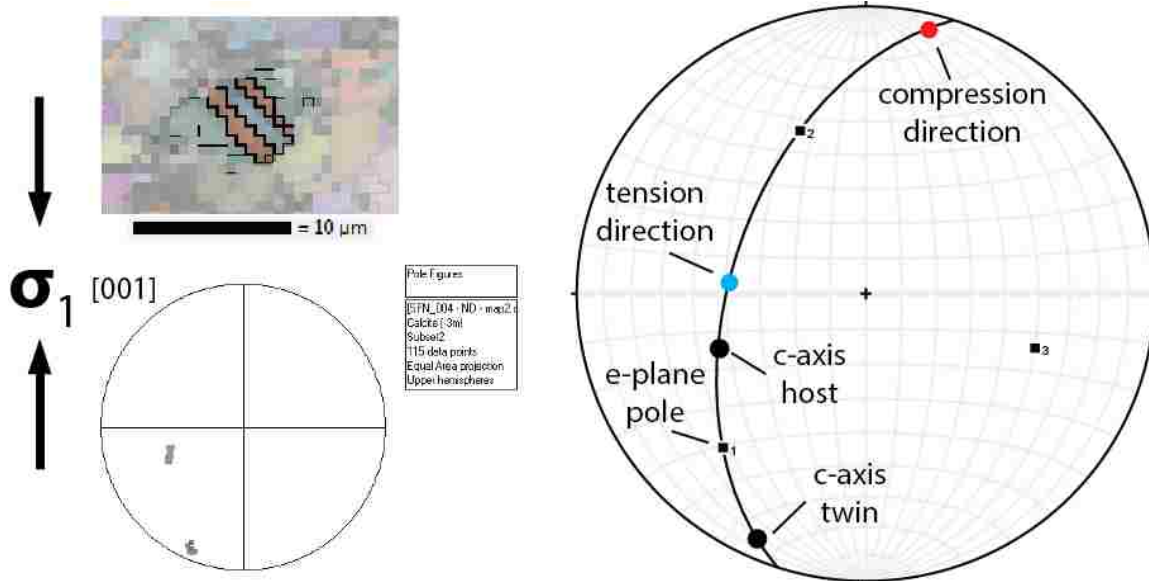


Figure 40. Calculation of preferred compression direction. Upper left shows a twinned grain from an Euler orientation map. Bottom left shows the associated pole figure of the [001] for the shown twinned grain. Stereonet on right shows the determination of compression direction from the orientation of the two c-axis and e-plane pole. Numbered boxes indicate the eigenvectors, 1 being equivalent to the e-plane pole.

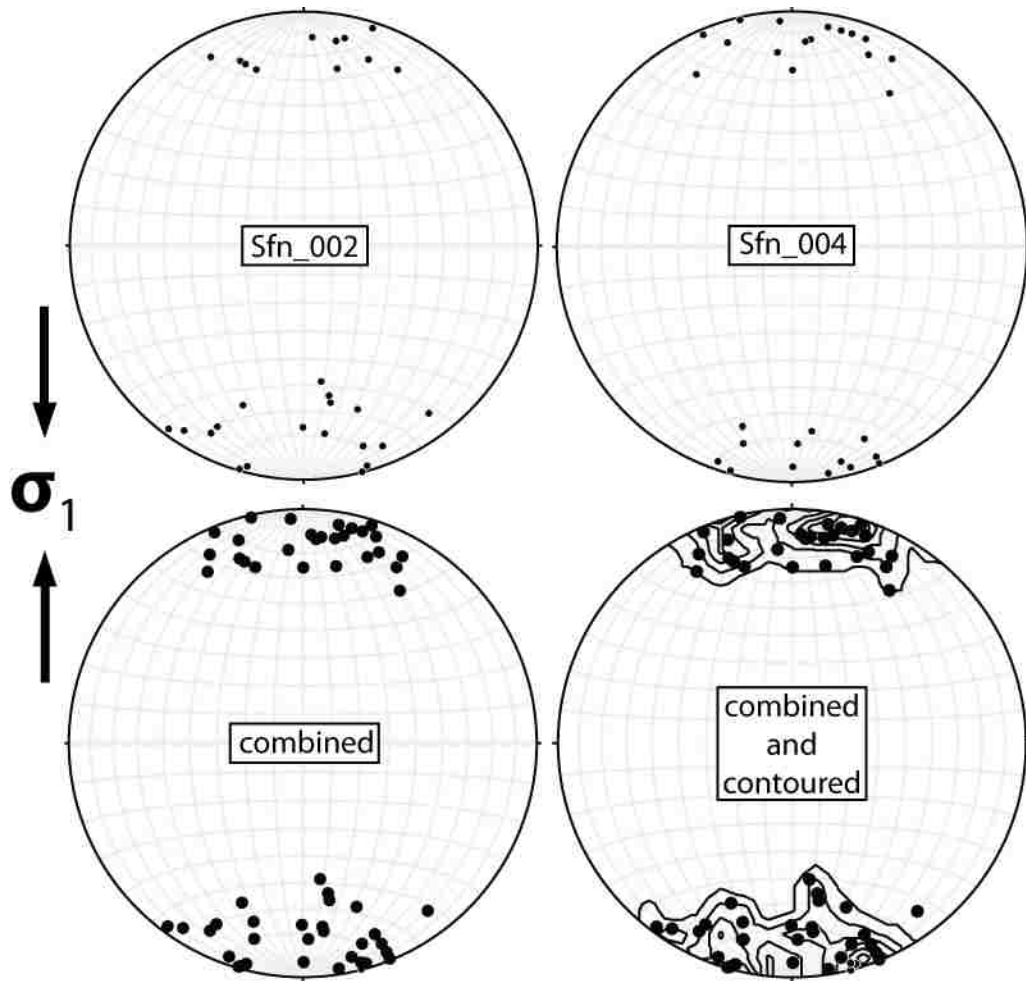


Figure 41. Compression directions from both calcite experiments. Upper stereonet shows the 30 calculated compression directions from twins in each deformed calcite sample. Bottom stereonets show the combination of all calculated compression directions from all twinned grains from both samples of Solnhofen. Bottom right, contoured stereonet of all data points to 1% area. All stereonets are upper hemisphere projections.

Finite element model local stress deviations

One finite element model was produced for each material, calcite, quartz and olivine. Within each model, 14 different grain populations were used which had different elastic constants and yield stresses and were run with different values of constant stress (Table 5). After completion of all constant stress FEM

runs, the stress tensor was extracted from each node (288 nodes/grain, or 741,312 nodes total) according to which of the 14 subpopulations the node is included in, (Fig. 42). This tensor is in the model coordinate system where x ,y and z are represented by σ_{11} , σ_{22} and σ_{33} respectively; since compression is vertical, σ_{22} is the stress component of interest. In addition, the diagonalized stress tensor was extracted from which the maximum compressive stress was used. Once the two stress components were extracted (Equation 4) was used to convert the stress magnitudes of both tensor components into the angular variation of the local stress tensors at each node in relation to the macroscopic applied to the model.

$$\theta = \cos^{-1} \left(\frac{\sigma_{22} \text{ component}}{\varphi} \right) \quad \text{eq. 4}$$

Where θ is angular variation between the macroscopic stress being applied to the model and the local diagonalized stress tensor (φ), a pictorial description of the conversion to angle is seen in (Fig. 43).

Table 5
Run conditions for each finite element model

material	yield stress_{min} (MPa)	yield stress_{max} (MPa)	σ (MPa)	plastic ϵ (%)	total ϵ (%)
Calcite	10	14	15.0	0.0001193	0.005811267
Quartz	60	230	60.0	0.0001019	0.015825802
Olivine	82	136	150	0.0006521	0.09513313

*values of stress are final values at which model successfully ran

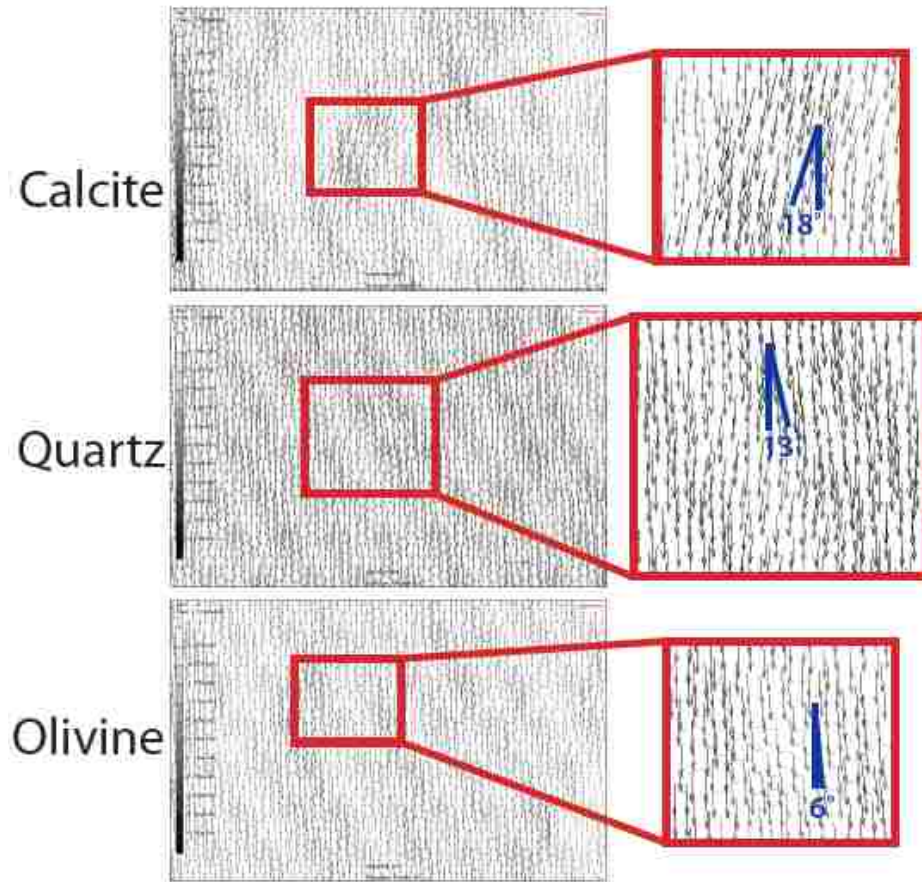


Figure 42. Example subsets of FEMs. Small example subsets (approximately 8% of whole model) of FEMs from different FEM runs. (Left) shows arrows which indicate the direction and magnitude of the diagonalized stress tensor in approximately 90 grains. (Right) expanded view of the subset, blue lines show the angular relationship between the diagonalized stress tensor and the σ_{22} direction.

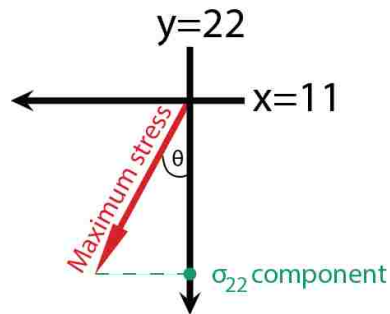


Figure 43. Pictorial description of stress variation calculation in FEMs. θ represents the angle between the σ_{22} component of the stress tensor for each node, and maximum stress represents the principal component of the diagonalized stress tensor.

To calculate the bulk aggregate stress direction modulations, the values of mean angular variation, median angular deviation, standard deviation of the angular deviation and maximum angular deviation of the 14 subpopulations are averaged which can then be compared to stress directions modulation values obtained from the experimental results, see (Fig. 44) for summary.

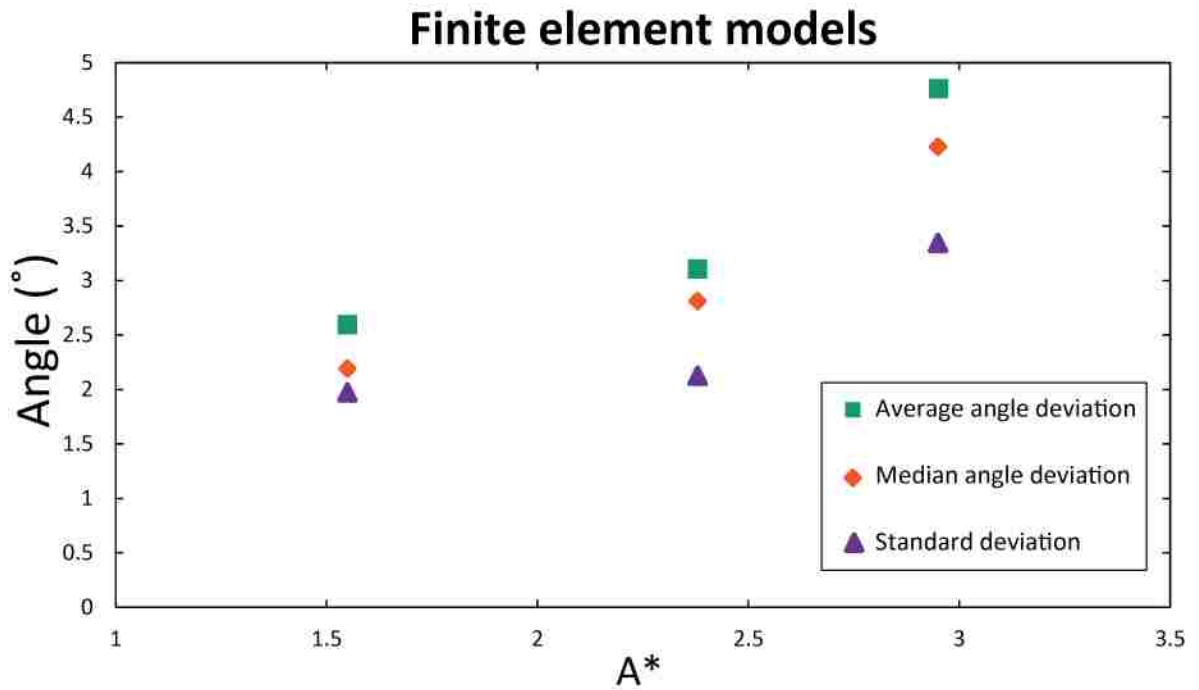


Figure 44. Summary graph of all FEM angular variations. Plotted are the average, median and standard deviation of stress direction deviations away from the macroscopic applied stress as a function of single crystal elastic anisotropy.

CHAPTER 5

DISCUSSION

Misorientation distribution

This section will examine the results of the Schmid factor and mean misorientation analysis. From the histograms in (Figs. 27 and 28) it can be observed that within the olivine samples increasing strain does not alter the distribution of intragranular strain amongst grains of different Schmid factors. The maximum mean misorientation angle through all Schmid factors of each plot occurs at approximately 1.5° . The only significant difference arises from the larger distribution of misorientation angles observed in the higher strain experiment, which is to be expected. I postulate that this trend of an increased broadening of the distribution of intragranular misorientations would continue up to the onset of dynamic recrystallization. At this point, if deformation is still occurring in a dislocation glide regime, new grain growth will be controlled either by subgrain rotation or grain boundary migration (Bysticky et al., 2000; Zhang et al., 2000). In either case, each controlling mechanism initiates the development of a distinct lattice preferred orientation (LPO) in the aggregate. The two different deformation mechanisms produce different patterns of LPO, being dominated by strain or the stress, but in either case the production of a LPO will produce a larger population of grains with similar orientations that are well orientated for dislocation glide (Karato, 1987; Zhang and Karato, 1995). Thus the population of recrystallized grains would have higher Schmid factors and the overall occurrence of high Schmid factor grains will increase. Since numerous studies

(e.g. Gennerat et al., 2012 and Castenlau et al., 2010), including this one, have shown that intragranular deformation is not effected by Schmid factor, it seems that even with an increase in the number of grains with higher Schmid factors from recrystallization, there would be no effect on the observed pattern of mean misorientation values seen in (Figs. 27 and 28). These findings indicate that for any amount of strain, Schmid factor is not a controlling factor in stress distributions during deformation of aggregates.

Experimental local stress direction modulations

Constraints on calculated compression directions

This section will analyze the difference in calculated compression directions from olivine and calcite, and the associated error involved. When preferred compression directions are calculated from both types of microstructures it must be noted that these are not the only compression directions that can produce the microstructure. The deformation mechanisms used in this study have a critical resolved shear stress and direction just as a slip system operating in dislocation glide. Also, just as in glide, the angular relationship between slip plane and direction defines the Schmid factor for the deformation mechanism. By calculating the preferred compression directions using crystallographic orientation data we can only define the local compression direction for that orientation which produces a Schmid factor of 0.5 for the specific deformation mechanism. By consequence, for any given stress applied to polycrystalline material, each grain will have multiple vectors which radiate out from the calculated preferred compression direction which could also produce the

specific deformation microstructure, thus inducing error into the calculations of local compression directions.

This effect of non-unique preferred compression directions is illustrated for calcite in (Fig. 45), which shows the resolved shear stress coefficient of each e-twin system in calcite (Jamison and Spang, 1976). This figure shows that the trigonal symmetry of calcite allows multiple compression vectors to have the same amount of shear stress resolved onto multiple twin systems simultaneously. Also, this figure shows the error included when using individual twinned calcite grains for local stress direction determination. Any compression direction within the 0.36 contour will produce a calculated preferred compression direction at the location of the 0.5 point as mentioned above, causing an error of approximately 20° for each twinned grain.

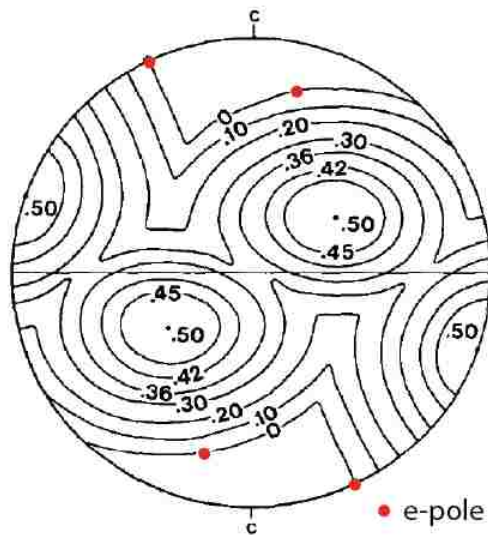


Figure 45. Resolved shear stress for calcite twins. The c-axis is oriented vertical and the red dots are indicative of the three e-poles for the three twin systems which are depicted, modified from Jamison and Spang (1976).

Similarly to calcite there is an error in compression directions which were calculated from kink bands in olivine, but the error is more constrained than in the case of mechanical twins. The slip systems that operate in olivine were shown in (Fig. 6b), and kink bands form due to the inability for stress to be resolved on any of slip planes when compression is parallel to the principal crystallographic axes. If the maximum compressive stress begins to deviate away from the direction of the principal crystallographic axes, the stress will then be resolved upon a glide plane. To the author's knowledge there is no study which has investigated the CRSS of the kinking system in olivine, but due to the relative infrequency of kinked grains in deformed samples, the CRSS of kinking can be assumed to be relatively high when compared to dislocation glide systems. This arrangement of slip planes helps to minimize the inherent error in calculated compression directions by limiting the allowable compression directions on a grain that has produced a kink band.

Calculated local stress variations

Since the CRSS of each deformation mechanism is specific to the each material tested in this study, and the stress during constant strain rate experiments is also specific to the material, the range of allowed compression orientations for the mechanism to initiate is also material specific. This allows for the direct comparison of local angular variations in different materials using deformation microstructures. Comparison of calculated local compression directions from calcite and olivine can be seen in (Fig. 46).

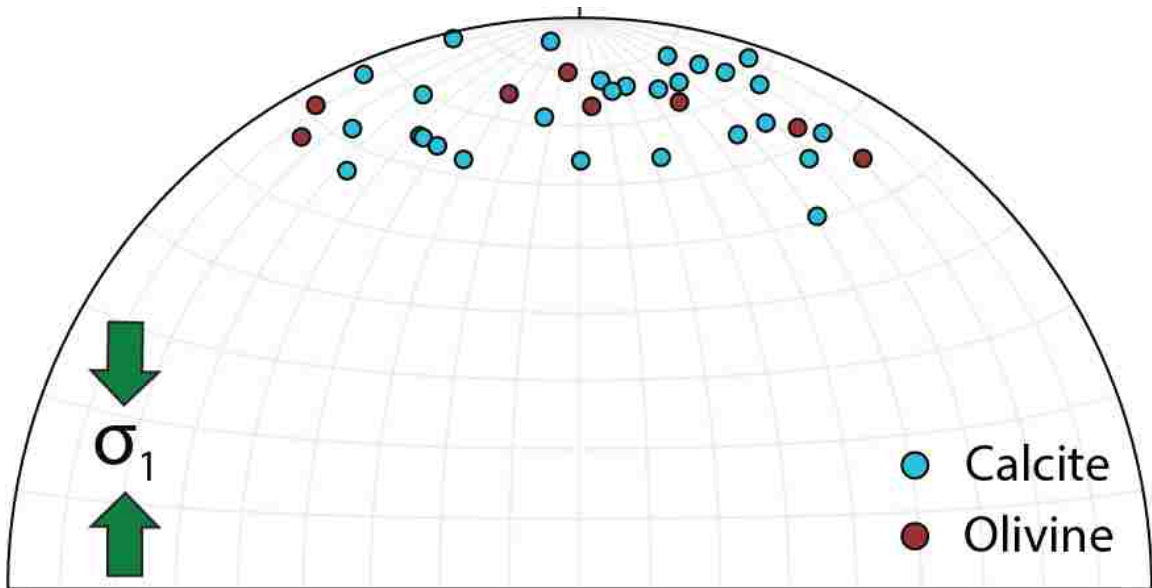


Figure 46. Stereonet comparing olivine and calcite data. Olivine grains (red) and 30 twinned calcite grains (blue) plotted with respect to the macroscopic stress applied during deformation of each aggregate. Olivine data has been rotated in a way which places the mean vector for all kinked grains at point 000° , 00° on the stereonet for an easier comparison. Mean angular variation for all measured compression directions in both materials is 23° . The 30 twinned grains are a combination from both experimental runs, all 60 are not shown to increase the clarity of the graph.

In (Fig. 46) there is no large difference between the two materials, with the maximum angle for calcite being 40° and 35° for olivine. This result argues against the working hypothesis that the single crystal anisotropy will determine the amount of stress heterogeneity, but two factors must also be considered. First, The CRSS for the formation of kink bands in olivine is much larger than that which is required to produce twins in calcite. The strain of the olivine experiment which produced kinked grains was $\approx 35\%$ compared to the average of 15% for the calcite experiments. From studies utilizing in-situ X-ray diffraction (e.g. Long et al., 2011) it can be inferred that as soon as plastic deformation initiates during polycrystalline deformation, the stress field will begin to evolve into a more

complex state, which could be expected to continue with increased strain. Since the final strain was much larger in the olivine experiment one could also conclude that the stress field was much more convoluted in the olivine at the time the kinked grains formed than the calcite experiment. Second, when these materials are described by single crystal anisotropy only the elastic anisotropy is taken into account. This disregards the open vs closed yield surface in olivine and calcite respectively, also the symmetry of calcite. Elastically, olivine is more isotropic than calcite, but the trigonal symmetry of the low CRSS twinning system in calcite means that it is much more plastically isotropic than olivine. The effects of elastic vs. plastic anisotropy are inseparable in deformation experiments, therefore this necessitates the construction of a parameter which includes both elastic and plastic anisotropy before both materials can be quantitatively compared.

Comparison to previous studies

The stress direction results from the calcite twin analysis appear to be in agreement with previous studies using the dynamic analysis technique. To the authors knowledge no study exists which exclusively examines the distribution of calculated compression directions within deformed aggregate of calcite as a function of single crystal properties, but as previously mentioned, many studies have used different techniques to determine macroscopic stress at the outcrop scale from deformation twins. (Fig. 47) is an example of dynamic stress analysis conducted on a deformed limestone from Rowe and Rutter (1990). In the current study the macroscopic stress direction was known and local variations were

calculated; in the Rowe and Rutter study, the local variations were calculated to determine the macroscopic stress direction. When the distributions of calculated stress directions are compared, the results appear to be in good agreement with an average variation from the macroscopic stress direction of approximately 35-40°.

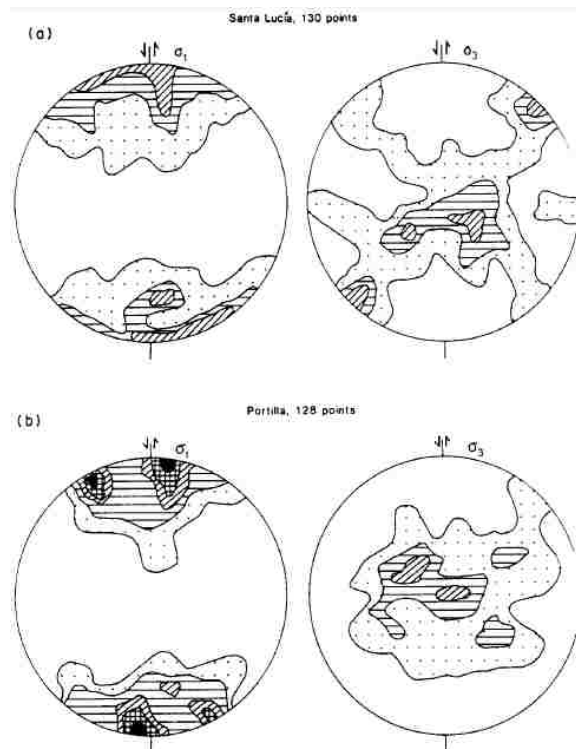


Figure 47. Pole figure of compression data from deformed limestone. Data uses mechanical twins in limestones from the Cantabrian zone of northern Spain to calculate macroscopic stress direction, from Rowe and Rutter (1990).

Local stress direction calculations from olivine in this study show similar results to the finding of Burnley et al. (2013), which investigated the morphology of kink bands formed in deformed magnesium germanate olivine (Mg_2GeO_4). In the Burnley study, 20 kinked germanate grain were analyzed in a similar way to

this study, and preferred compression directions in each kinked grain were determined to be parallel to the [001] axis. (Fig. 48) shows a pole figure of 20 kinked germanate grains, and the distribution of [001] are mainly oriented within 35° of macroscopic compression, and show a similar spatial distribution of compression vectors to what is seen in the San Carlos olivine kink bands analyzed in this study, as seen in (Fig. 46).

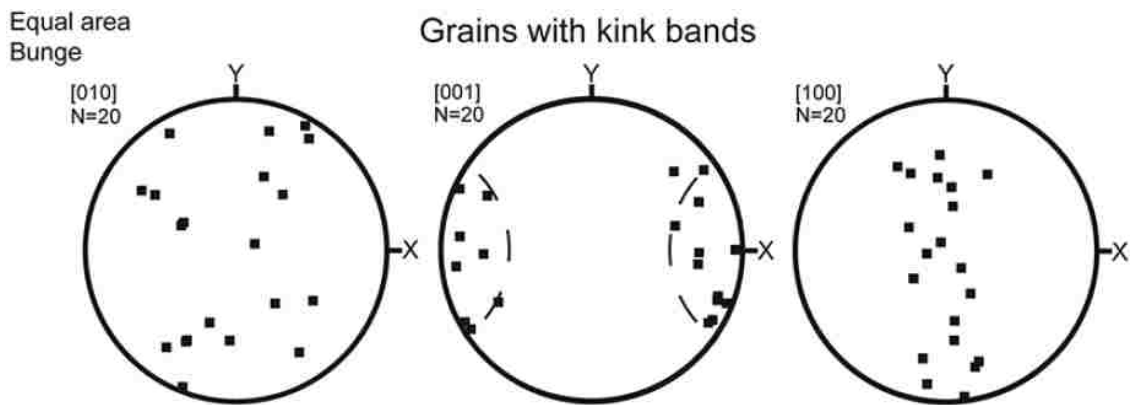


Figure 48. Pole figure of 20 kinked Mg_2GeO_4 grains. The morphology of the kink band is the same as in the current study, with the [001] axis indicating the maximum compression directions in each kinked grain. Dashed line is indicative of the 35° great circle. Compression is horizontal, from Burnley et al. (2013).

Modeled results compared to experimental

The finite element models in this study replicate the general trend which was observed in Burnley (2013). The Burnley (2013) study showed by increasing the anisotropy of constituent structural components within the simple hexagon model, the heterogeneity of the stress field will also increase as a function of the anisotropy (Fig. 44). The main difference between these two studies is the lower observed magnitude of stress direction variations in this study (Fig. 49). The original FEMs of Burnley (2013) were constructed with a wide range of elastic

anisotropy, some of which are exaggerated beyond values which could be expected from a monophasic polycrystalline aggregate. By plotting the results from the FEMs of this study along with the data from Burnley (2013), a trend can be observed that is in agreement with the original hypothesis that angular variation in local compression directions are controlled by the anisotropy of the single crystal.

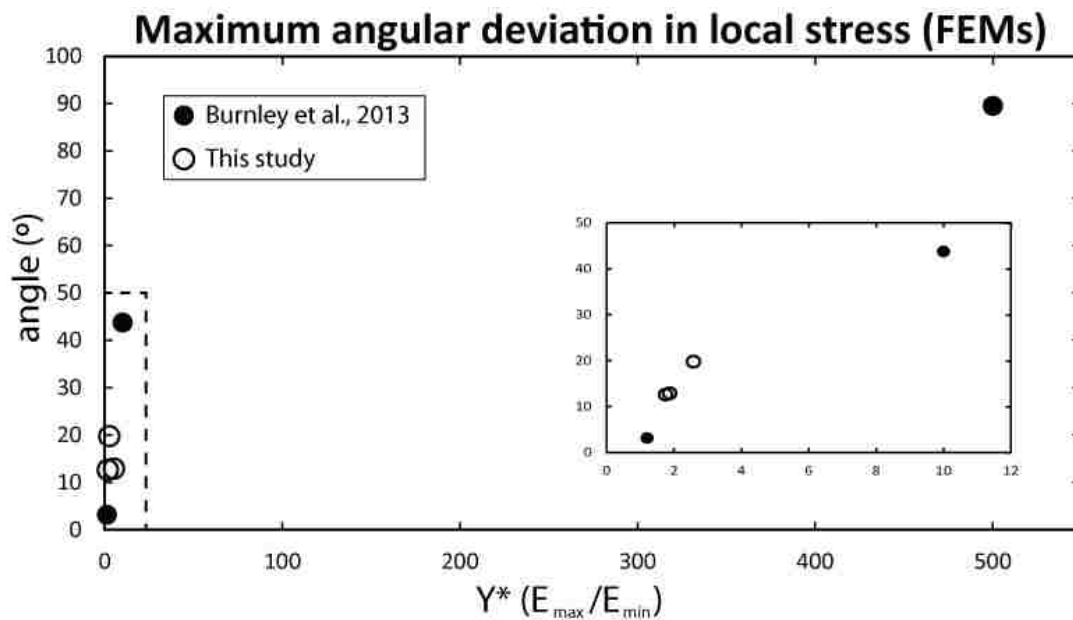


Fig. 49. Comparison of FEMs to those of Burnley, (2013). Graph shows maximum angular deviations in local stress tensor as a function of Y* from Burnley et al. (2013) (solid circles) and this study (open circles). Inset is representative of area within dashed box.

There is an observed agreement in the maximum stress direction variations between both the experimentally deformed samples and the FEM results in this study. The trend of increasing angular variation with increasing constituent single crystal anisotropy is also in support of the original hypothesis, as seen in (Fig. 50). However, when all results are plotted together a significant

discrepancy is observed between the two techniques. The modeled maximum stress variations consistently plot $\approx 20^\circ$ lower than the experimental results (Fig. 50). There are two aspects of the finite element models that can explain this discrepancy. First, the models are constructed with all hexagons welded together at each interface. This is done to ensure the model maintains compatibility during deformation but works focusing on deformation mechanisms during polycrystalline deformation point to the importance of grain boundary sliding as a deformation mechanism (Raj and Ashby, 1971; Jackson et al., 2006; Hansen et al., 2011). The addition of a grain boundary sliding component into the FEMs would complicate the stress field and in turn increase the angular variation observed in each model; but since the mechanics of grain boundaries are not fully understood it is impossible to accurately integrate this deformation mechanism into the models. Second, the amount of accumulated strain in the FEMs is $<1\%$, in comparison to the 15% average in the Solnhofen experiments and 35% in the olivine experiment. These values of strain are necessary for each of the experimental method respectively; the FEMs are designed to be used for small strains, and are neither numerically stable nor particularly reliable at higher values of strain. In addition, to form the microstructures in the experimentally deformed samples required moderate strains, in the case of calcite twins, and large strains in the case of kink bands in olivine. As mentioned above, continued plastic deformation can be expected to further complicate the stress field, and therefore the measured values of stress modulations. This leads to the conclusion that the observed discrepancy in maximum stress direction deviation

between the experimental and modeled deformation can also be influenced not only by the rheology of grain boundaries, but also by the total strain of each experiment. Thus, grain boundaries, single crystal elasticity, single crystal plastic and strain must be considered within any attempt to predict stress heterogeneity during polycrystalline deformation.

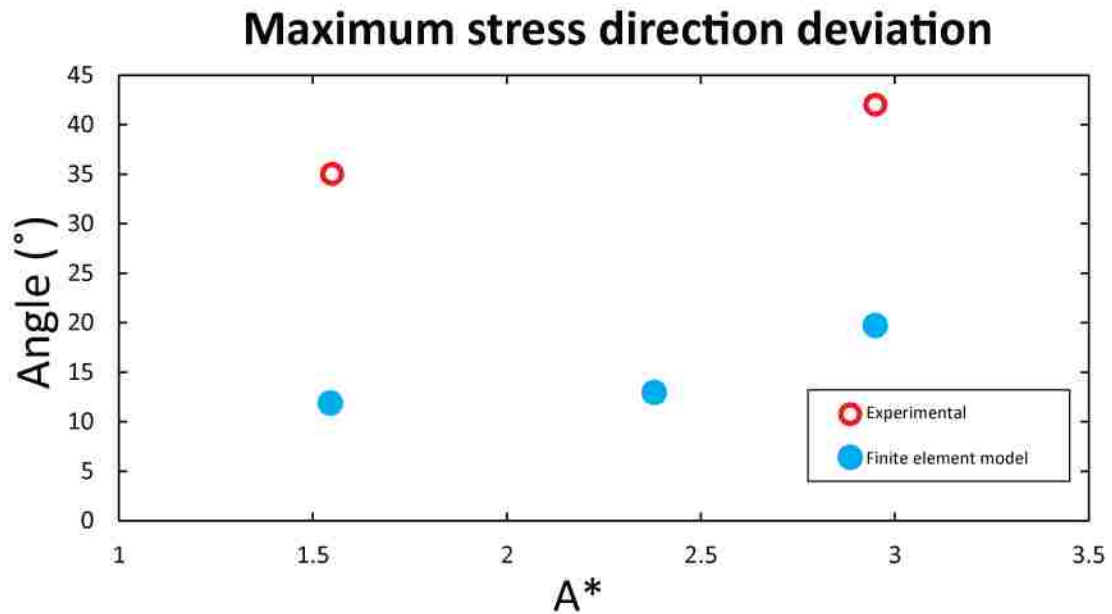


Figure 50. Comparison of all modeled and experimental results. Plot shows the maximum angular deviation observed in each experimentally (red) and modeled deformation (blue), as a function of the single crystal elastic anisotropy. A small positive correlation is observed between increasing single crystal elastic anisotropy and the maximum variation in local stress direction.

CHAPTER 6

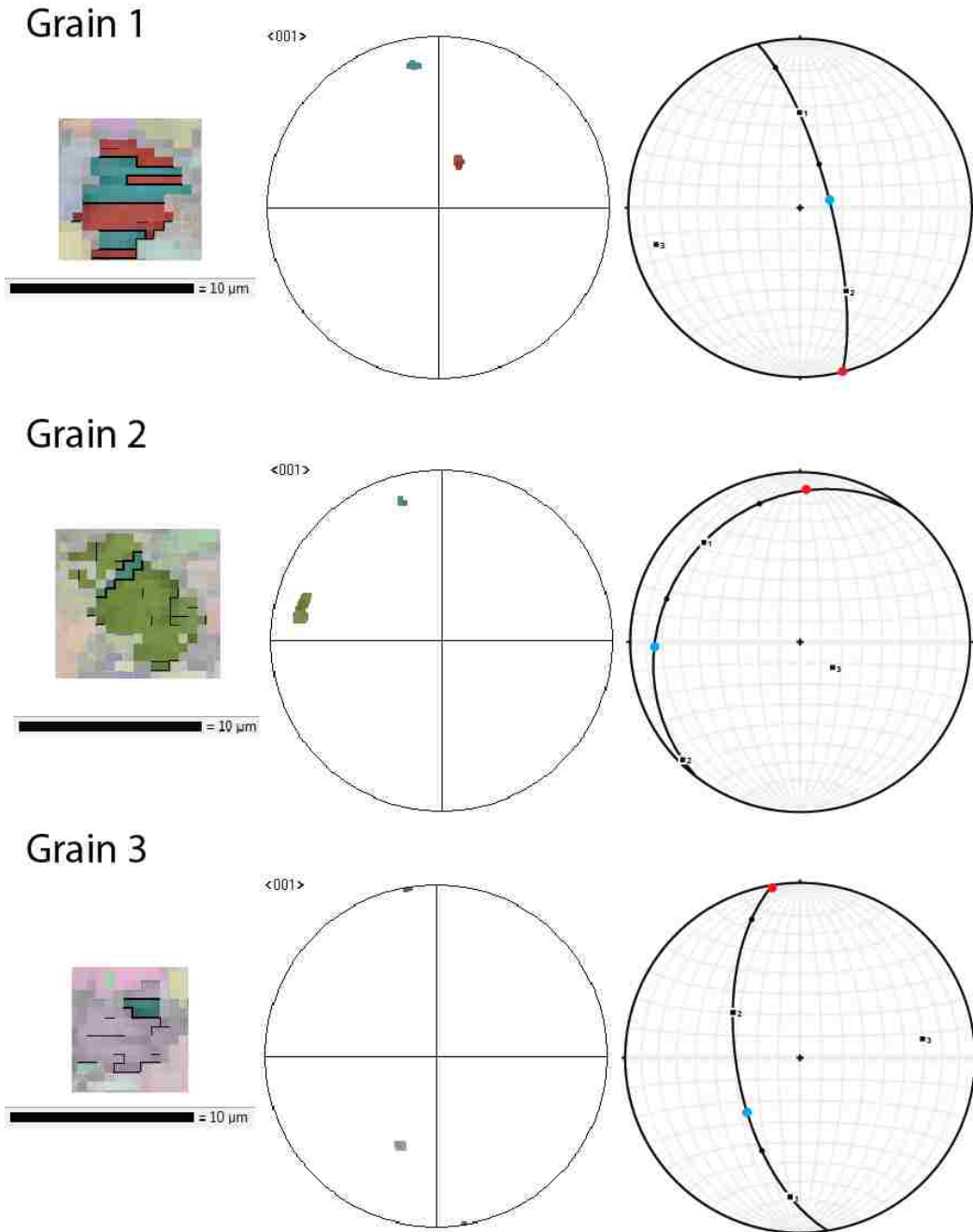
CONCLUSIONS

To summarize, the hypothesis that stress and strain heterogeneity is induced during polycrystalline deformation by the elastic and plastic anisotropy of the single crystal has not been disproven. In the comparison of experimentally deformed olivine and calcite, the microstructures show a general trend of increasing stress heterogeneity with larger values of single crystal elastic anisotropy. In addition, the results of this study have elucidated two deficiencies in the experimental method that would need to be resolved before any further work is undertaken on the matter. The first being the ability to include plastic anisotropy into the calculation of single crystal anisotropy for each material, differences between an open and closed yield surface in a single crystal constituent will have large effects on stress partitioning during polycrystalline deformation. The second deficiency was identified using the local stress direction modulation data from the finite element models. These data show a necessity to integrate a structural component into the FEMs which can accurately replicate the rheology of grain boundaries. The FEMs used in this study were constructed without the ability to activate grain boundary sliding as a deformation mechanism, and as a result lack the magnitude of maximum variation which is observed in experimental data. The addition of a grain boundary sliding component to the models will be difficult, the current state of understanding about grain boundary mechanics is still very incomplete and many difficulties exist in adding this as a structural component to models of polycrystalline deformation. In addition to

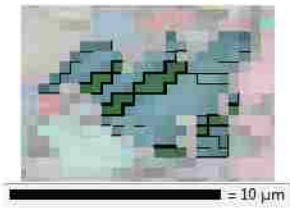
these experimental deficiencies it appears that total accumulated strain must also be considered when making any prediction of stress and strain heterogeneity in a deformed polycrystal. The effect of strain is believed to have been partly responsible for the difference in maximum local stress deviations between the two experimentally deformed samples, and also contribute to the discrepancy between the magnitude of stress direction modulations calculated from both the experimental and modeled results.

Appendix A: Calcite host/twin c-axis analysis

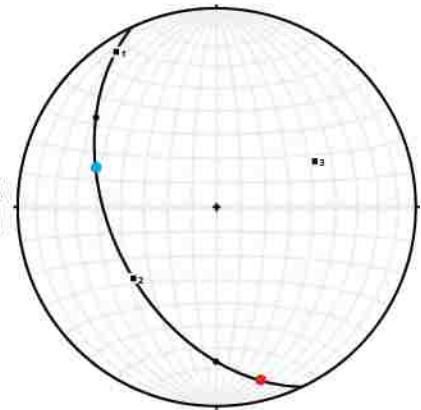
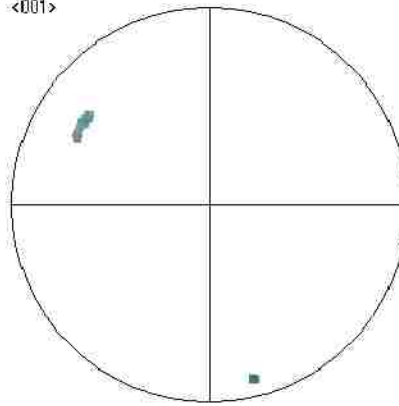
(Left) Each twinned grain image is cropped from the appropriate EBSD map. (Center) Pole figure shows the [001] axes of the host and twinned portion of each grain. (Right) Stereonet produced through the program Stereowin, numbered points are the results of the eigenvector analysis of the two c-axes with #1 being the pole to the e-plane. The red dot represents the compression direction and the blue represent the tension direction.



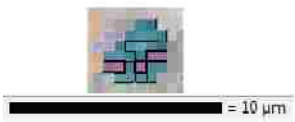
Grain 4



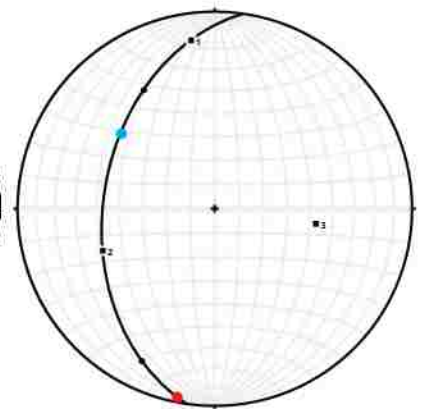
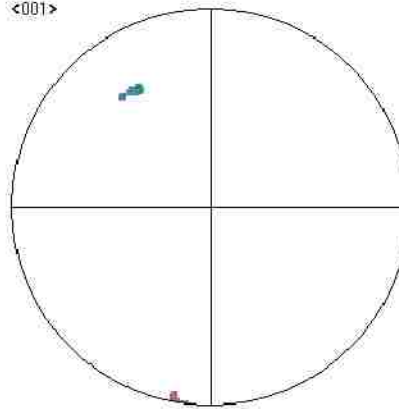
<001>



Grain 5



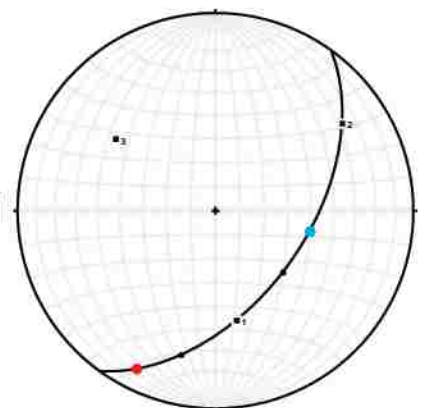
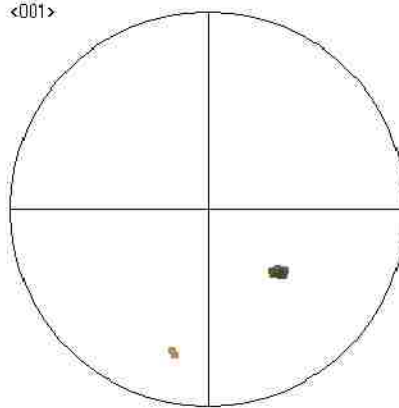
<001>



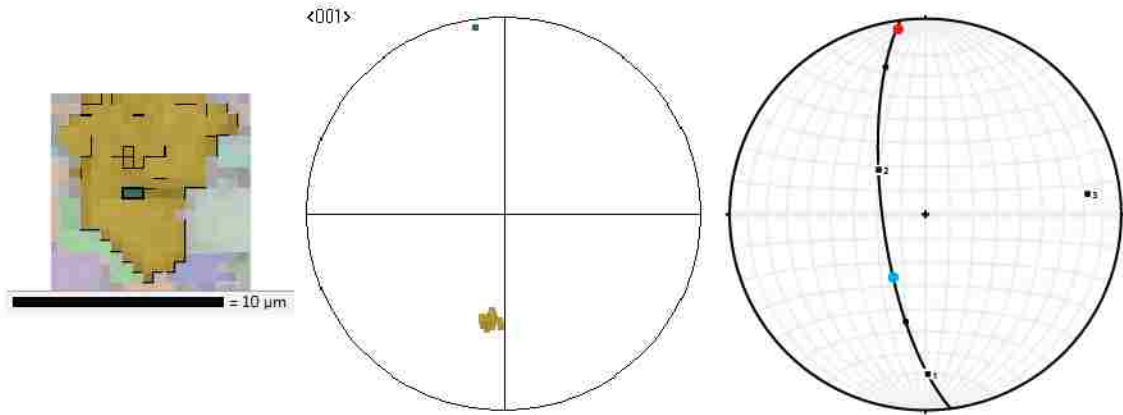
Grain 6



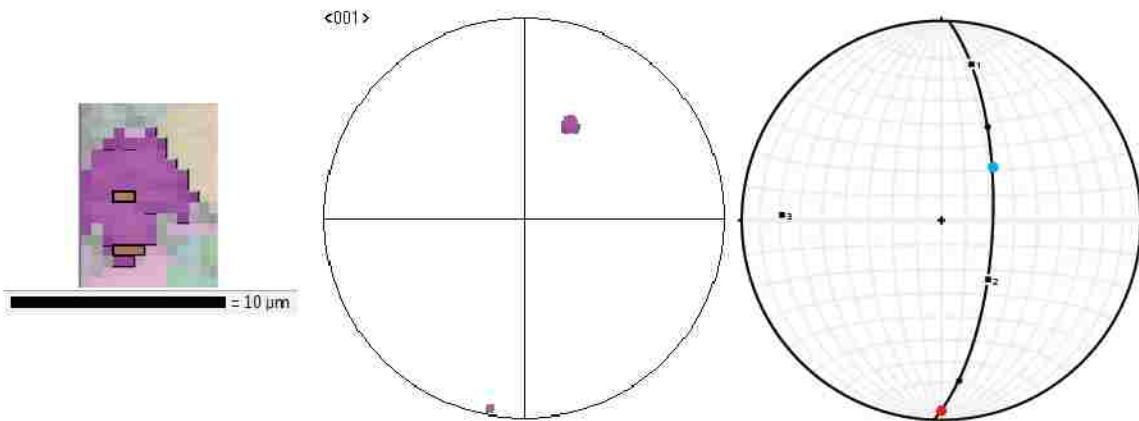
<001>



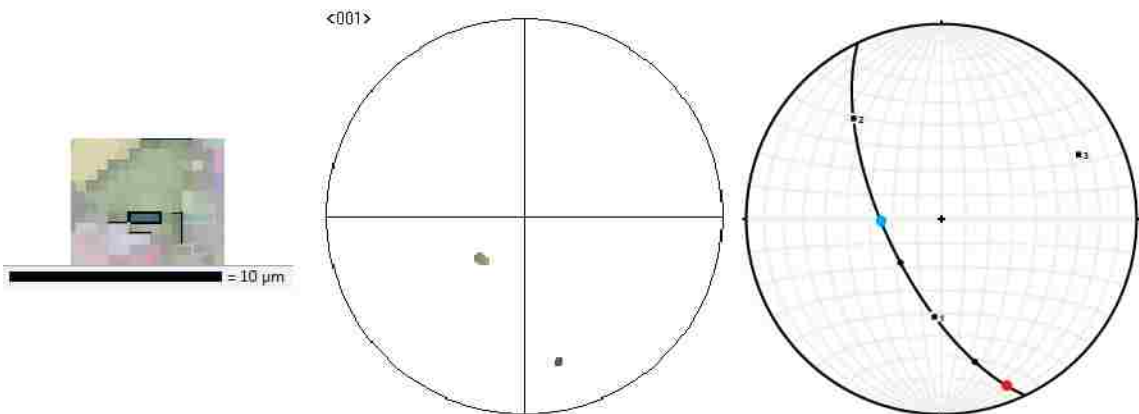
Grain 7



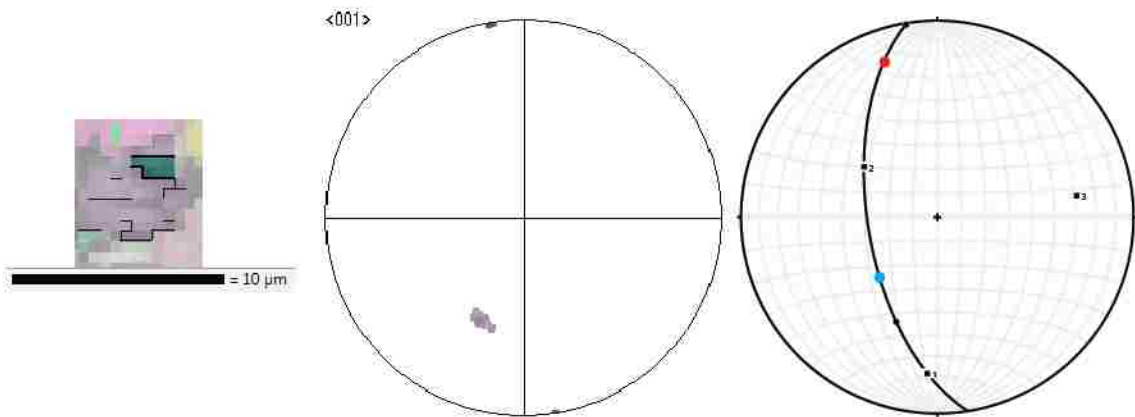
Grain 8



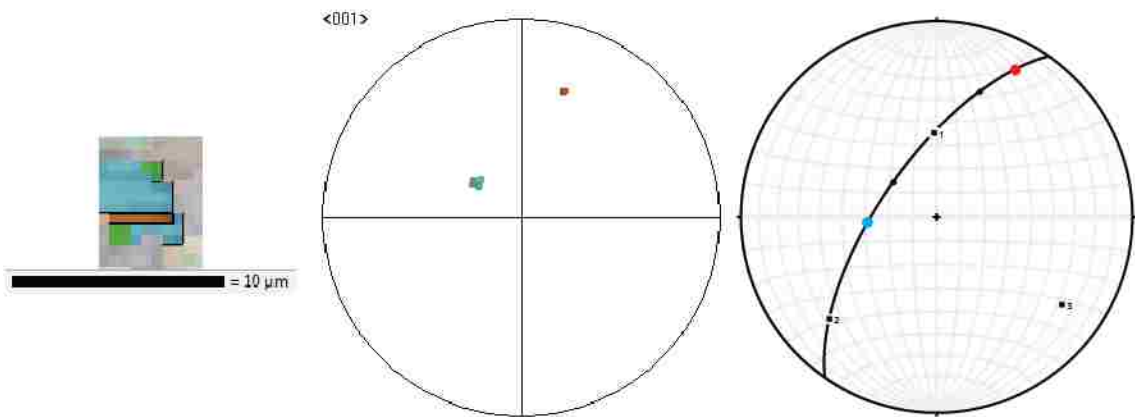
Grain 9



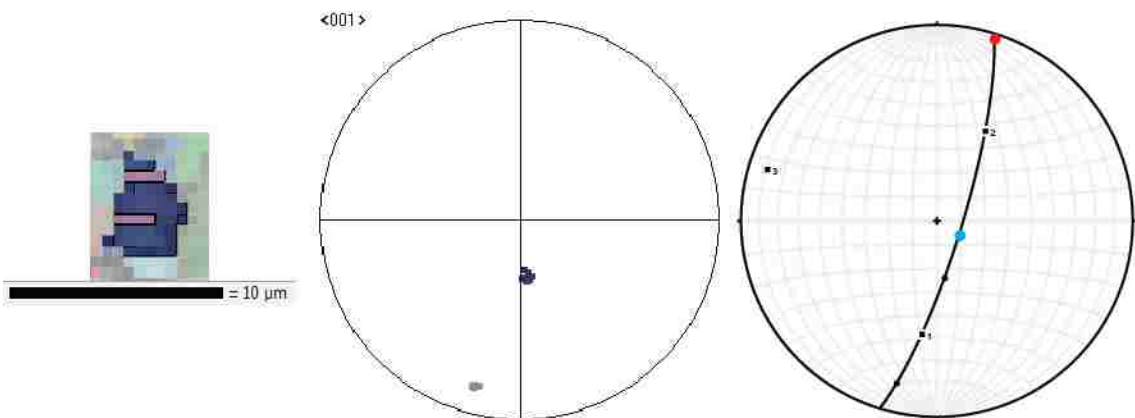
Grain 10



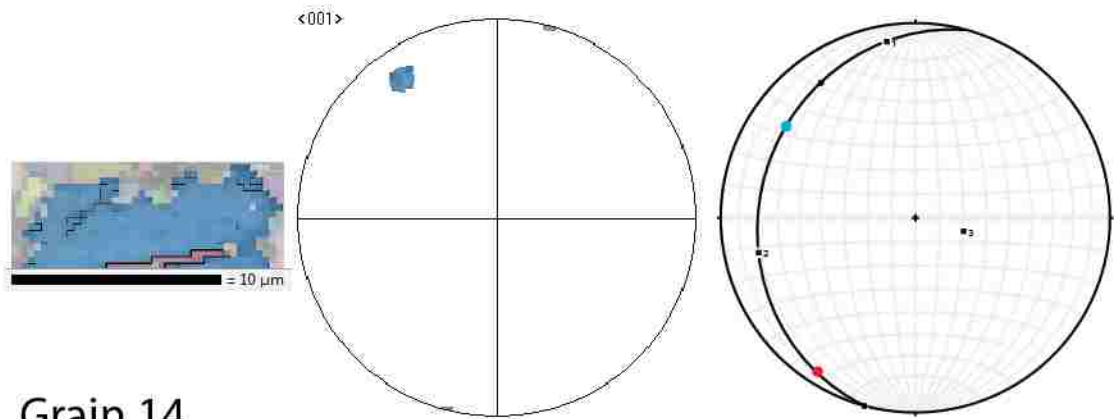
Grain 11



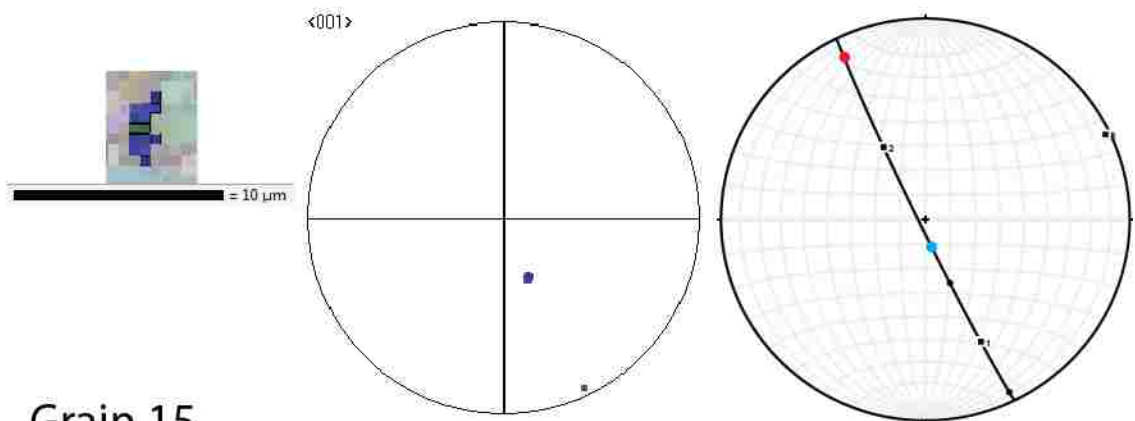
Grain 12



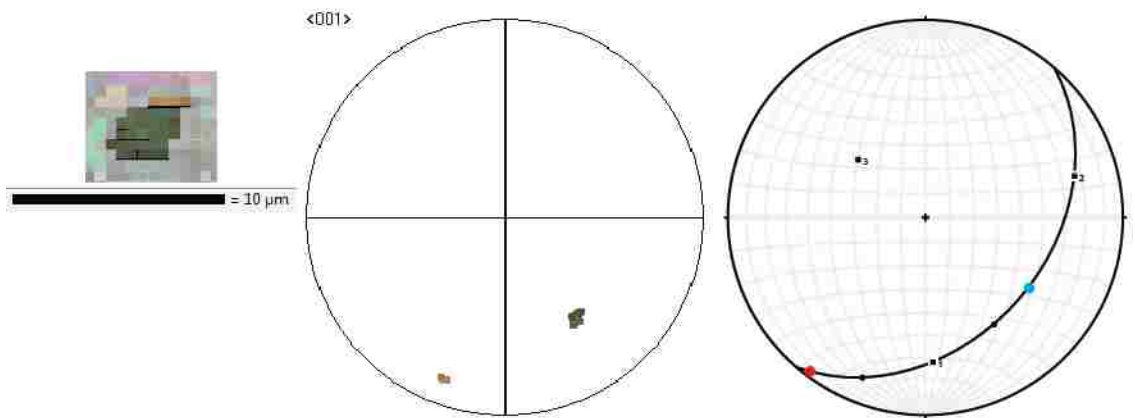
Grain 13



Grain 14



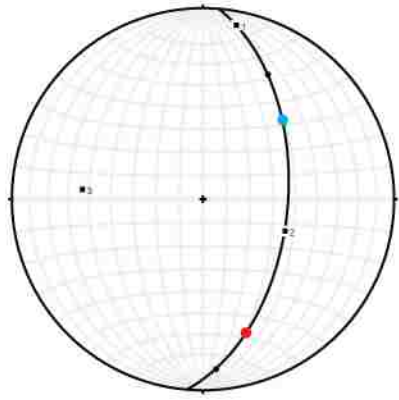
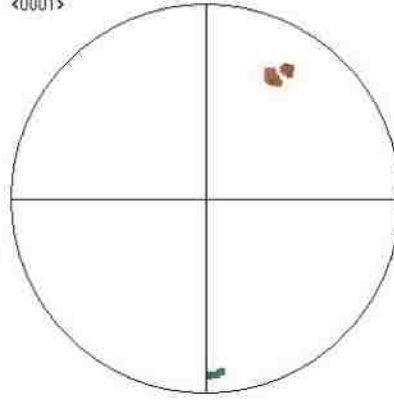
Grain 15



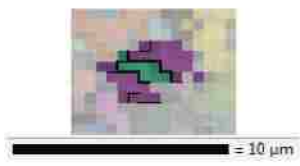
Grain 16



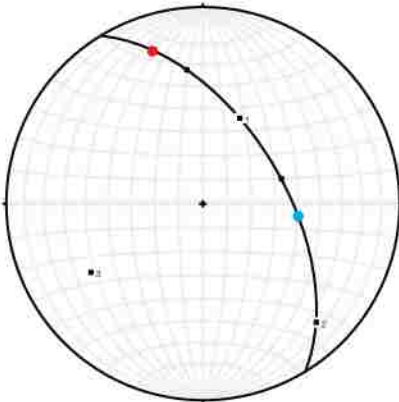
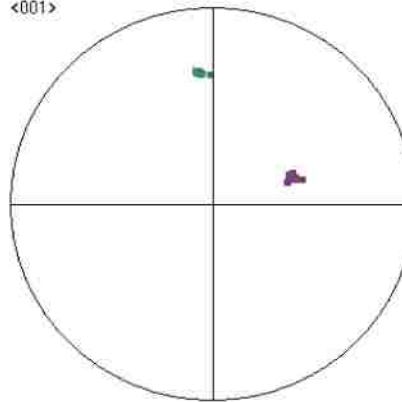
<0001>



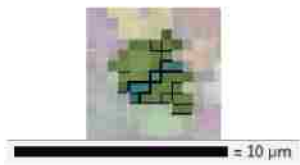
Grain 17



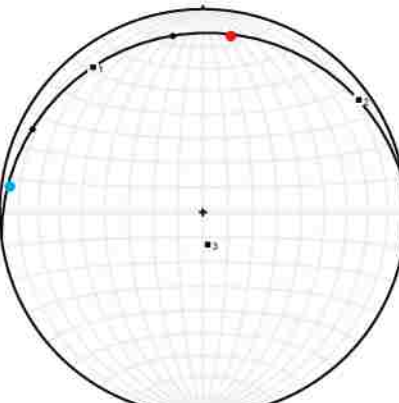
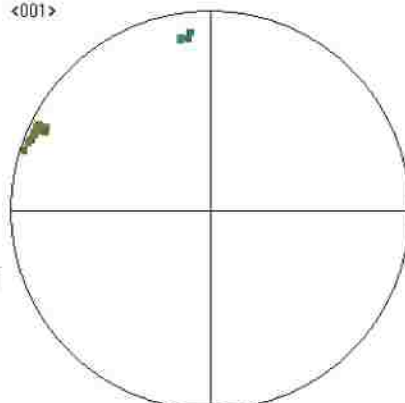
<001>



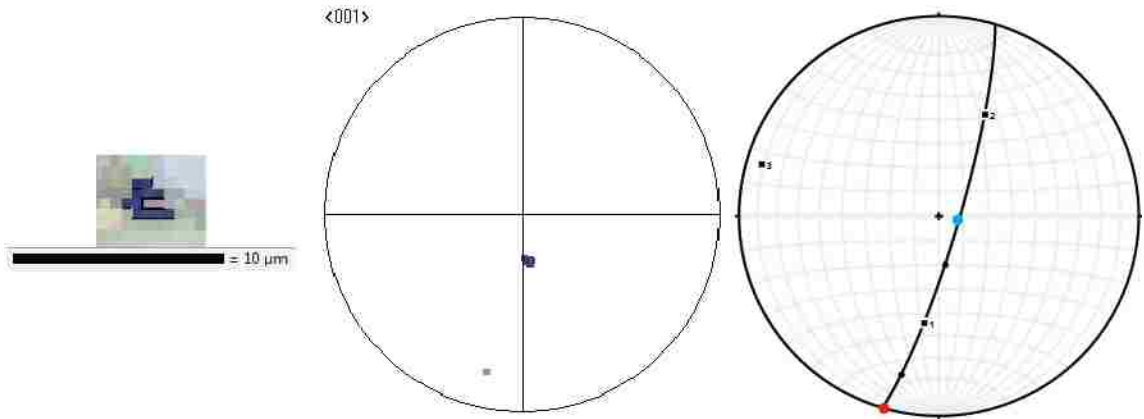
Grain 18



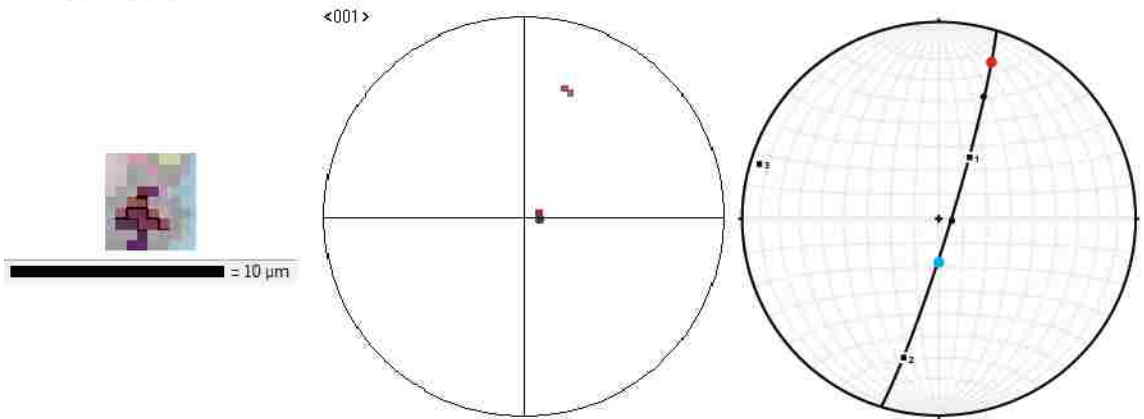
<001>



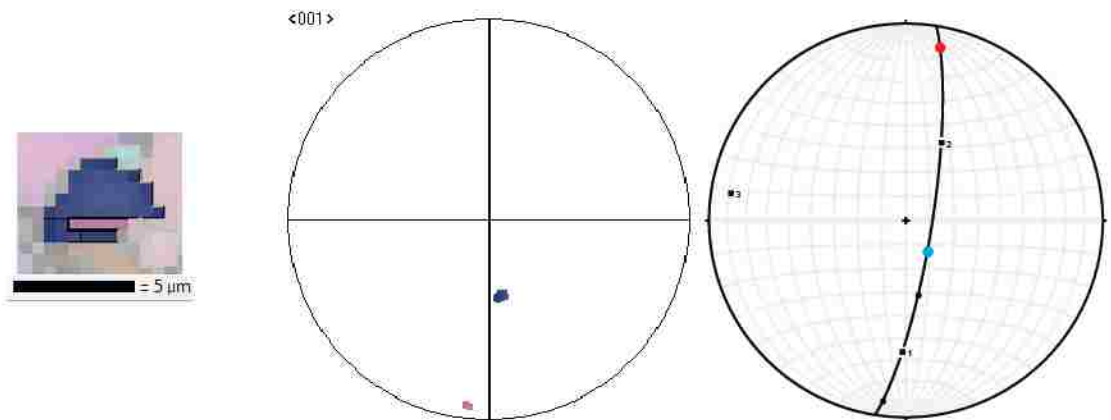
Grain 19



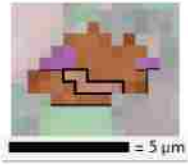
Grain 20



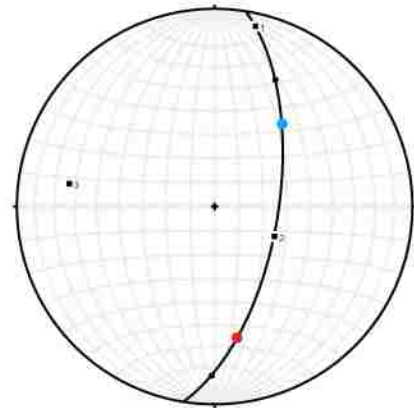
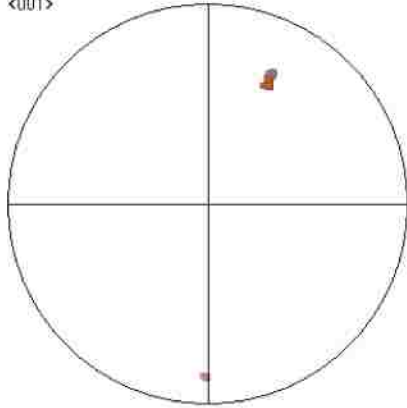
Grain 21



Grain 22



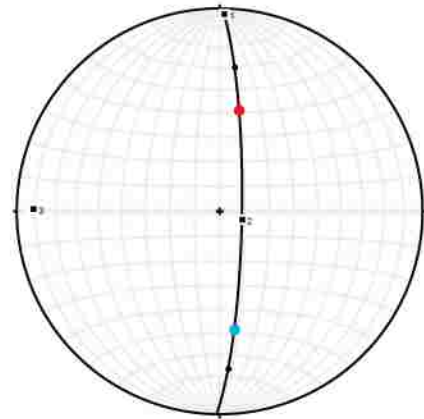
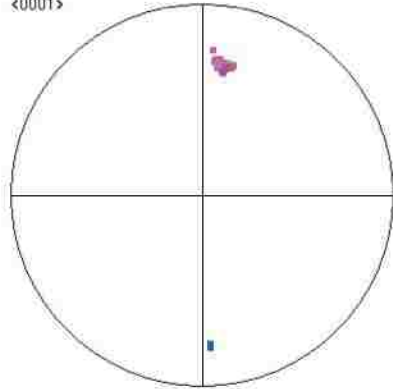
<001>



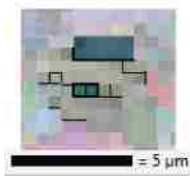
Grain 23



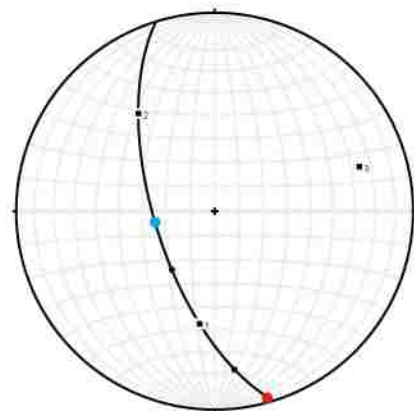
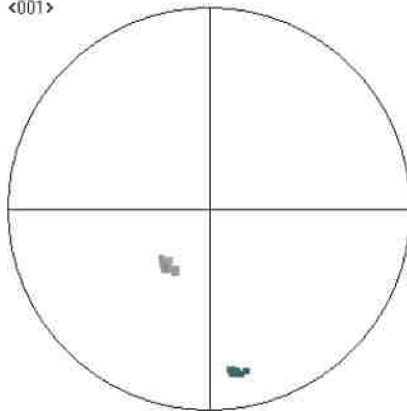
<0001>



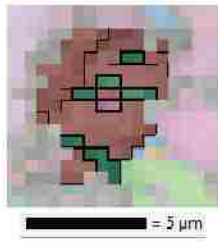
Grain 24



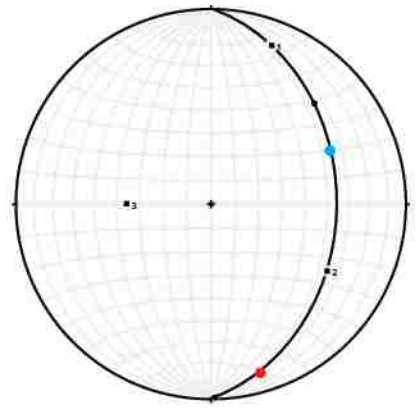
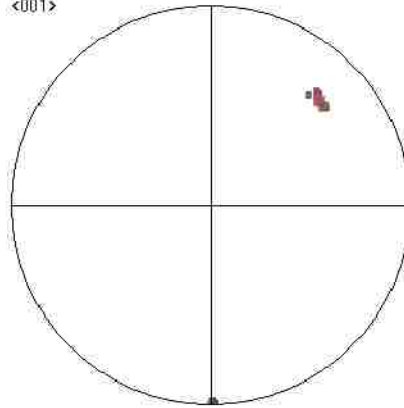
<001>



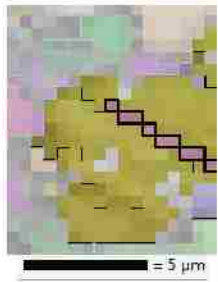
Grain 28



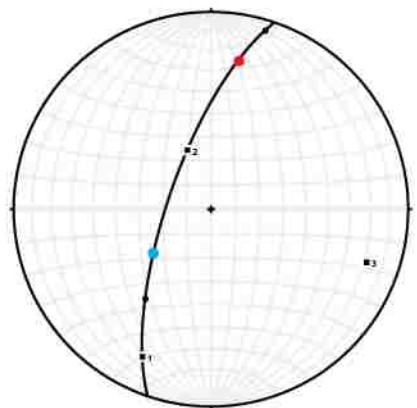
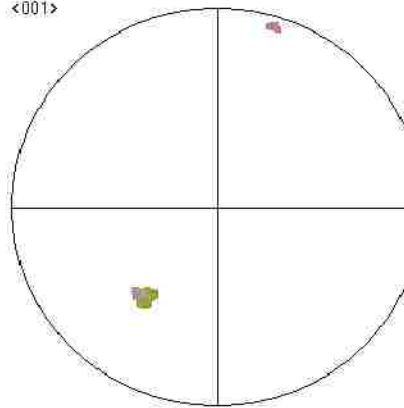
<001>



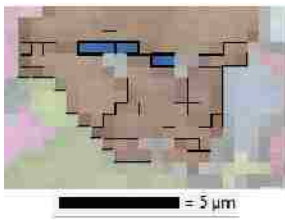
Grain 29



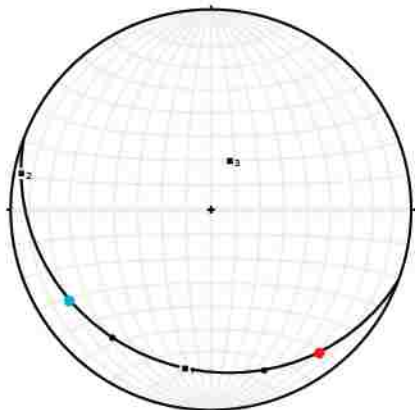
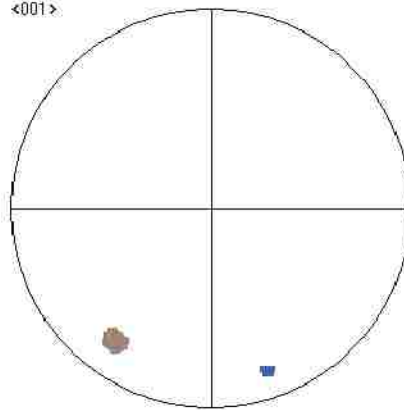
<001>



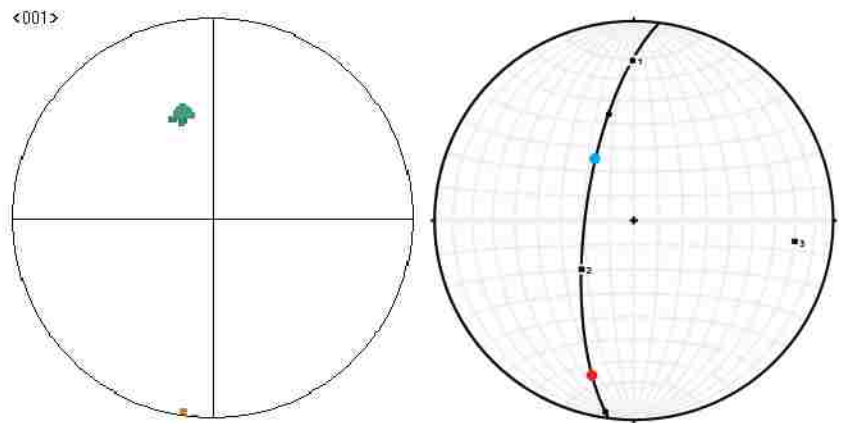
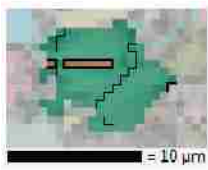
Grain 30



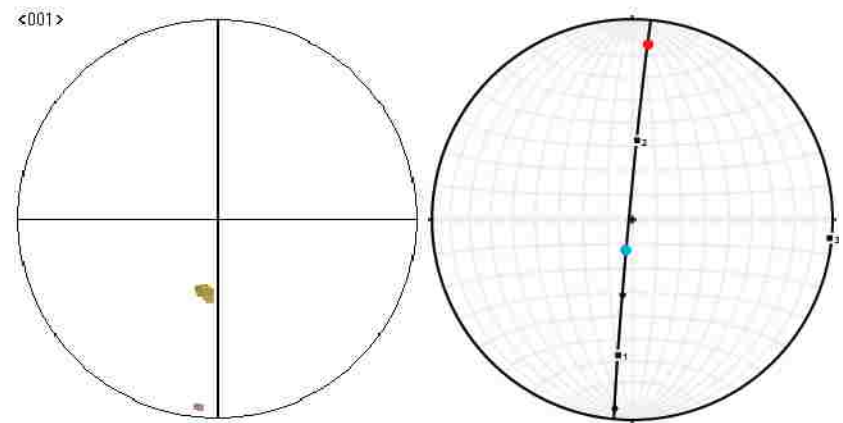
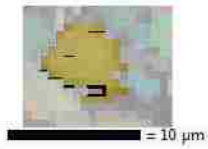
<001>



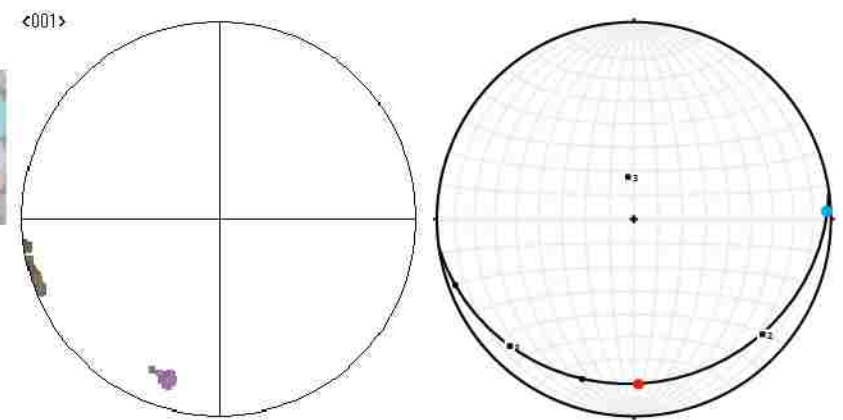
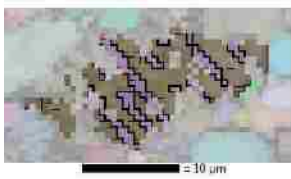
Grain 31



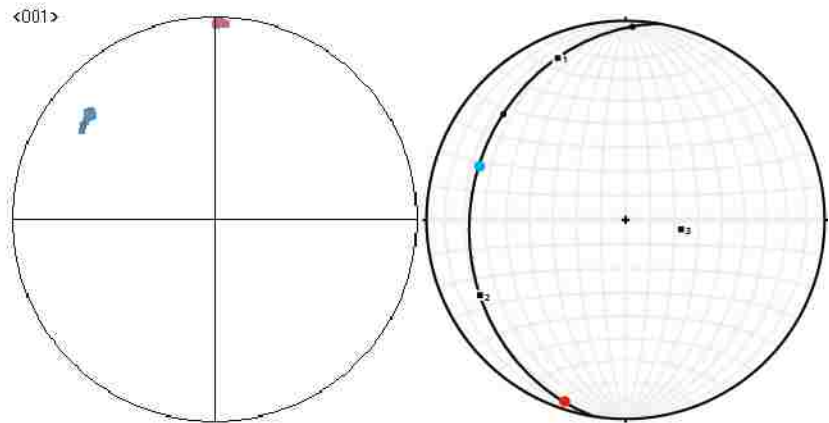
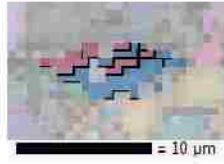
Grain 32



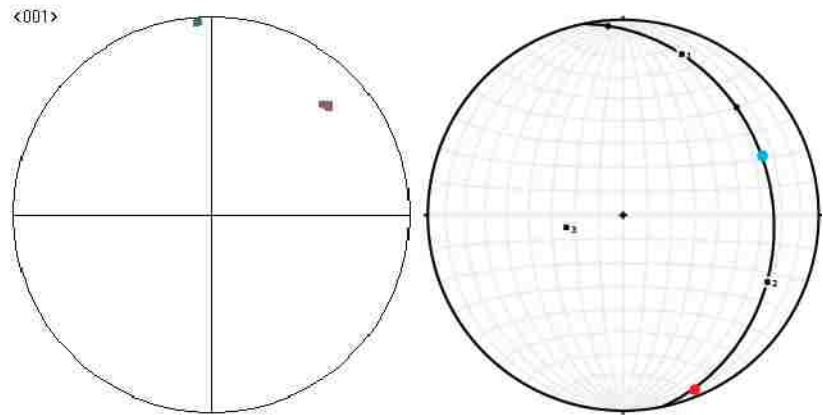
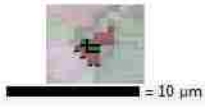
Grain 33



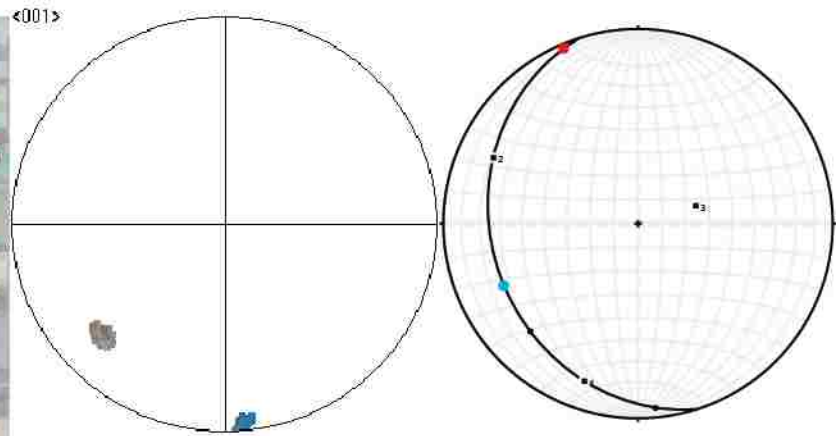
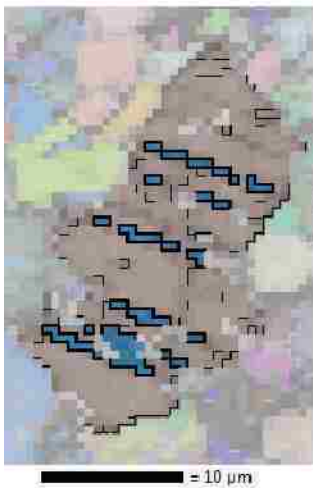
Grain 34



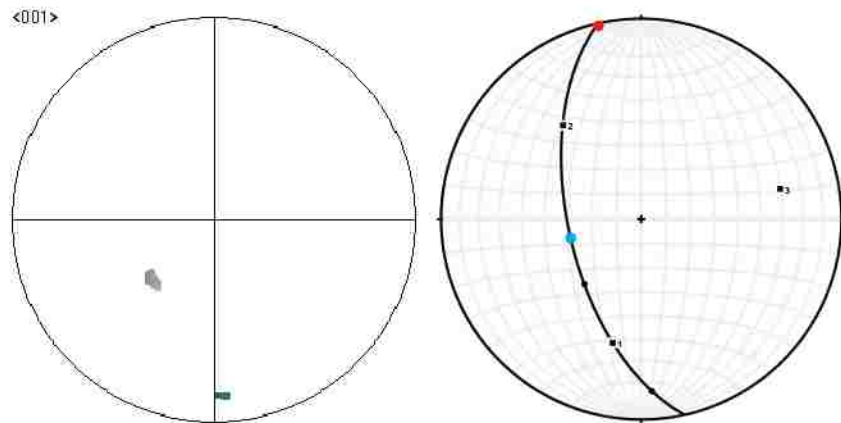
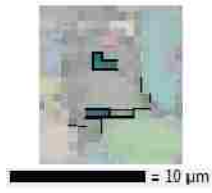
Grain 35



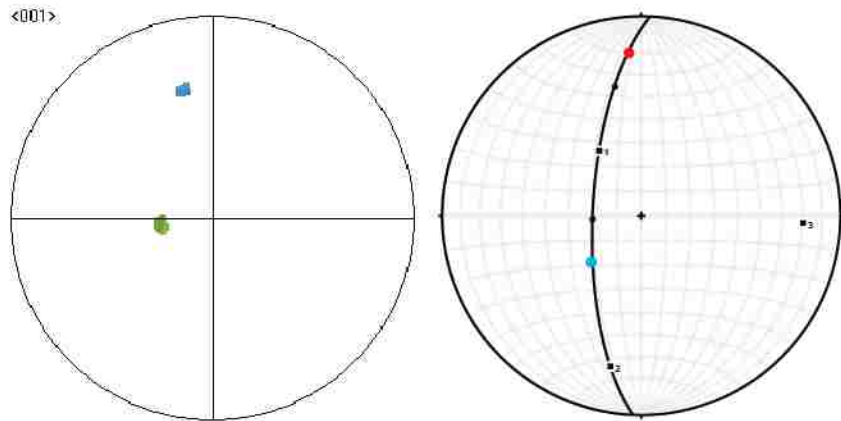
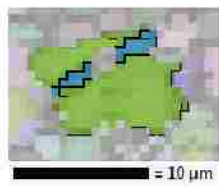
Grain 36



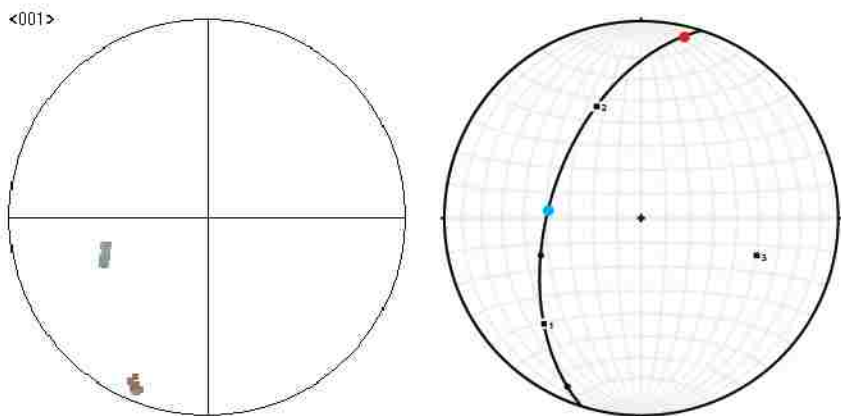
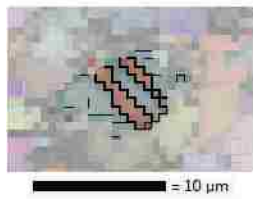
Grain 37



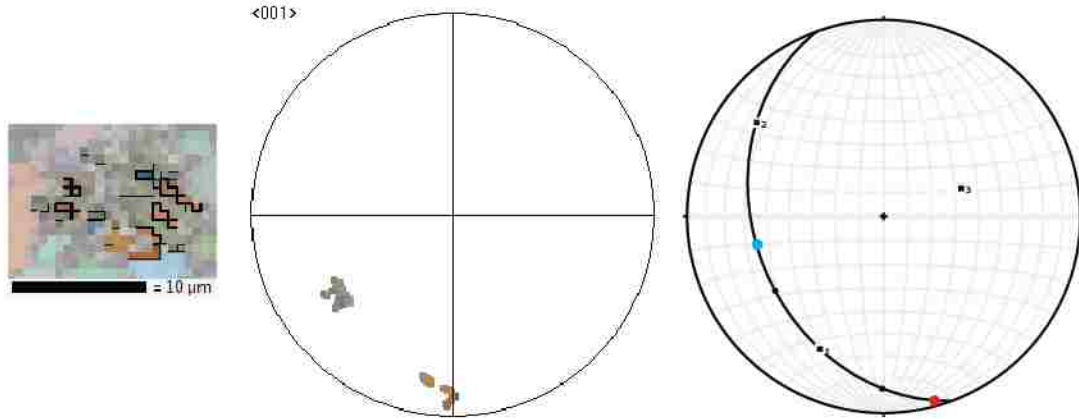
Grain 38



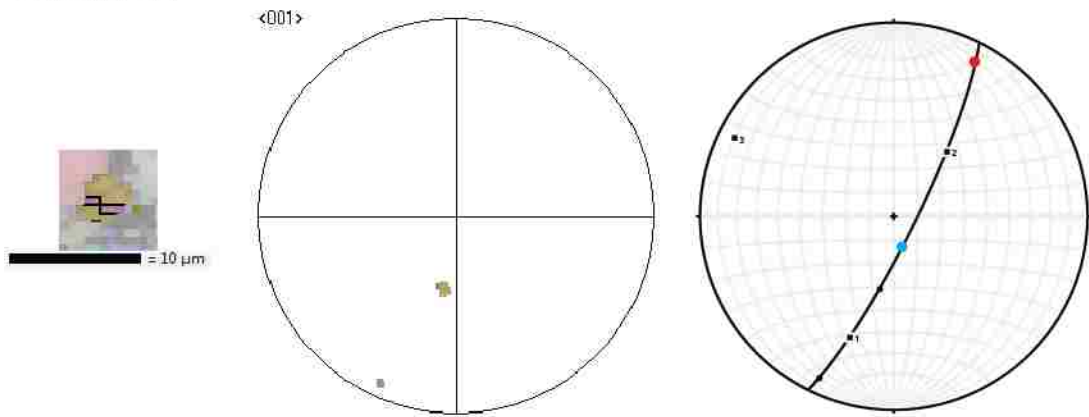
Grain 39



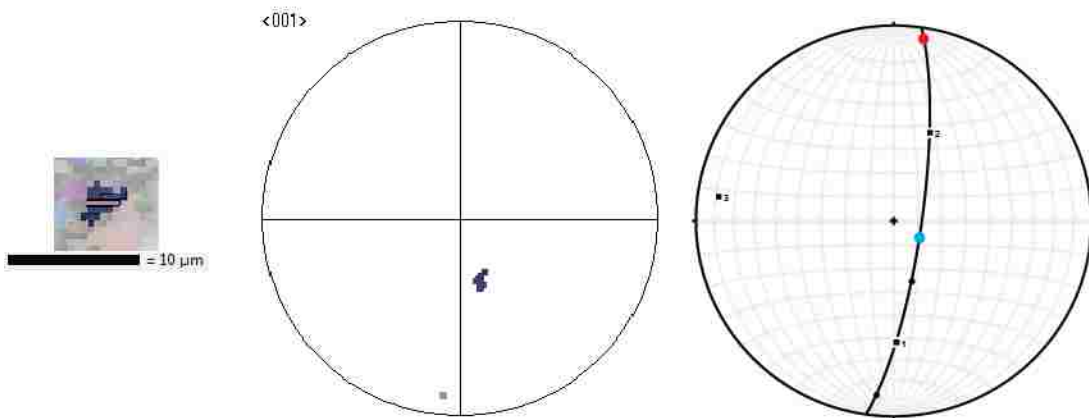
Grain 40



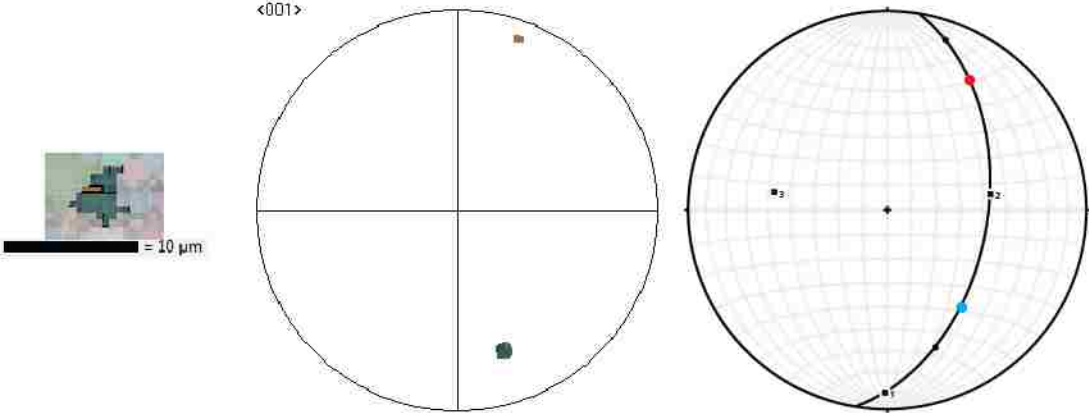
Grain 41



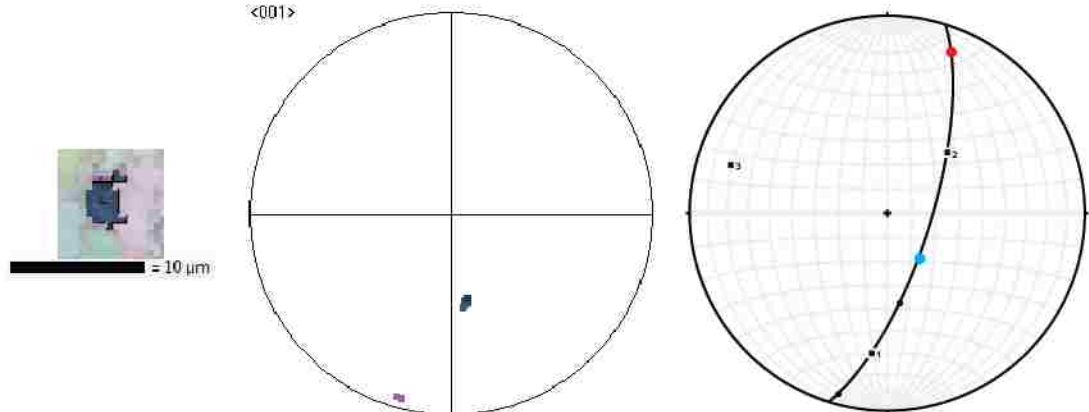
Grain 42



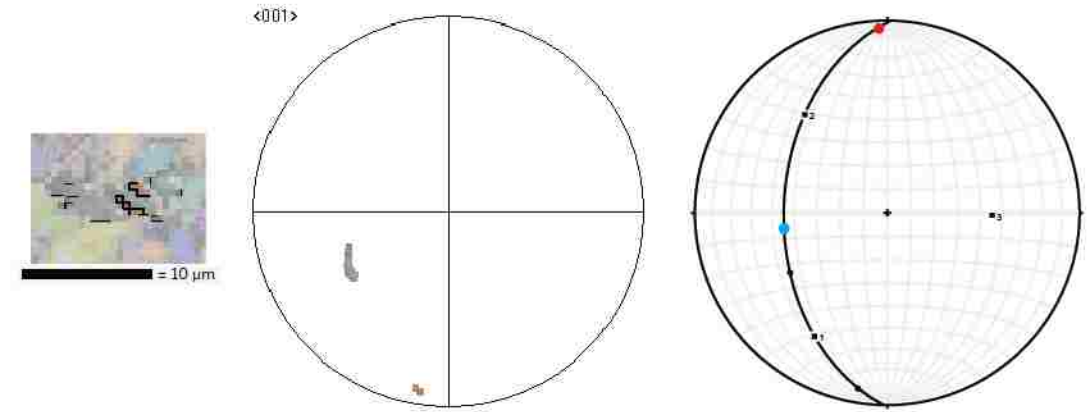
Grain 43



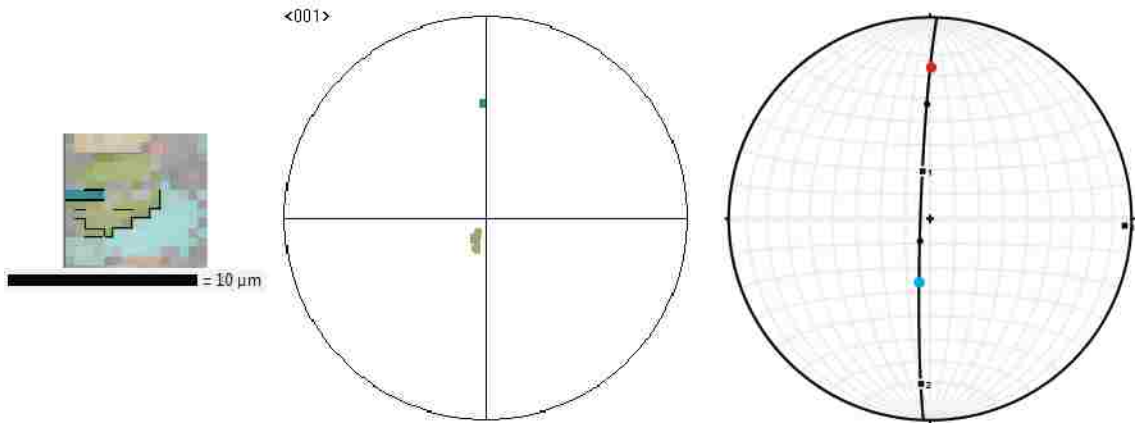
Grain 44



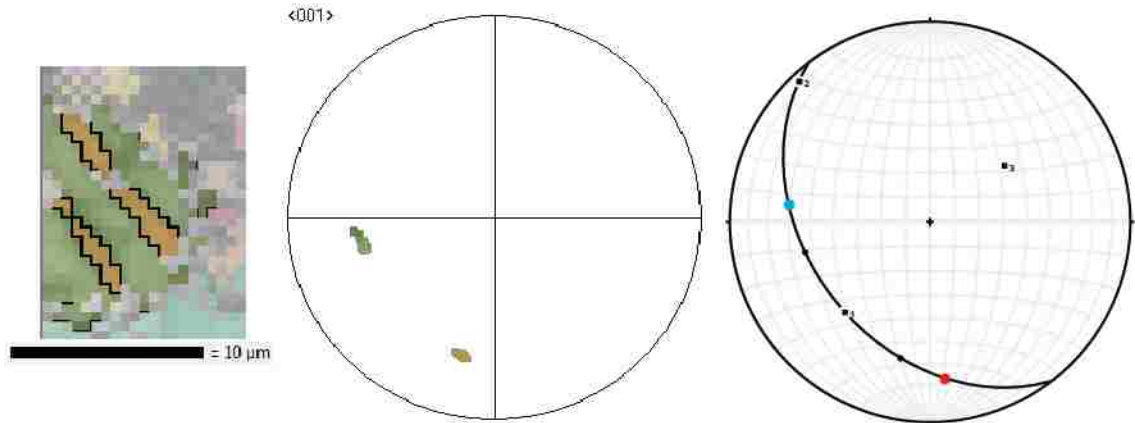
Grain 45



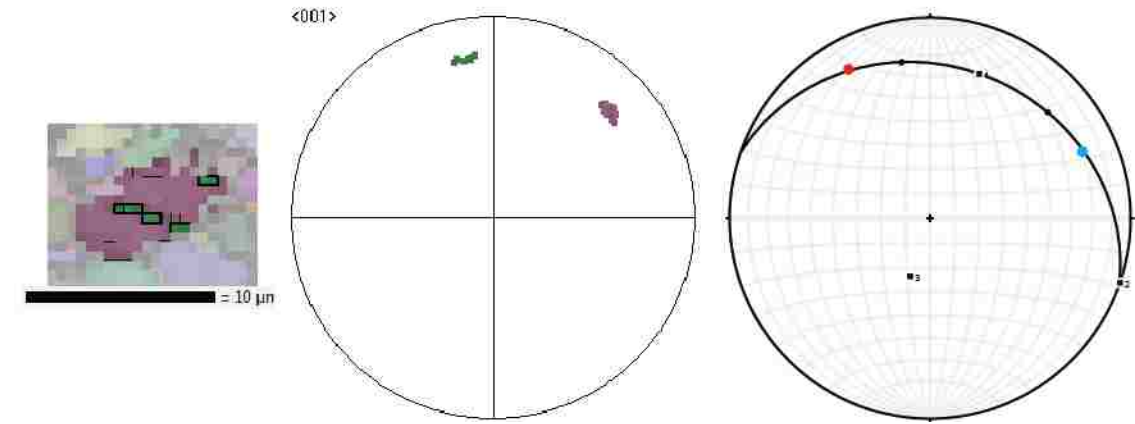
Grain 46



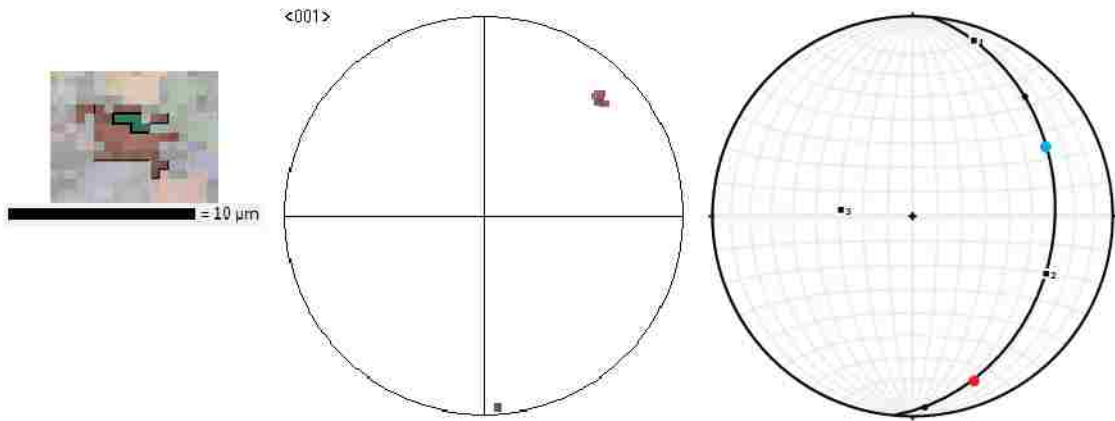
Grain 47



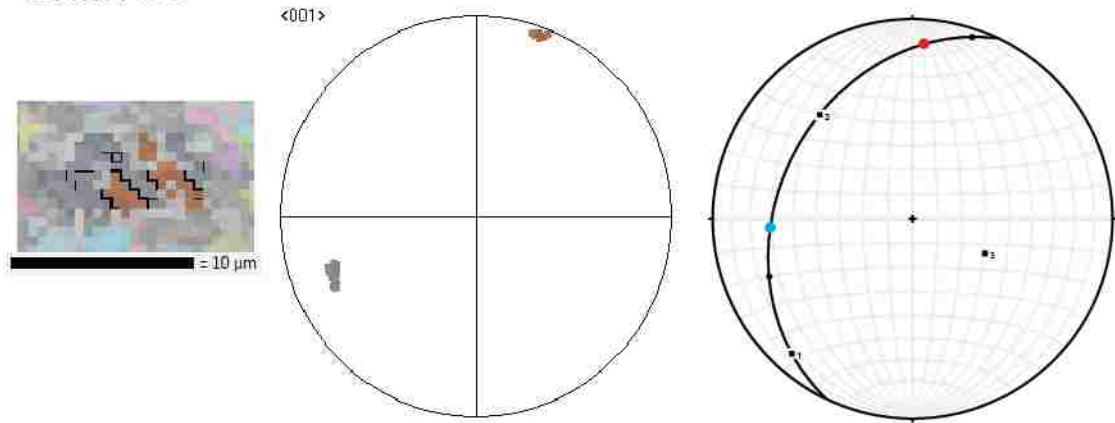
Grain 48



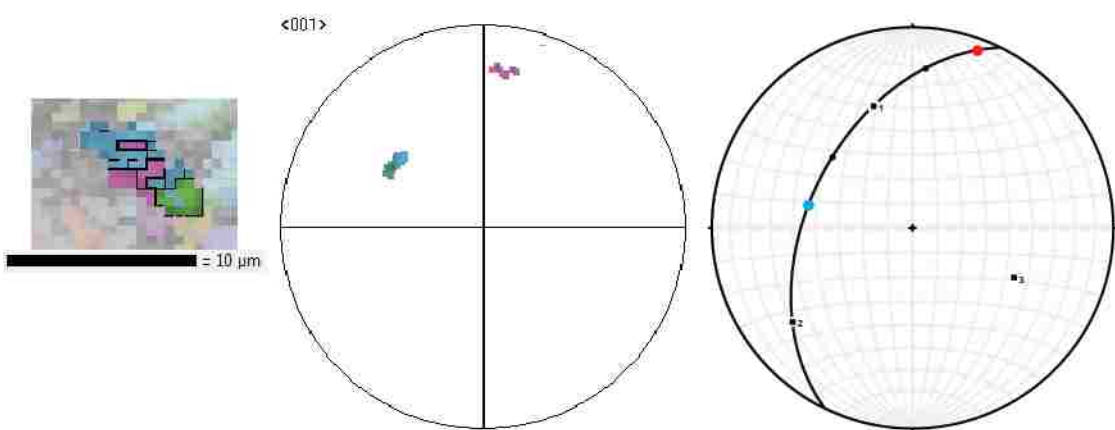
Grain 49



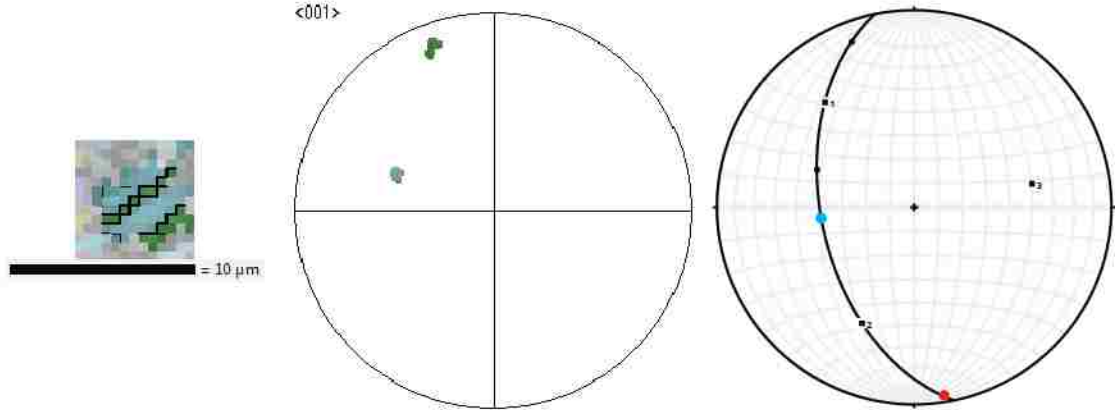
Grain 50



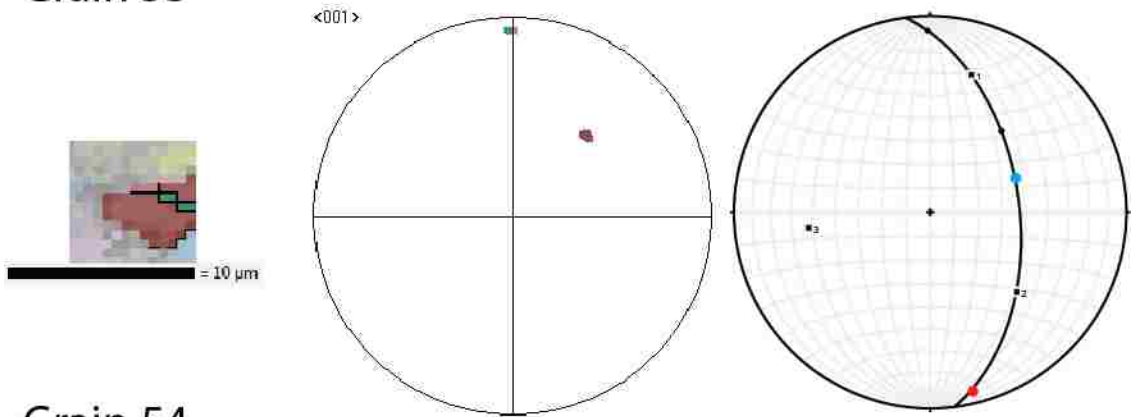
Grain 51



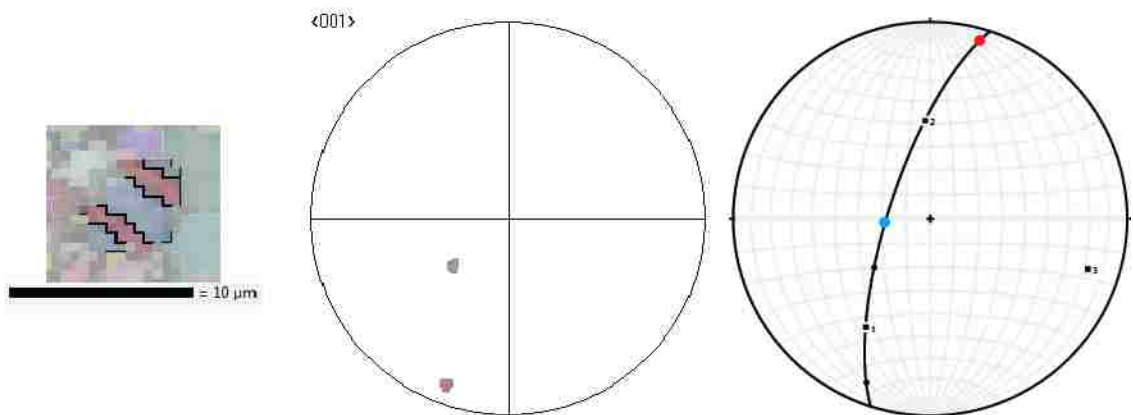
Grain 52



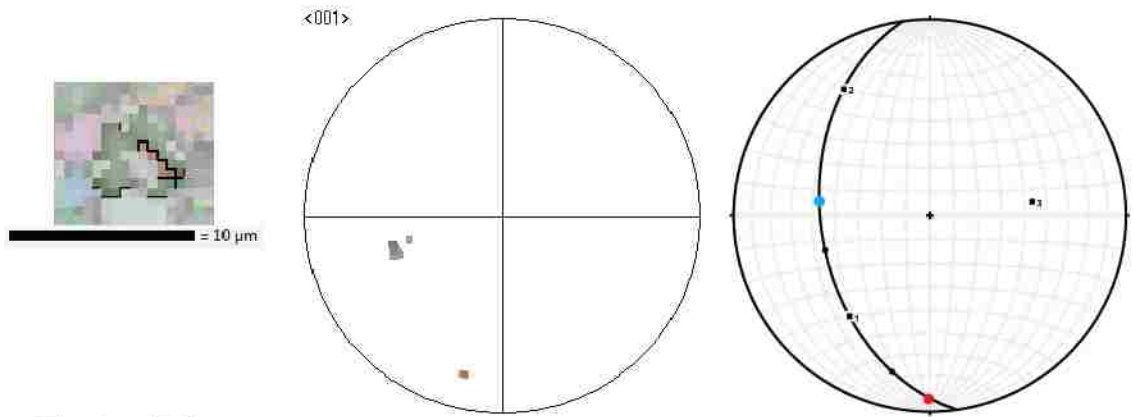
Grain 53



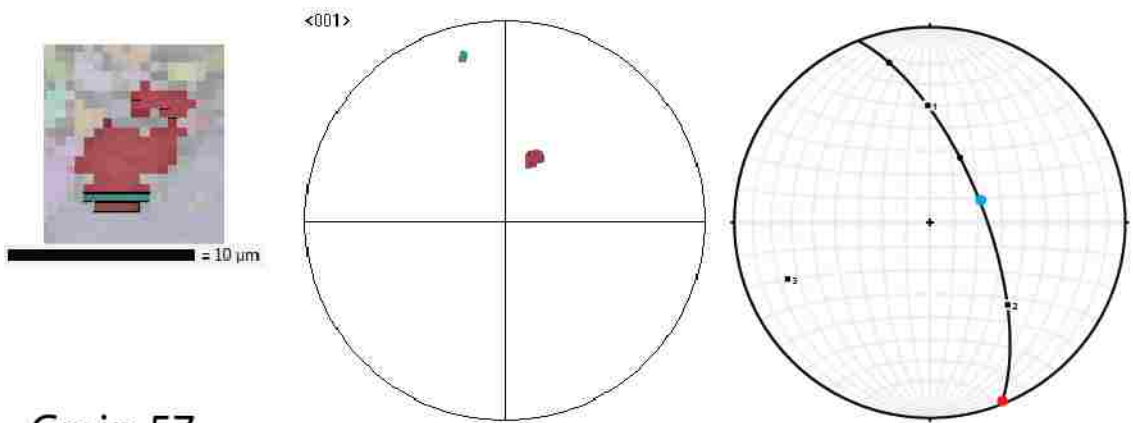
Grain 54



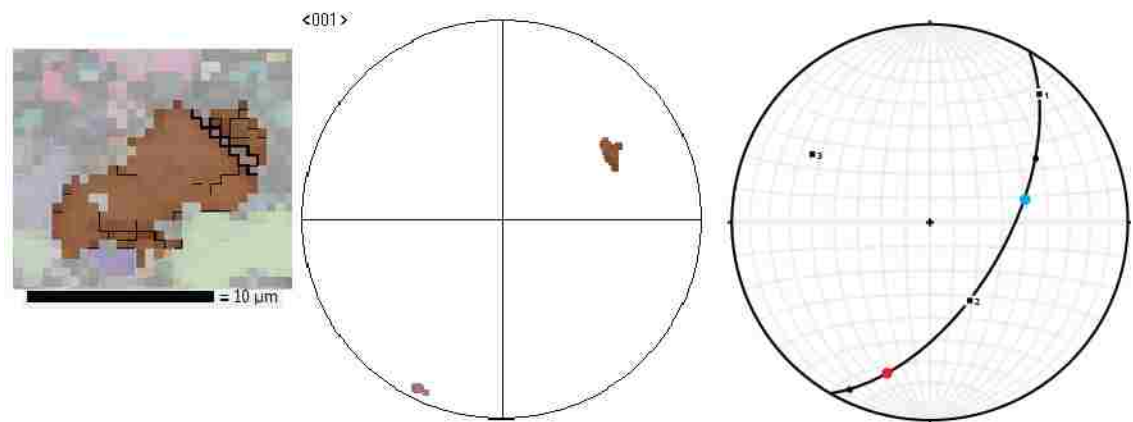
Grain 55



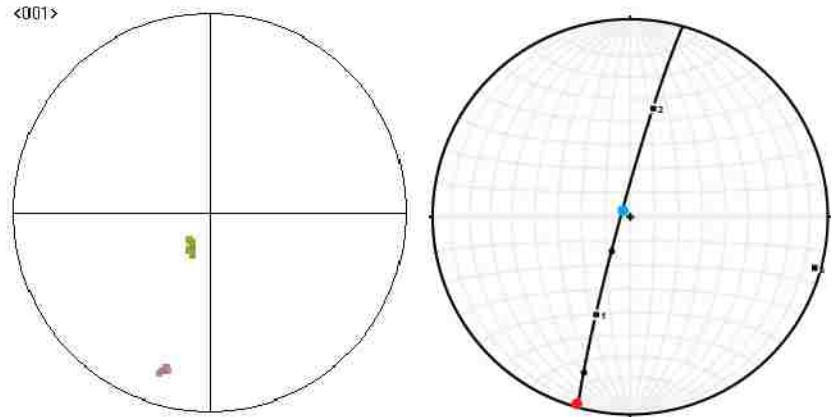
Grain 56



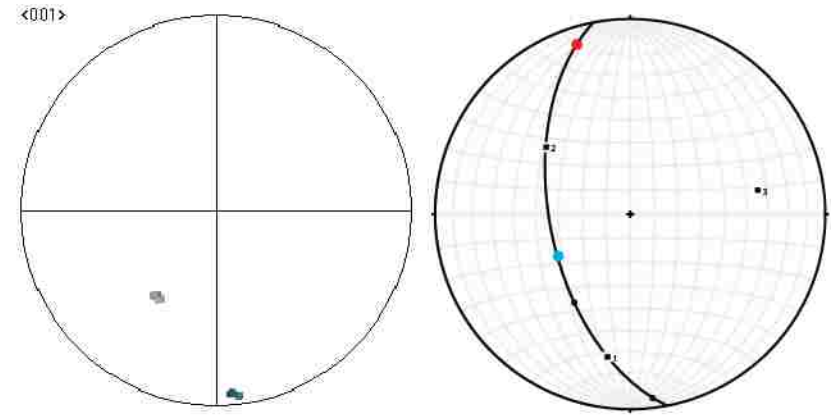
Grain 57



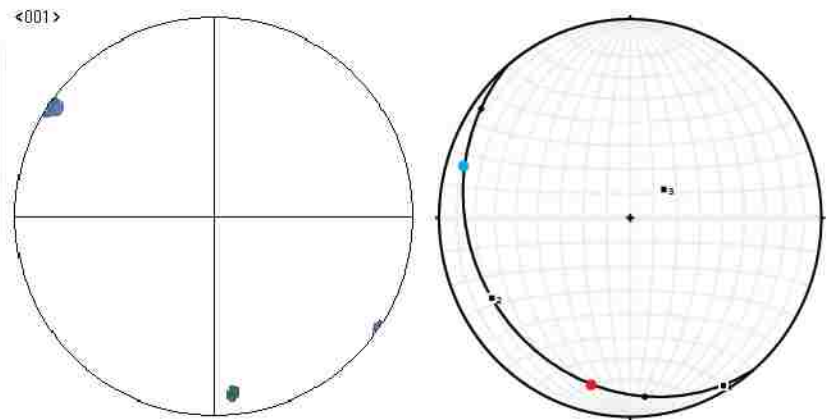
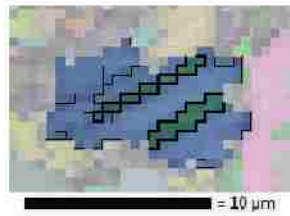
Grain 58



Grain 59



Grain 60



Appendix B: Calcite twin numerical data

This section list the C-axis trend and plunge of both host and twin domains in each twinned grain that have been calculated using the average Euler orientation of each respective domain. From the C-axis measurements the e-plane pole is calculated and thusly the preferred compression and tension direction which caused the deformation twinning.

SFN_002										
Grain #	C-axis host		C-axis twin		e-plane pole		Compression direction		Tension direction	
	trend	plunge	trend	plunge	trend	plunge	trend	plunge	trend	plunge
1	350.1	16.7	22.7	67	359.4	42.8	165.6	0.5	73.8	75.6
2	288	18.4	343.6	16	316	19.3	2.2	11.7	268.9	15.4
3	202.6	42.2	350.7	0.5	184.2	21.6	340.7	17.1	225.2	54.5
4	306.7	25.2	165.9	11	327.1	7.5	180.4	23.6	288.8	35.8
5	329.1	30.3	191.4	3	351.9	14.6	205.7	15.5	308.6	38.6
6	132.4	52	193.4	26.1	169.2	43.1	206.5	11.7	102.4	49.8
7	190.6	43.7	351.1	4.7	179.3	19.8	344.8	22.9	207.1	60.3
8	26.1	46.6	190.2	5	10.7	21.3	173.8	20.5	43.6	59.8
9	223.6	65	166.9	26	184.2	48.6	158.6	9.1	268.2	64.6
10	201.6	42.3	350.7	0.6	183.8	21.5	341	17.5	224.1	55.1
11	308.9	66.7	18.8	32.8	358	54.4	27.9	15.8	266.7	61.3
12	172.4	66.1	194	15.9	187.6	41.4	17.4	2.7	121.8	79.2
13	324.9	16.3	195.3	0	350.7	9	213.1	6.6	305.4	19.6
14	159.3	62.5	154.5	5.7	156	34.1	333.7	10.8	167.7	78.8
15	147.3	36.1	201.6	14.1	177.1	27.7	216.6	3.1	124.3	37.1
16	27.3	27.2	175.7	12	10.7	7.9	161.9	27.5	45.1	41
17	72.1	55.7	353	31.8	23.1	50.8	342.1	19.4	96.8	49.9
18	296	7.2	350.2	12.8	322.8	11.2	8.8	12.3	278	3.5
19	172.7	70.1	193.4	19.8	187.9	45.3	196.2	0.9	100	81.7
20	97.6	84.8	19.9	34.2	26.9	61.4	19	16.8	181	72.4
21	170.7	58.5	187.3	8.4	181.6	33.7	11	10.4	143.7	74.9
22	25.4	29.6	181.1	15.8	12.6	7.1	170.5	32.7	39.5	45.6
23	5.9	29.3	176.9	23.4	1.3	3	172.9	41.3	10.6	47.3
24	216.5	60.1	173	20.9	187.8	42.4	164	2.7	259.9	65
25	311.3	1.5	182.9	23.6	155.9	12.2	201.1	28	296.4	9.8
26	142.4	62.3	186.6	21.1	172.2	43.6	194.5	3.2	97.1	66.9
27	355.2	34.4	172.1	15.7	353.5	9.4	170.6	35.5	357.5	54.3
28	45.6	26.9	178.9	1.2	20.8	13.9	163.6	11.9	65.7	33.1
29	216.4	43.1	16.8	6	205.1	18.8	10.5	23.9	232	59.4
30	217.8	20.5	161.7	16.9	189.4	21	143.3	11.9	237.1	17.5

SFN_004											
Grain #	C-axis host		C-axis twin		e-plane pole		Compression direction		Tension direction		
	trend	plunge	trend	plunge	trend	plunge	trend	plunge	trend	plunge	
31	346.6	44.2	188.6	3.5	359.4	20.7	195.5	21.5	328.3	60	
32	187.6	59	185.4	6.1	186.2	32.6	5	12.4	191.5	77.5	
33	249.9	3.7	198.1	16	224.5	10.9	178.5	17.6	87.8	2	
34	310.8	19.8	1.9	3.1	337.2	12.7	199.2	4.1	290.9	22.4	
35	46.2	21	355.3	3.1	19.8	13.3	158.2	4.6	66.2	23.9	
36	225.2	22.8	174.7	5.7	198.9	15.7	337.2	2.4	246.1	25.2	
37	221.5	54.5	176.6	15.3	193.2	36.9	347	1	255.3	60	
38	266.2	69.9	348.3	34.1	327	57.9	355.6	18.1	226.7	62.5	
39	250	44.7	203.9	7.6	222.9	28	12.7	6.3	275	50.7	
40	235.8	33.5	180.6	13.6	205.9	26.2	165.2	3.7	257.7	34	
41	191.1	58.7	204.8	8.9	200.1	34	27.9	10.4	166	76.2	
42	163.8	63.8	185.7	11.6	178.9	38.1	9.2	5.9	126	77.1	
43	160.7	28	18.8	10.5	180.8	9.2	32.3	23.7	142.9	38.9	
44	172.2	52.2	195.2	5.9	186.5	29.5	21.6	13.1	145.4	67.4	
45	238.6	40.4	189.6	8.4	210.7	26.5	356.8	4.3	262.5	44.9	
46	205.4	80.2	358.3	42.4	350.8	70.4	0	25.7	190	63.9	
47	256.5	35.9	192.4	31.1	223.5	38	174	22.4	277.3	29.4	
48	47.8	22.2	349.5	21.9	18.6	24.9	330.9	17.1	66.5	17.5	
49	43	19.1	176.4	5.1	19.1	7.6	159.4	14.1	62.5	25.5	
50	248.2	23.6	18	4.8	222	10.4	3.6	13.5	265.9	29.2	
51	311.5	45.6	4.6	21.2	342.1	36.3	19.4	6.9	282.3	45.8	
52	291.4	45.9	339.3	11	319.7	30.6	171	3.1	264.8	50.7	
53	40.9	44.1	359.1	8	16.5	27.6	167.2	7.3	67.8	51.5	
54	229.2	59.1	201.4	11.9	210.9	36.2	15.6	6.5	266	71.4	
55	251.9	43.1	193.8	19.4	218.8	34.7	179.9	7.4	276.7	42.6	
56	24.6	59.9	345.6	16.5	358.8	39.7	158.1	1.1	65.4	67.3	
57	58.7	37.7	205.7	7.1	40.3	15.9	195.6	22.1	77	49.7	
58	208.8	74	196.7	19	199.4	46.6	195.5	1.7	309.8	85.8	
59	212.5	45.5	173.1	5.8	189.2	27	342.4	9.7	238.6	54.2	
60	305.2	4.9	175.2	10.9	150	3.3	194.1	15.1	286.9	10.4	

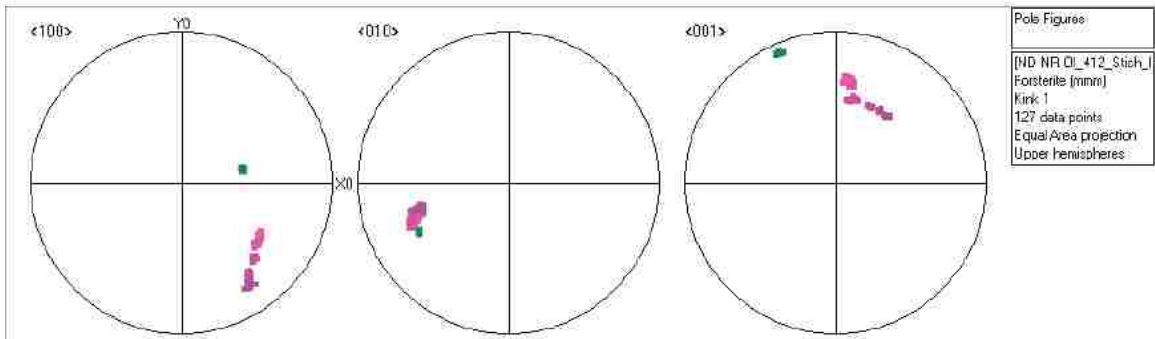
Appendix C: Olivine kink analysis from EBSD orientation maps

Image of kinked grains is cropped from the larger EBSD orientation map. Also included is the pole figure for each kinked grain which shows the [100], [010], and [001] axes.

Kinked grain 1



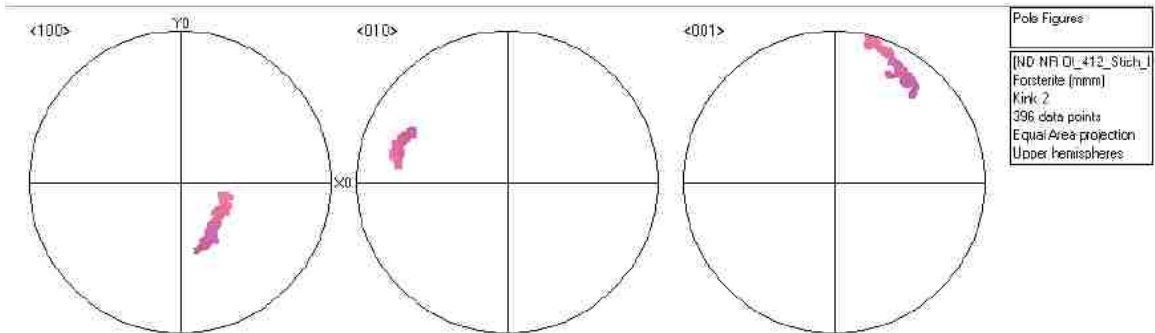
 = 50 μm



Kinked grain 2



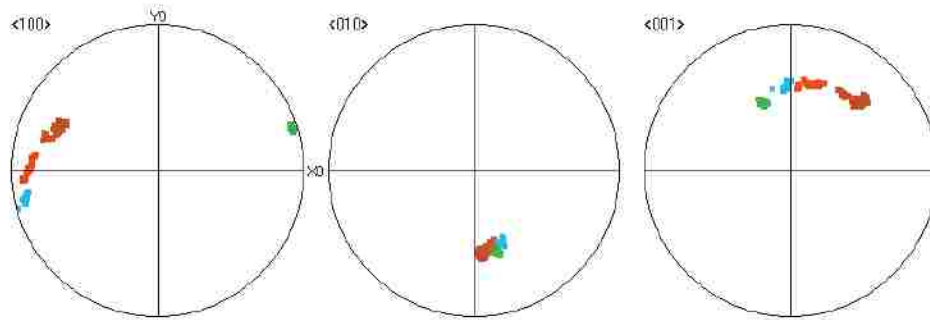
 = 50 μm



Kinked grain 3



= 50 μm

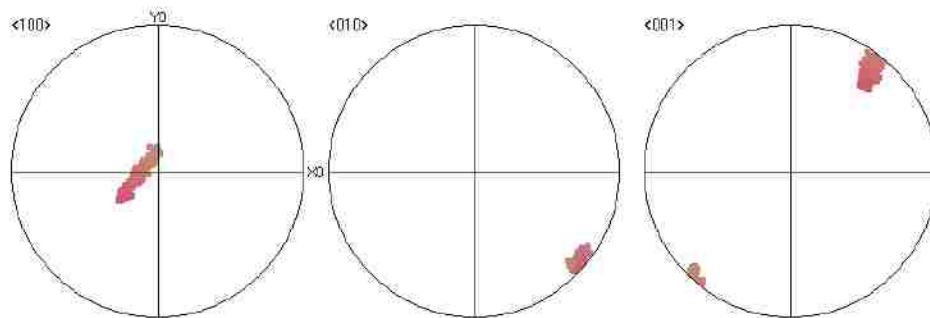


Pole Figures
[ND NR 01_412_Stich_1]
Forstite (rmm)
Kink 3
413 data points
Equal Area projection
Upper hemispheres

Kinked grain 4

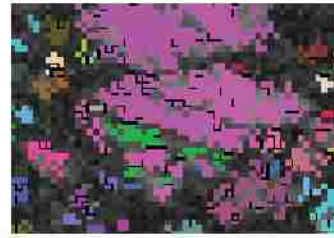


= 50 μm

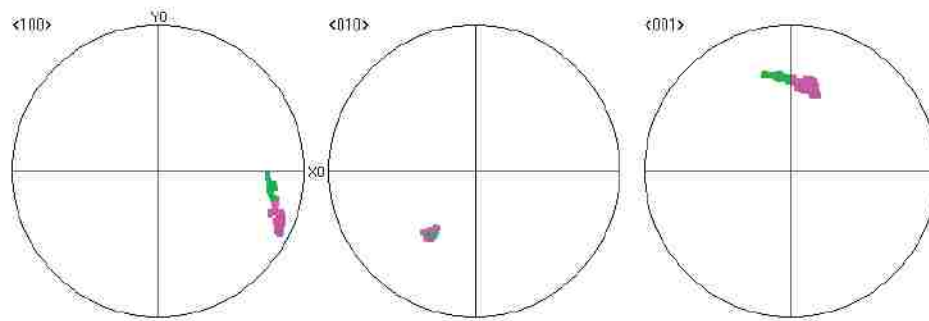


Pole Figures
[ND NR 01_412_Stich_1]
Forstite (rmm)
Kink 4
736 data points
Equal Area projection
Upper hemispheres

Kinked grain 5



= 50 μm

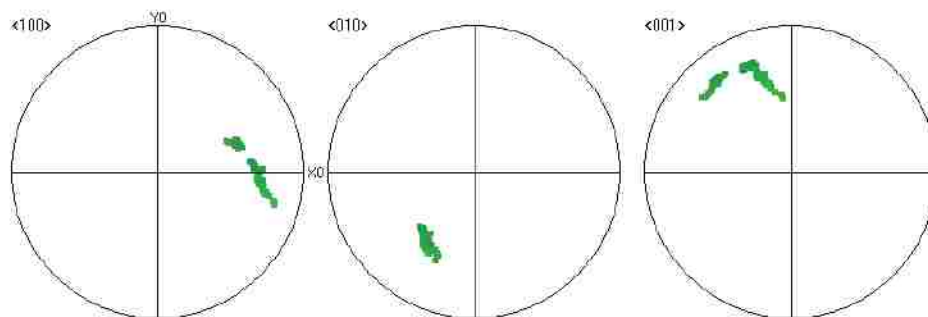


Pole Figures
[ND] NR_01_412_Stich_1
Forsterite (mm)
Kink 5
329 data points
Equal Area projection
Upper hemisphere

Kinked grain 6

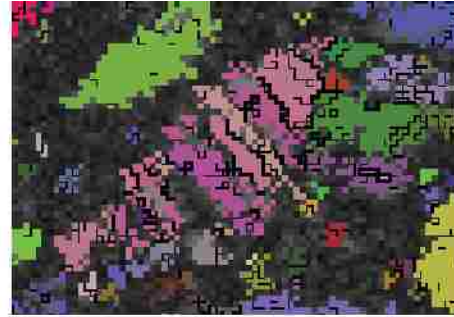


= 50 μm

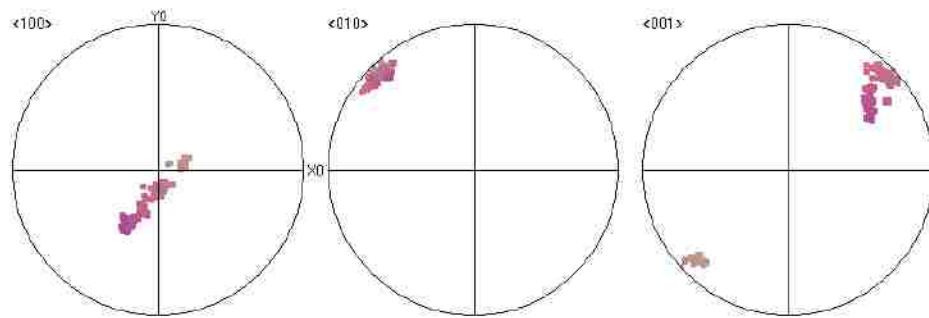


Pole Figures
[ND] NR_01_412_Stich_1
Forsterite (mm)
kink 6
222 data points
Equal Area projection
Upper hemisphere

Kinked grain 7

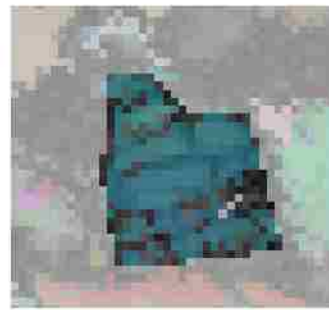


= 50 μm

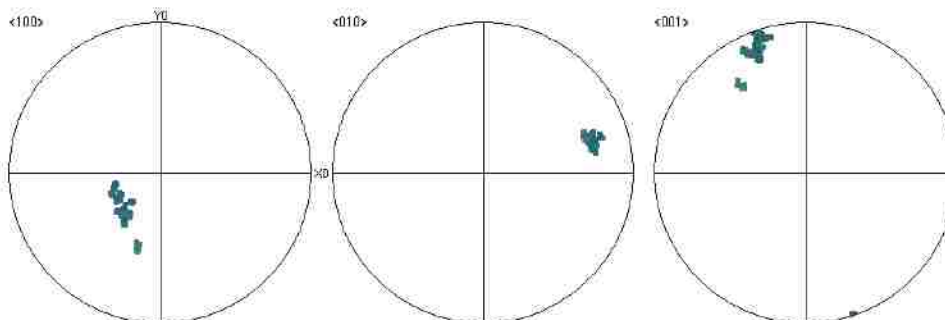


Pole Figures:
[ND NR OL_412_Stich_1]
Foisterite (mm)
Kink: 7
494 data points
Equal Area projection
Upper hemispheres

Kinked grain 8



= 50 μm



Pole Figures:
[ND NR OL_412_Stich_1]
Foisterite (mm)
Si4x23
265 data points
Equal Area projection
Upper hemispheres

Appendix D: Olivine kink numerical data

Conversion of euler orientation of each kinked grain in sample OI_412 into trend and plunge for use in determining compression direction. Mean vector is the the colution to Eigenvector analysis which was used in determining the spread of compression directions amongst the kinked grain population.

OI_412						
Kink	e1	e2	e3	c-axis	trend	plunge
1	170.1	56.7	135.3	east	9.9	33.3
2	157.2	81.3	115.5	east	22.8	8.7
3	166.8	50.5	17.9	east	13.2	39.5
4	143.5	80.6	82	east	36.5	9.4
5	178.3	53.9	157.2	east	1.7	36.1
6	19.9	113.8	38.7	west	340.1	23.8
7	135.5	81.2	96.6	east	44.5	8.8
8	20.5	102.1	116.3	west	339.5	12.1
mean vector	trend	plunge				
	11.6	23.1				

Appendix E: Rotation of elastic tensors for finite element models

This section will detail each of the 14 elastic tensors used in material specific finite element models. The boxed numbers are the three Euler angles used in the rotation, followed by the 6x6 elastic stiffness matrix with the bold number representing which of 14 subpopulations the tensor belongs.

Olivine rotated elastic tensors

30	0	0					
255.1188	74.35625	63.075	0	0	-35.9942		
74.35625	193.2688	66.225	0	0	-17.5695		
63.075	66.225	213.5	0	0	2.72798		1
0	0	0	60.875	-6.01888	0		
0	0	0	-6.01888	67.825	0		
-35.9942	-17.5695	2.72798	0	0	85.55625		
0	90	-30					
182.1125	72.7875	59.175	0	0	-4.74149		
72.7875	199.7125	60.725	0	0	-10.5006		
59.175	60.725	302	0	0	-1.34234		2
0	0	0	70.875	-0.73612	0		
0	0	0	-0.73612	70.025	0		
-4.74149	-10.5006	-1.34234	0	0	62.3875		
0	90	45					
189.25	74.45	59.95	0	0	8.8		
74.45	189.25	59.95	0	0	8.8		
59.95	59.95	302	0	0	1.55		3
0	0	0	70.45	0.85	0		
0	0	0	0.85	70.45	0		
8.8	8.8	1.55	0	0	64.05		
60	0	0					
193.2688	74.35625	66.225	0	0	17.56949		
74.35625	255.1188	63.075	0	0	35.99418		
66.225	63.075	213.5	0	0	-2.72798		4
0	0	0	67.825	6.018877	0		
0	0	0	6.018877	60.875	0		
17.56949	35.99418	-2.72798	0	0	85.55625		

0	135	45				
197.3563	70.35625	75.7125	1.847316	10.47402	13.15625	
70.35625	197.3563	75.7125	10.47402	1.847316	13.15625	
75.7125	75.7125	230.925	15.64474	15.64474	12.6125	5
1.847316	10.47402	15.64474	80.8125	17.3125	9.48407	
10.47402	1.847316	15.64474	17.3125	80.8125	9.48407	
13.15625	13.15625	12.6125	9.48407	9.48407	70.75625	

-40	110	-67				
199.6751	66.31914	67.73017	5.698859	-8.39159	-6.18789	
66.31914	236.7007	79.14326	-33.6227	-3.91673	1.6543	
67.73017	79.14326	206.4391	-23.7175	-5.08167	-0.09766	6
5.698859	-33.6227	-23.7175	89.85689	1.602344	-4.47278	
-8.39159	-3.91673	-5.08167	1.602344	65.21655	-4.21027	
-6.18789	1.6543	-0.09766	-4.47278	-4.21027	68.71914	

45	90	-45				
204.7688	76.06875	72.1625	-4.90555	-14.7343	1.34375	
76.06875	204.7688	72.1625	-14.7343	-4.90555	1.34375	
72.1625	72.1625	218.875	-21.8673	-21.8673	7.5125	7
-4.90555	-14.7343	-21.8673	77.6125	13.2625	-12.0473	
-14.7343	-4.90555	-21.8673	13.2625	77.6125	-12.0473	
1.34375	1.34375	7.5125	-12.0473	-12.0473	75.76875	

0	90	60				
215.5063	81.61875	65.45	0	0	-7.54525	
81.61875	259.7563	60.75	0	0	-30.7764	
65.45	60.75	178.3	0	0	4.070319	8
0	0	0	66.55	-5.28275	0	
0	0	0	-5.28275	60.45	0	
-7.54525	-30.7764	4.070319	0	0	91.41875	

45	0	0				
218.875	79.675	64.65	0	0	30.925	
79.675	218.875	64.65	0	0	30.925	
64.65	64.65	213.5	0	0	-3.15	9
0	0	0	64.35	6.95	0	
0	0	0	6.95	64.35	0	
30.925	30.925	-3.15	0	0	90.875	

0	135	45				
223.2375	82.3375	67.2	-3.05824	-4.26032	-28.1875	
82.3375	223.2375	67.2	-4.26032	-3.05824	-28.1875	
67.2	67.2	189.25	-6.22254	-6.22254	7.25	10
-3.05824	-4.26032	-6.22254	67.25	-3.2	-2.56326	
-4.26032	-3.05824	-6.22254	-3.2	67.25	-2.56326	
-28.1875	-28.1875	7.25	-2.56326	-2.56326	92.8375	

0	90	-45				
230.925	88.325	63.1	0	0	22.125	
88.325	230.925	63.1	0	0	22.125	
63.1	63.1	178.3	0	0	-4.7	11
0	0	0	63.5	6.1	0	
0	0	0	6.1	63.5	0	
22.125	22.125	-4.7	0	0	98.125	

60	45	45				
239.2483	64.37617	83.0843	0.9755	-30.5686	7.60904	
64.37617	182.3665	68.07352	2.884301	6.244723	4.015179	
83.0843	68.07352	216.5172	3.968763	-18.6832	5.288281	12
0.9755	2.884301	3.968763	65.72605	6.200781	-3.98001	
-30.5686	6.244723	-18.6832	6.200781	93.10676	-0.50238	
7.60904	4.015179	5.288281	-3.98001	-0.50238	67.30117	

30	45	45				
258.703	70.3668	72.31393	10.33754	-20.8984	-22.834	
70.3668	188.7931	70.33138	7.948384	1.788241	-6.88553	
72.31393	70.33138	195.6797	10.29623	-3.1434	2.607031	13
10.33754	7.948384	10.29623	65.45892	-4.05547	-4.86561	
-20.8984	1.788241	-3.1434	-4.05547	79.8114	12.43054	
-22.834	-6.88553	2.607031	-4.86561	12.43054	78.3418	

0	0	0				
302	58.4	61.5	0	0	0	
58.4	178.3	67.8	0	0	0	
61.5	67.8	213.5	0	0	0	14
0	0	0	57.4	0	0	
0	0	0	0	71.3	0	
0	0	0	0	0	69.6	

Calcite rotated elastic tensors

13	98.8	28.1				
125.3774	61.9838	64.4217	4.0493	5.9165	-20.3463	1
61.9838	88.0872	44.5698	1.3914	4.7231	-9.6012	
64.4217	44.5698	144.4848	4.1491	-8.4256	16.0124	
4.0493	1.3914	4.1491	24.1355	14.4284	4.9748	
5.9165	4.7231	-8.4256	14.4284	50.4828	5.1394	
-20.3463	-9.6012	16.0124	4.9748	5.1394	41.357	

178.5	88	115.3				
143.9368	52.2785	58.7401	-19.6435	1.358	5.7598	2
52.2785	83.2312	54.5142	1.2415	-1.3986	0.8106	
58.7401	54.5142	141.6664	20.6718	-0.0189	-4.8689	
-19.6435	1.2415	20.6718	33.7192	-4.6755	-1.4053	
1.358	-1.3986	-0.0189	-4.6755	45.3261	-19.3855	
5.7598	0.8106	-4.8689	-1.4053	-19.3855	31.4875	

162.6	120	90.6				
124.1682	68.7006	57.765	-5.8343	15.8718	12.5295	3
68.7006	92.667	49.1736	-2.4782	10.8897	3.8199	
57.765	49.1736	131.7865	-18.5867	-18.3318	-2.4168	
-5.8343	-2.4782	-18.5867	28.8699	-0.8331	11.8479	
15.8718	10.8897	-18.3318	-0.8331	42.0186	-8.8919	
12.5295	3.8199	-2.4168	11.8479	-8.8919	49.7506	

171.5	58.8	99.2				
133.8642	54.8847	65.2106	-0.417	-9.647	19.3778	4
54.8847	98.7977	54.7279	13.918	-13.2569	-10.8496	
65.2106	54.7279	117.5918	15.028	18.6403	-1.5653	
-0.417	13.918	15.028	34.0462	-0.7738	-13.7416	
-9.647	-13.2569	18.6403	-0.7738	49.7065	2.826	
19.3778	-10.8496	-1.5653	-13.7416	2.826	36.0705	

31.4	127.3	17.6
------	-------	------

138.9275	61.1317	43.7587	2.8429	22.0135	6.7227
61.1317	115.8272	48.0294	-1.09	1.0636	-26.3079
43.7587	48.0294	139.3058	25.0327	-6.7271	1.2659
2.8429	-1.09	25.0327	28.5005	-0.8164	2.9221
22.0135	1.0636	-6.7271	-0.8164	26.3701	5.8876
6.7227	-26.3079	1.2659	2.9221	5.8876	43.0491

5

154.6	59.5	0.4
-------	------	-----

121.7967	52.846	71.4652	-0.4035	4.8028	20.3784
52.846	99.8535	62.8621	15.5378	-11.4519	-7.0588
71.4652	62.8621	103.9032	10.5826	-5.5622	5.4072
-0.4035	15.5378	10.5826	43.0729	7.5359	-12.84
4.8028	-11.4519	-5.5622	7.5359	55.1482	2.5198
20.3784	-7.0588	5.4072	-12.84	2.5198	33.9522

6

138.8	47.2	82.5
-------	------	------

143.0023	53.2898	43.5019	-0.4289	-21.9538	-8.8214
53.2898	127.3868	54.4822	-2.9096	-2.7458	26.8932
43.5019	54.4822	126.9631	27.7573	3.3224	-0.7021
-0.4289	-2.9096	27.7573	35.4107	1.2724	-5.1758
-21.9538	-2.7458	3.3224	1.2724	24.9573	2.3469
-8.8214	26.8932	-0.7021	-5.1758	2.3469	35.9059

7

53	79.2	95
----	------	----

117.3649	57.9475	39.6235	-4.5681	8.2378	-25.4475
57.9475	100.1118	74.1906	-5.6663	-3.9725	-7.6015
39.6235	74.1906	138.9002	3.0231	-13.835	2.8585
-4.5681	-5.6663	3.0231	57.9447	-0.5733	-5.0603
8.2378	-3.9725	-13.835	-0.5733	21.4095	-5.3878
-25.4475	-7.6015	2.8585	-5.0603	-5.3878	37.4073

8

20.1	40.9	75
------	------	----

158.9152	46.3055	46.4834	-1.5834	7.7494	5.8947
46.3055	136.8326	47.2504	-11.4279	2.4938	-24.0967
46.4834	47.2504	124.0736	-17.2437	-21.315	9.1956
-1.5834	-11.4279	-17.2437	26.8251	8.1718	1.2353
7.7494	2.4938	-21.315	8.1718	28.481	-5.0225
5.8947	-24.0967	9.1956	1.2353	-5.0225	29.7332

9

59.3	26.1	90.2				
112.6459	69.3539	63.6845	-3.6053	-15.621	-7.4102	
69.3539	139.963	42.3989	-11.9779	10.3119	9.0985	
63.6845	42.3989	96.4165	2.4522	-16.806	-7.2196	10
-3.6053	-11.9779	2.4522	22.6578	-7.8483	7.7981	
-15.621	10.3119	-16.806	-7.8483	43.2578	-5.0979	
-7.4102	9.0985	-7.2196	7.7981	-5.0979	54.5217	

38.8	22.2	39.4				
154.8381	55.9473	40.5655	8.0874	2.0916	10.2795	
55.9473	129.7553	63.6526	-9.4241	-12.3589	-17.3572	
40.5655	63.6526	94.9758	-16.412	-4.0029	2.5391	11
8.0874	-9.4241	-16.412	43.2674	2.0232	-13.9811	
2.0916	-12.3589	-4.0029	2.0232	20.4072	6.0699	
10.2795	-17.3572	2.5391	-13.9811	6.0699	41.4909	

62.5	17.6	70.8				
129.0339	59.456	61.8272	-12.6439	-12.9854	-14.3422	
59.456	151.5858	42.6892	7.9654	10.2176	8.2315	
61.8272	42.6892	91.3355	-3.9852	-13.875	3.6729	12
-12.6439	7.9654	-3.9852	22.4215	3.3958	8.3257	
-12.9854	10.2176	-13.875	3.3958	41.1714	-13.6287	
-14.3422	8.2315	3.6729	8.3257	-13.6287	45.3794	

118.4	161.6	105.2				
154.3264	45.8307	49.824	-10.9112	-3.6545	11.0095	
45.8307	152.9668	54.7351	11.9423	10.3005	2.0168	
49.824	54.7351	91.8271	-10.305	10.5056	-10.3126	13
-10.9112	11.9423	-10.305	34.5056	-10.0041	12.2501	
-3.6545	10.3005	10.5056	-10.0041	29.1908	-11.9654	
11.0095	2.0168	-10.3126	12.2501	-11.9654	31.6934	

0	0	0				
144.5	57.1	53.4	-20.5	0	0	
57.1	144.5	53.4	20.5	0	0	
53.4	53.4	83.1	0	0	0	14
-20.5	20.5	0	32.6	0	0	
0	0	0	0	32.6	-20.5	
0	0	0	0	-20.5	43.7	

Quartz rotated elastic tensors

13	98.8	28.1				
76.1951	17.3032	13.657	2.5767	3.0507	-4.5336	
17.3032	108.8661	3.2811	-0.6709	5.5369	-5.6061	
13.657	3.2811	89.5565	-5.6474	-9.4514	15.5767	1
2.5767	-0.6709	-5.6474	47.8905	18.1347	5.1305	
3.0507	5.5369	-9.4514	18.1347	47.7772	0.8163	
-4.5336	-5.6061	15.5767	5.1305	0.8163	62.2235	
178.5	88	115.3				
86.1987	11.5773	8.1414	-17.3727	1.2376	3.3271	
11.5773	106.1805	13.4939	0.7701	-1.2565	0.4731	
8.1414	13.4939	84.2957	15.7169	0.042	-4.4641	2
-17.3727	0.7701	15.7169	58.6857	-4.7764	-1.2456	
1.2376	-1.2565	0.042	-4.7764	41.4141	-17.7893	
3.3271	0.4731	-4.4641	-1.2456	-17.7893	56.7628	
162.6	120	90.6				
77.2938	21.0714	9.2384	-2.8348	5.9634	-2.0421	
21.0714	103.3085	-1.1335	8.7065	13.1714	-2.3073	
9.2384	-1.1335	104.1451	4.6235	-22.4238	-1.0866	3
-2.8348	8.7065	4.6235	43.2651	-3.6441	11.624	
5.9634	13.1714	-22.4238	-3.6441	46.2774	2.1029	
-2.0421	-2.3073	-1.0866	11.624	2.1029	63.2839	
171.5	58.8	99.2				
79.3997	10.8104	16.0959	-3.9677	-4.2369	10.0655	
10.8104	110.2928	2.9747	1.3628	-13.5091	-12.0374	
16.0959	2.9747	93.6456	-8.5263	19.4096	-0.7448	4
-3.9677	1.3628	-8.5263	47.9836	-2.0229	-12.7265	
-4.2369	-13.5091	19.4096	-2.0229	52.7437	-9.2046	
10.0655	-12.0374	-0.7448	-12.7265	-9.2046	52.8036	
31.4	127.3	17.6				
102.1448	11.5828	-3.4648	2.6318	5.4065	21.1959	
11.5828	109.0281	-3.0013	-16.8142	5.0451	-11.9906	
-3.4648	-3.0013	121.6935	3.7315	-16.8309	-2.0576	5
2.6318	-16.8142	3.7315	40.146	1.3051	2.0439	
5.4065	5.0451	-16.8309	1.3051	36.2262	-2.285	
21.1959	-11.9906	-2.0576	2.0439	-2.285	52.3945	

154.6	59.5	0.4
-------	------	-----

83.3619	5.1902	20.8173	-0.9628	14.7734	1.4339
5.1902	105.1661	10.9313	1.4237	-14.5257	-14.9167
20.8173	10.9313	80.6943	-10.4948	4.5168	6.1762
-0.9628	1.4237	-10.4948	54.499	2.7386	-12.2842
14.7734	-14.5257	4.5168	2.7386	58.7778	-5.6835
1.4339	-14.9167	6.1762	-12.2842	-5.6835	47.3119

6

138.8	47.2	82.5
-------	------	------

112.2185	4.3561	-4.7417	1.0602	-2.2637	-21.309
4.3561	105.6639	3.6214	-20.2365	-4.9328	10.7535
-4.7417	3.6214	118.746	9.6488	15.5372	3.7784
1.0602	-20.2365	9.6488	46.0301	0.5899	-1.0087
-2.2637	-4.9328	15.5372	0.5899	36.8161	-3.4222
-21.309	10.7535	3.7784	-1.0087	-3.4222	44.0395

7

53	79.2	95
----	------	----

120.9533	4.3214	-3.7429	-6.7313	11.5652	-8.1757
4.3214	86.0902	24.3648	0.036	-4.9538	14.1485
-3.7429	24.3648	86.17	9.5088	-2.8776	5.8065
-6.7313	0.036	9.5088	62.2105	11.3484	-3.1972
11.5652	-4.9538	-2.8776	11.3484	37.281	-5.4075
-8.1757	14.1485	5.8065	-3.1972	-5.4075	49.1018

8

20.1	40.9	75
------	------	----

105.4641	0.174	1.5478	1.5576	17.1518	13.5971
0.174	120.4878	-5.1591	10.1347	0.1554	-14.9522
1.5478	-5.1591	124.0226	0.1123	-12.9874	4.8691
1.5576	10.1347	0.1123	39.4359	6.5224	2.1878
17.1518	0.1554	-12.9874	6.5224	42.2301	7.1113
13.5971	-14.9522	4.8691	2.1878	7.1113	38.5468

9

59.3	26.1	90.2
------	------	------

76.1496	18.7041	14.6811	-2.8904	5.5166	-1.662
18.7041	88.986	-0.5087	1.9633	11.1006	13.1082
14.6811	-0.5087	112.2115	6.0504	-7.9886	-9.2881
-2.8904	1.9633	6.0504	42.9813	-8.2727	15.1601
5.5166	11.1006	-7.9886	-8.2727	59.2782	-0.48
-1.662	13.1082	-9.2881	15.1601	-0.48	54.2669

10

38.8	22.2	39.4				
102.5873	6.731	-1.9946	8.6606	15.1844	13.1773	
6.731	84.4953	16.8762	7.9813	-9.7859	-10.9377	
-1.9946	16.8762	112.7922	-9.7169	0.1693	-0.4688	11
8.6606	7.9813	-9.7169	61.4063	0.3643	-7.1664	
15.1844	-9.7859	0.1693	0.3643	42.1692	11.9186	
13.1773	-10.9377	-0.4688	-7.1664	11.9186	41.687	

62.5	17.6	70.8				
82.1048	9.5012	16.1212	-10.2958	4.091	-10.2025	
9.5012	95.2301	1.6638	15.3018	10.9256	9.5069	
16.1212	1.6638	111.1927	-1.6256	-8.5231	1.6468	12
-10.2958	15.3018	-1.6256	46.0042	2.0943	13.9806	
4.091	10.9256	-8.5231	2.0943	61.0882	-8.7055	
-10.2025	9.5069	1.6468	13.9806	-8.7055	43.8437	

118.4	161.6	105.2				
104.685	-2.2733	5.4465	-8.784	-18.9338	7.0659	
-2.2733	96.8126	11.9332	19.3215	6.8717	-0.8684	
5.4465	11.9332	111.3895	-6.9191	5.3701	-7.2563	13
-8.784	19.3215	-6.9191	56.2119	-7.7544	3.7233	
-18.9338	6.8717	5.3701	-7.7544	50.3772	-7.0817	
7.0659	-0.8684	-7.2563	3.7233	-7.0817	32.1673	

0	0	0				
86.6	6.7	12.6	-17.8	0	0	
6.7	86.6	12.6	17.8	0	0	
12.6	12.6	106.1	0	0	0	14
-17.8	17.8	0	57.8	0	0	
0	0	0	0	57.8	-17.8	
0	0	0	0	-17.8	39.95	

REFERENCES

- Abramson, E. H., Brown, J. M., Slutsky, L. J., Zaug, J., 1997, Elastic constants of San Carlos olivine to 17GPa: *Journal of Geophysical Research*, v. 102, p. 12,253-12,263.
- Allmendinger, R.W., 2002, StereoWin for Windows. Computer Program.
- Anderson, O. L., Andreatch JR. P., 1966, Pressure derivatives of elastic constants of single-crystal MgO at 23° and -195.8°C: *Journal of the American Ceramic Society*, v. 49 (8), p. 404-409.
- Angel, R.J., Gonzalez-Platus, J., Alvaro, M., submitted, EosFit7c and a Fortran module (library) for equation of state calculations: *Zeitschrift für Kristallographie*.
- Ave Lallemand, H. G., Mercier, J-C. C., Carter, N. L., Ross, J. V., 1980, Rheology of the upper mantle: inferences from peridotite xenoliths: *Tectonophysics*, v. 70, p. 85-113.
- Bai, Q., Mackwell, S. J., Kohlstedt, D. L., 1991, High-temperature creep of olivine single crystals 1. Mechanical results for buffered samples: *Journal of Geophysical Research*, v. 96, p. 2441-2463.
- Bai, Q., and Kohlstedt, D. L., 1992, High-temperature creep of olivine single crystals 3. Mechanical results for unbuffered samples: *Philosophical magazine*, v. 66(6), p. 1149-1181.
- Barber, D. J., Wenk, W. R., 1973, The microstructures of experimentally deformed limestones: *Journal of Materials science*, v. 9, p. 500-508.
- Becker, T, W., Cheverot, S., Schulte-Pelkum, V., Blackman, D. K., 2006, Statistical properties of seismic anisotropy predicted by upper mantle geodynamic models: *Journal of Geophysical Research*, v. 111.
- Burkhard, M., 1993, Calcite twins, their geometry, appearance and significance as stress-strain markers and indicators of tectonic regime: a review: *Journal of Structural Geology*, v. 15, p. 351-368.
- Burnley, P. C., 2013, The importance of stress percolation patterns in rocks and other polycrystalline materials: *Nature Communications*, 4:2117.
- Burnley, P. C., Cline II, C. J., Drue, A., 2013, Kinking in Mg₂GeO₄: An EBSD study: *American Mineralogist*, v. 98, p. 927-931.

- Bystricky, M., Kunze, K., Burlini, L., Burg, J-P., 2000, High shear strain of olivine aggregates: Rheological and seismic consequences: *Science*, v. 290, p. 1564-1567.
- Bystricky, M., Heidelbach, F., Mackwell, S., 2006, Large-strain deformation and strain partitioning in polyphase rocks: Dislocation creep of olivine-magnesiowüstite aggregates: *Tectonophysics*, v. 427, p. 115-132.
- Carter, N. L., Ave Lallemand, H. G., 1970, High temperature flow of dunite and peridotite: *Geological Society of America Bulletin*, v. 81, p. 2181-2202.
- Castenlau, O., Blackman, D. K., Lebonsohn, R. A., Ponte Castaneda, P., 2008, Micromechanical modeling of the viscoplastic behavior of olivine: *Journal of Geophysical Research*, v. 113, B09202.
- Chen, J., Li, L., Yu, T., Long, H., Weidner, D., Wang, L., Vaughan, M., 2006, Do Reuss and Voigt bounds really bound in high-pressure rheology experiments: *Journal of Condensed Matter*, v. 18, p. 1049-1059.
- Clausen, B., 1997, Characterisation of polycrystal deformation: PhD thesis, Riso National Laboratory, Roskilde, Denmark, 86 p.
- Clausen, B., Lorentzen, T., Leffers, T., 1998, Self-consistent modeling of the plastic deformation of F.C.C. polycrystals and its implications for diffraction measurements of internal stresses: *Acta Metallurgica*, v. 46, p. 3087-3098.
- Couvy, H., 2005, Experimental deformation of forsterite, wadsleyite and ringwoodite: Implications for seismic anisotropy of the Earth's mantle: PhD thesis, Université de Lille and Bayreuth University, 161 p.
- Dehoog, J. C. M., Gall, L., Cornell, D. H., 2010, Trace-element geochemistry of mantle olivine and application to mantle petrogenesis and geothermobarometry: *Chemical Geology*, v. 270, p. 196-215.
- Delannay, I., 2001, Observation and modeling of grain interactions and grain subdivision in rolled cubic polycrystals: PhD thesis, Katholieke Universiteit Leuven, 181 p.
- Demouchy, S., Schneider, S. E., Mackwell, S. J., Zimmerman, M. E., Kohlstedt, D. L., 2009, Experimental deformation of olivine single crystals at lithospheric temperatures: *Geophysical Research Letters*, v. 36, L04304.
- Dölle, H., 1979, The influence of multiaxial stress states, stress gradients and elastic anisotropy on the evaluation of (residual) stresses by X-Rays: *Journal of applied Crystallography*, v. 12, p. 489-501.

- Durham, W. B., Goetze, C., Blake, B., 1977, Plastic flow of orientated single crystals of olivine 2. Observations and interpretations of the dislocation structures: *Journal of Geophysical Research*, v. 82(36), p.5755.
- Eshelby, J. D., 1957, The determination of the elastic field of an ellipsoidal inclusion, and related problems: *Proceedings of the Royal Society of London, Mathematical and Physical Science*, v. 241(1226), p. 376-396.
- Faul, U. H., Jackson, I., 2005, The seismological signature of temperature and grain size variations in the upper mantle: *Earth and Planetary Science Letters*, v. 234, p. 119-134.
- Faul, U. H., Gerald, J. F., Farla, R. J. M., Ahlefeldt, R., and Jackson, I., 2011, Dislocation creep of fine-grained olivine: *Journal of Geophysical Research*, v. 116(B1).
- Friák, M., Counts, W. A., Ma, D., Sander, B., Holec, D., Raabe, D., Neugebauer, J., 2012, Theory-guided materials design of multi-phase Ti-Nb alloys with bone-matching elastic properties: *Materials*, v. 5, p. 1853-1872.
- Getting, I. C., Chen, G., Brown, J., 1993, The strength and rheology of commercial Tungsten carbide cements used in high-pressure apparatus: *Pure and Applied Geophysics*, v. 141, p. 546-577.
- Goetze, C., 1978, The mechanisms of creep in olivine: *Philosophical Transactions of the Royal Society of London*, v. 288, p. 99-119.
- Green, H. W., Radcliffe, S. V., 1972, Dislocation mechanisms in olivine and flow in the upper mantle: *Earth and Planetary Science Letters*, v. 15, p. 239-247.
- Griggs, D. T., Turner, F. J., Heard, H. C., 1960, Deformation of rocks at 500° to 800°: *Geologic Society of America Memoirs*, v. 79, p. 39-104.
- Groshong Jr. R. H., 1972, Strain calculated from twinning in calcite: *Geological Society of America Bulletin*, v. 83, p. 2025-2038.
- Hansen, L. N., Zimmerman, M. E., Kohlstedt, D. L., 2011, Grain boundary sliding in San Carlos olivine: Flow law parameters and crystallographic-preferred orientation: *Journal of Geophysical Research*, v. 116, B08201.
- Hansen, L. N., Zimmerman, M. E., Dillman, A. M., and Kohlstedt, D. L., 2012, Strain localization in olivine aggregates at high temperature: A laboratory comparison of constant-strain-rate and constant-stress boundary conditions: *Earth and Planetary Science Letters*, v. 333, p. 134-145.

- Hirth, G., Kohlstedt, D., 2003, Rheology of the upper mantle and the mantle wedge: A view from the experimentalists: Inside the Subduction Factory, Geophysical monograph 138.
- Hull, D., & Bacon, D. J., 2011, Introduction to dislocations (Vol. 37): Butterworth-Heinemann.
- Jackson, I., Fitz Gerald, J. D., Faul, U. H., Tan, B. H., 2002, Grain-size-sensitive seismic wave attenuation in polycrystalline olivine: Journal of Geophysical Research, v. 107, ECV(5).
- Jackson, I., Faul, U.H., Fitz Gerald, J.D., Morris, S.J.S., 2006, Contrasting viscoelastic behavior of melt-free and melt-bearing olivine: implications for the nature of grain-boundary sliding: Materials Science and Engineering, v. A442, p. 170-174.
- Jang, B-A., Kim, C-B., Kang, S-S., 2012, Paleostress from calcite twins of limestones and its tectonic implication in South Korea: Geosystem Engineering, v. 15(3), p. 157-170.
- Karato, S-I., Paterson, M. S., Fitz Gerald, J. D., 1986, Rheology of synthetic olivine aggregates: Influence of grain size and water: Journal of Geophysical Research, v. 91, 8151
- Karato, S-I, 1988, The role of recrystallization in the preferred orientation of olivine: Physics of the Earth and Planetary Interiors, v. 51, p. 107-122.
- Karato, S-I., Wu, P., 1993, Rheology of the upper mantle: A synthesis: Science, v. 260(5109) p. 771-778.
- Karato, S-I., Dupas-Bruzek, C., Rubie, D., 1998, Plastic deformation of silicate spinel under the transition-zone conditions of earths mantle Nature, v. 395, p. 266-269.
- Karato, S-I., Jung, H., 2003, Effects of pressure on high-temperature dislocation creep in olivine: Philosophical Magazine, v. 83(3), p. 401-414.
- Karato, S-I., 2010, Rheology of the Earth's mantle: A historical review: Gondwana Research, v. 18, p. 17-45.
- Kimizuka, H., Ogata, S., Li, J., Shibutani, Y., 2007, Complete set of elastic constants of α -quartz at high pressure: A first principle study: Physical Review, v. 75 (3117).
- Kirby, S., 1983, Rheology of the lithosphere: Reviews of Geophysics and Space Physics, v. 21(6), p. 1458-1487.

- Kozachek, K. J., Ruud, C. O., Hirsch, J., Conway Jr., J. C., Yu, C. j., 1992, Crystallography-based prediction of plastic anisotropy of polycrystalline materials: *Journal of Nondestructive Evaluation*, v. 12 (1), p. 97-107.
- Kröner, E., 1961, Zur Plastischen Verformung des Vielkristalls: *Acta metalalia*, v. 9, p. 155.
- Lacombe, O., 2010, Calcite twins, a tool for tectonic studies in thrust belts and stable orogenic forelands: *Oil and Gas Science and Technology*, v. 65, p. 809-838.
- Laurent, P., Kern H., Lacombe, O., 2000, Determination of deviatoric stress tensors based on inversion of calcite twin data from experimentally deformed monophase samples. Part II. Axial and triaxial stress experiments: *Tectonophysics*, v. 327, p. 131-148.
- Lazarus, D., Jefferey, R. N., Weiss, J. D., 1971, Relative pressure dependence of chromel/alumel and platinum/platinum-10%rhodium thermocouples: *Applied Physics Letters*, v. 19(10), p. 371-373.
- Ledbetter, H., Migliori, A., 2006, A general elastic-anisotropy measure: *Journal of Applied Physics*, v. 100, 063516.
- Lee, H-Y., Jiang, Z., Karato, S-I., 2002, A scanning electron microscope study of the effects of dynamic recrystallization on lattice preferred orientation in olivine: *Tectonophysics*, v. 351, p. 331-341.
- Lenze, A., Stöckhert, B., Wirth, R., 2005, Grain scale deformation in ultra-high-pressure metamorphic rocks-an indicator of rapid phase transformation: *Earth and Planetary Science Letters*, v. 229, p. 217-230.
- Lin, C-C, 2013, Elasticity of calcite: Thermal evolution: *Physics and Chemistry of Minerals*, v. 40, p. 157-166.
- Long, H., Weidner, D. J., Li, L., Chen, J., and Wang, L., 2011, Deformation of olivine at subduction zone conditions determined from in situ measurements with synchrotron radiation: *Physics of the Earth and Planetary Interiors*, v. 186(1), p. 23-35
- Mainprice, D., Barruol, G., Ismail, W. B., 2000, The seismic anisotropy of the Earth's mantle: from single crystal to polycrystal: *Earth's Deep Interior: Mineral Physics and Tomography from the Atomic Scale to the Global Scale*, Geophysical Monograph Series, v. 117, p. 237-264.

- Maitland, T., Sitzman, S., 2007, Electron backscatter diffraction (EBSD) technique and materials characterization examples: Scanning Microscopy for Nanotechnology Techniques and Application, XIV, 522 p.
- Molinari, A., Azhi, S., Kouddane, R., 1997, On the self-consistent modeling of elastic-plastic behavior of polycrystals: *Mechanics of Materials*, v. 26, p. 43-62.
- Murray, C. E., 2013, Equivalence of Kröner and weighted Voigt-Reuss models for x-ray stress determination: *Journal of Applied Physics*, v. 113, 153509.
- Nicolas, A., 1978, Stress estimates from structural studies in some mantle peridotites: *Philosophical Transactions of the Royal Society of London*, v. 288, p. 49-57.
- Padaki, V. C., Lakshmikumar, S. T., Subramanyam, S. V., Gopal, E. S. R., 1981, Elastic constants of galena down to liquid helium temperatures: *Pramana*, v. 17(1), p. 25-32.
- Pfiffner, O. A., Burkhard, M., 1987, Determination of paleostress axis orientations from fault, twin earthquake data: *Annales Tectonicae*, v. 1, p. 48-57.
- Poirier, J-P., 1975, On the slip systems of olivine: *Journal of Geophysical Research*, v. 80(23).
- Raj, R., Ashby, M.F., 1971, On grain boundary sliding and diffusional creep: *Metallurgical Transactions*, v. 2, p. 1113-1127.
- Raterron, P., Chen, J., Li, L., Weidner, D., Cordier, P., 2007, Pressure-induced slip-system transition in forsterite: Single-crystal rheological properties at mantle pressure and temperature: *American Mineralogist*, v. 92, p. 1436-1445.
- Raterron, P., Chen, J., Geenen, T., Girard, J., 2011, Pressure effect on forsterite dislocation slip systems: implications for upper-mantle LPO and low viscosity zone: *Physics of the Earth and Planetary Interiors*, v. 188, p. 26-36.
- Rez, J., Melichar, R., 2010, Peek inside the black box of calcite twinning paleostress analysis: *Trabajos de Geologia*, v. 30, p. 163-168.
- Rybacki, E., Evans, B., Janssen, C., Wirth, R., Dressen, G., 2013, Influence of stress, temperature, and strain on calcite twins constrained by deformation experiments: *Tectonophysics*, v. 601, p. 20-36.

- Sachs, E., 1928, Zur Ableitung einer Fließbedingung., **72**, 734
- Smyth, J., Hazen, R. M., 1973, The crystal structure of forsterite and hortonolite at several temperatures up to 900°C: *American Mineralogist*, v. 58, p. 588-593.
- Spang, J. H., 1972, Numerical method for dynamic analysis of calcite twin lamellae: *Geological Society of America Bulletin*, v. 83, p. 467-472.
- Srivastava S. K., Sharma, S. K., 2007, Elastic constants for NaCl and KCl solids at high temperatures: *Journal of Physics and Chemistry of Solids*, v. 68, p. 1648-1651.
- Stocker, R. L., Ashby, M. F., 1973, On the rheology of the upper mantle: *Reviews of Geophysics and space Physics*, V. 11(2), p. 391-426.
- Taylor, G., 1938, Plastic strain in metals: *J. Inst. Metals*, v. 62, p. 307-324.
- Tielke, J. A., 2010, Development and application of a method for determining paleostress from calcite deformation twins using electron backscatter diffraction: M.s. thesis, South Dakota School of Mines and Technology, 133 p.
- Turner, F. J., 1953, Nature and dynamic interpretation of deformation lamellae in calcite of three marbles: *American Journal of Science*, v. 251, p. 276-298.
- Valcke, S., Pennock, G., Drury, M., De Bresser, J., 2006, Electron backscattered diffraction as a tool to quantify subgrains in deformed calcite, *Journal of Microscopy*, v. 224, p. 264-276.
- Wang, Y., Durham, W. B., Getting, I. C., Weidner, D. J., 2003, The deformation-DIA: A new apparatus for high temperature triaxial deformation to pressures up to 15 GPa: *Review of Scientific Instruments*, v. 74(6), p. 3002-3011.
- Wenk, H. R., Venkatasubramanian, C. S., Baker, D. W., 1973, Preferred orientation in experimentally deformed limestone: *Contributions to Mineralogy and Petrology*, v. 38, p. 81-114.
- Zener, C., 1948, *Elasticity and Anelasticity of Metals*: University of Chicago Press, Chicago, p. 16
- Zhang, S., Karato, S-I., 1995, Lattice preferred orientation of olivine aggregates deformed in simple shear: *Nature*, v. 375, p. 774-777.

- Zhang, S., Karato, S-I., Fitz Gerald, J., Faul, U, H., Zhou, Y., 1999, Simple shear deformation of olivine aggregates: *Tectonophysics*, v. 316, p. 133-152.
- Zhao, Z., Kucknicki, S., Radovitzky, R., Cuitiño, A., 2007, influence of in-grain mesh resolution on the prediction of deformation textures in FCC polycrystals by crystal plasticity FEM: *Acta Materialia*, v. 55, p. 2361-2373.

VITA

Graduate college
University of Nevada Las Vegas

Christopher J. Cline II

Degrees

Bachelor of Science, Geology, 2012
University of Nevada Las Vegas

Awards and honors

UNLV graduate access grant (2013)
Bernada French Scholarship (2011)
Southern Nevada Gem and Mineralogical Society scholarship (2011)
UNLV grant (2011)
Anne Wyman outstanding mineralogist award (2010)

Publications

Tanis, E. A., Simon, A., Tschauner, O., Chow, P., Xiao, Y., Burnley, P.,
Cline, C., Hanchar, J., Pettke, T., Shen, G., Zhao, Y., Submitted,
Experimental constraints on the mobility of Nb-rutile in NaCl- and
NaF-bearing aqueous fluids during the blueschist to eclogite
transition in subduction zones: American Mineralogist.

Burnley, P. C., **Cline II, C. J.**, Drue, A., 2013, Kinking in Mg₂GeO₄: An
EBSD study: American Mineralogist, v. 98, p. 927-931.

Thesis title: The effect of single crystal elastic and plastic anisotropy on stress
and strain heterogeneity: comparison of olivine to other common minerals

Masters thesis examination committee

Chair: Pamela C. Burnley Ph. D.
Committee member: Rodney V. Metcalf Ph. D.
Committee member: Michael L. Wells Ph. D.
Graduate faculty representative: Andrew Cornelius Ph. D.

